NTNU – Trondheim
Norwegian University of
Science and Technology

IN-SITU FRACTURE MECHANICAL TESTING OF MICROSIZED CANTILEVERS

Kristine Greina

Problem text

**MASTER THESIS 2014
FOR
STUD.TECHN. KRISTIN GREINA**

IN-SITU FRACTURE MECHANICAL TESTING OF MICROSIZED CANTILEVERS
In-situ bruddmekanisk prøving av mikro bjelker

The Arctic is exceedingly interesting for the petroleum industry, and constitutes huge possibilities of prospective areas. The arctic is an appealing new ventures area; however the climate is extremely demanding, and more technically challenging than any other environment. With low design temperatures down to -60°C brittle behavior of materials is of great concern. Brittle fracture has a rapid propagation without significant deformation. A sudden failure is always dangerous because it involves a considerable element of unpredictability.

The rapid developments within nanotechnology have made it possible to machine very small test specimens from selected areas within crystalline materials. In this way, very precise mechanical properties can be obtained. In order to understand the deformation behavior of complex steel alloys used in arctic environments it is crucial to comprehend the local deformation behavior of iron. Knowledge about the local deformation behavior at low temperatures may lead to a better understanding of the origin and mechanism of cleavage fracture.

Nanomechanical testing at low temperatures is in theory possible by cooling the samples by means of a cold finger connected to a liquid nitrogen tank. Extensive work shall be put into arranging a test setup to combine a Coldfinger and a Piconindenter in a Scanning Electron Microscope (SEM) vacuum chamber.

Nanomechanical testing procedure of pure iron:
- Crystallographic orientation shall be determined with Electron BackScatter Diffraction (EBSD) examinations.
- Microsized cantilever beams shall be machined by means of Focused Ion Beam (FIB) milling at NTNU NanoLab.
- Fracture mechanical testing of cantilevers at low temperatures with a Picoindenter interfaced with a SEM shall be conducted. The purpose is to precisely record load displacement data, while simultaneously observe the deformation process, in order to obtain indications of the local fracture toughness.
- Determining a method of measuring the Crack Tip Opening Displacement (CTOD) during in-situ testing.

The nanomechanical testing procedure exhibit exciting possibilities. Depending on the progress, additional testing may be applied to grain-boundary effects or the effect of specific microstructural constituent, such as MA phases, of industrial materials from the joint industry project: Arctic Materials.

Three weeks after start of the thesis work, an A3 sheet illustrating the work is to be handed in. A template for this presentation is available on the IPM's web site under the menu "Masteroppgave" (http://www.ntnu.no/ipm/masteroppgave). This sheet should be updated one week before the Master's thesis is submitted.

Performing a risk assessment of the planned work is obligatory. Known main activities must be risk assessed before they start, and the form must be handed in within 3 weeks of receiving the problem text. The form must be signed by your supervisor. All projects are to be assessed, even theoretical and virtual. Risk assessment is a running activity, and must be carried out before starting any activity that might lead to injury to humans or damage to materials/equipment or the external environment. Copies of signed risk assessments should also be included as an appendix of the finished project report.

The thesis should include the signed problem text, and be written as a research report with summary both in English and Norwegian, conclusion, literature references, table of contents, etc. During preparation of the text, the candidate should make efforts to create a well arranged and well written report. To ease the evaluation of the thesis, it is important to cross-reference text, tables and figures. For evaluation of the work a thorough discussion of results is appreciated.

The thesis shall be submitted electronically via DAIM, NTNU's system for Digital Archiving and Submission of Master's thesis.

Torgeir Welo
Head of Division

Christian Thaulow
Professor/Supervisor

NTNU
Norges teknisk-
naturvitenskapelige universitet
Institutt for produktutvikling
og materialer

Preface

This report is written as a partial requirement for a Master degree in Material Science and Technology at the Norwegian University of Science and Technology (NTNU). The Master thesis is conducted at the Department of Engineering Design and Materials. The report serves as a documentation of the performed work, during a duration of 20weeks.

Extensive work has been put into designing and developing a cooling system to be interfaced with a picoindenter and SEM set-up, in order to cool down the sample during in-situ fracture experiments. The design of the cooling system proved challenging and extremely time consuming due to the sensitivity of the picoindenter and the limited space inside the SEM chamber. A series of discussion and deliberations with professionals within different fields were crucial. The development of the new testing equipment involved a series of trial and error before a successful solution was obtained. Some components had to be ordered externally, which resulted in some delays due to shipping problems. A series of components had to be machined by different mechanical workshops at NTNU. By this the progress of the experimental work was dependent external personnel.

During the coarse of this project downtime of the Focused Ione Beam, at Nanolab NTNU caused some delays in the experimental work related to fabrication of micro-cantilevers.

I had the pleasure of attending the nanomechanical conference Nanobrücken, in Saarbrücken Germany. This was a great opportunity to consult my work with experts within the field. At the conference my work was presented with a poster, which is included in Appendix G: Posters presented at Nanobrücken.

In order to present my thesis a poster was made at the beginning and end of the present work, these are included in Appendix F: Posters. Performing a risk assessment of the planned work was obligatory and is presented in Appendix H: Risk evaluation.

Abstract

The arctic is an appealing new ventures area for the oil and gas industry. However the climate is extremely demanding, and more technically challenging than any other environment. With design temperatures down to -60°C the ductile to brittle transition temperature (DBTT) is an important concern. The propagation of a brittle fracture in iron and steel requires much less energy than that associated with a ductile fracture. Once a material is cooled below the DBTT, it has a much greater tendency to shatter on impact instead of bending or deforming. The brittle-ductile behavior of BCC crystals has long been an area of intensive study, however the fundamental mechanisms that control the transition have not yet been explained. The rapid development within nanotechnology has made it possible to conduct small scale fracture experiments. The development of innovative nanomechanical testing techniques could lead to a better understanding of fracture properties at low temperatures, quantitative information on local stress requirements for crack propagation and subsequently explain the fundamental mechanisms that control the ductile to brittle transition.

Advanced fracture experiments of pure iron at a micron scale have been completed. Electron Backscatter Diffraction analysis were conducted in order to determine the crystal orientation of the surface grains. Micro-cantilevers with dimensions of approximatly 2x2x10 µm were fabricated, in grains with preferred crystal orientation, by means of Focused Ion Beam (FIB) milling. The cantilevers were then loaded in a controlled manner to obtain load displacement data using a Picoinenter. The use of a picoindenter combine with a Scanning Electron Microscope (SEM) has shown to be a valuable tool since it allows events observed in the mechanical data to be correlated directly with the corresponding deformation mechanisms witnessed through the electron microscope. Extensive work has been put in to designing and constructing a cooling system, in order to conduct micro fracture experiments at low temperatures. The developed cooling system consists of a liquid nitrogen tank mounted on an SEM port, which is mechanically connected to the sample through a coldfinger. The thermal conductivity of the cooling system proved be sufficient; after approximately 1,5h a temperature of -90°C was reached, and loading of cantilevers at room temperature, -70°C and -90°C were successfully conducted.

All cantilever were plastically deformed during loading, but no fracture occurred. Due to the absence of fracture the critical stress intensity factor, i.e. fracture toughness, could not be determined. However the preliminary stress intensity, (K_Q) was calculated using five different methods. The results showed a drop in the preliminary stress intensity values between -70°C and -90°C. The K_Q values may indicate the stress causing the first deviation from ideal elastic behavior by dislocation movement and plastic deformation. By this, the stress at which plastic deformation starts, decrease with decreasing temperature.

It was not possible to measure the Crack Tip Opening Displacement (CTOD) directly during in-situ experiments, due to low image resolution. However, CTOD was calculated with two different methods: the hinge model and the double gauge model, both relying on the measurements of CMOD during loading. CTOD values for the two different methods were compared, however, they did not correlate. The double gauge model is probably the most accurate method since it is a direct approach and independent of the global behavior, whereas the hinge model relies on accurate values for the rotational center.

Sammendrag

Oljeindustrien viser stor interesse for utvinning i Arktiske strøk. Dette er et spennende satsningsområdet med mange prospektive områder. Det arktiske klimaet derimot har vist seg å være utfordrende for materialer, spesielt krevende er de lave temperaturer ned til -60°C. Omslagstemperaturen (DBTT) fra duktil til sprø oppførsel er et viktig anliggende. Sprø brudd i jern og stål krever langt mindre energi en duktile brudd. Når et materiale avkjøles til temperaturer lavere enn omslagstemperaturen er hurtige og ustabile brudd mer sannsynlig enn deformasjon. Omslagstemperaturen fra duktil til sprø oppførsel hos bcc materialer har lenge vært kjent, men de grunnleggende mekanismene som styrer overgangen er ennå ikke forklart.

Den raske utviklingen innen nanoteknologi har gjort det mulig å gjennomføre bruddforsøk på mikroskala. Utviklingen av innovative nanomekaniske test metoder kan føre til en bedre forståelse av bruddegenskaper ved lave temperaturer og kvantitativ informasjon om lokale spennings verdier for sprekk forplantning. Dette kan bidra til å fastslå de grunnleggende mekanismene som styrer omslagstemperaturen.

Mikroskala bruddforsøk av rent jern har blitt utført. Først ble en EBSD analyse gjennomført for å bestemme krystallorientering til overflate kornene. Mikrobjelker med dimensjoner på omtrent 2x2x10 mikrometer ble fabrikkert ved hjelp av Fokusert Ion Beam (FIB), i korn med foretrukne krystall orientering. Bjelkene ble deretter lastet på en kontrollert måte for å oppnå lastforskyvningsdata ved hjelp av en Picoinenter. Bruken av en picoindenter kombinere med et elektronmikroskop (SEM) har vist seg å være et verdifullt verktøy, da hendelser observert i de mekaniske dataene kan korreleres direkte med tilsvarende deformasjonsmekanismer observert gjennom elektronmikroskopet.

Omfattende arbeid ble lagt ned i å designe og konstruere et kjølesystem, for å utføre mikrobruddforsøk ved lave temperaturer. Det utviklede kjølesystemet består av en flytende nitrogentank som videre er mekanisk koblet til prøven gjennom en kaldfinger. Den termiske ledningsevnen til kjølesystemet vist seg å være tilstrekkelig; etter omtrent 1,5 time nådde prøven en temperatur på -90°C. Lasting av 8 bjelker ble gjennomført ved romtemperatur, -70°C og -90°C.

Lasting av bjelkene førte til plastisk deformasjon, men lastingen resulterte ikke i brudd for noen av bjelkene. Uten brudd var det ikke mulig å bregne bruddseigheten. Stress intensiteten (K_Q) ble midlertidig beregnet ved hjelp av fem forskjellige metoder. Resultatene viste et drop mellom -70°C og -90°C. K_Q verdiene kan indikere spenningen til det første avviket fra ideell elastisk oppførsel ved dislokasjonsbevegelse og plastisk deformasjon. Spenningen som forårsaker plastisk deformasjon avtar dermed med synkende temperatur.

På grunn av lav bildeoppløsning var det ikke mulig å utføre direkte CTOD målinger. CTOD ble midlertidig beregnet ved hjelp av to ulike metoder: "Hinge model" og "Double gauge model", som begge avhenger av CMOD målt under forsøkene. CTOD verdiene for de to ulike metodene ble sammenlignet, men de korrelerte ikke. "Double gauge model" er sannsynligvis den mest nøyaktige metoden på grunn av den direkte fremgangsmåten, som er uavhengig av den globale oppførsel, mens "Hinge model" er avhengig av nøyaktige verdier for rotasjonssenteret.

Nomenclature

DBTT = ductile to brittle transitions temperature
SEM = Scanning electron Microscope
FIB = Focused ion beam
EBSD = Electron backscatter diffraction
TEM = Transmission electron microscope
SE = secondary electrons
SI = Secondary ions
BCC = Bode centered cubic
FCC = face centered cubic
GND = geometrically necessary dislocations
$<...>$ = crystallographic direction
$\{...\}$ = crystallographic plane
σ_{mm} = stress required to propagate a crack through matrix/matrix interphase
σ_y = yield stress
σ_{pm} = stress required to propagate a crack through particle/matrix interphase
σ_I = local maximum stress
σ_{M-A} = stress required to initiate a crack at or near a brittle particle/ MA constituent.
K = Stress intensity factor
K_{IC} = fracture toughness (critical stress intensity factor)
σ_f = fracture stress
a = crack length
$f\left(\dfrac{a}{h}\right)$ = dimensionless shape factor
σ = bending stress
F = force
L = cantilever length from loading point to notch
w = cantilever width
h = cantilever height
S = length of three-point-bending specimen
y = vertical distance between the upper surface and the neutral plane
I = moment of inertia of the cantilever cross section
r_p = center of rotation
a_{eff} = effective crack length
CTOD = Crack tip opening displacement
d = distance from apparent crack tip to rotational point
$CTOD_{pl}$ = plastic crack tip opening displacement
$CTOD_{el}$ = elastic crack tip opening displacement
a_0 = original crack length
CMOD = Crack mouth opening displacment
h' = new cantilever height
A = cross-section area
v = potassio ratio
E = E-modulus (young's modulus)
CTOA = crack tip opening angle

Innholdsfortegnelse

1 <u>Introduction</u>

Within the oil and gas industry the Arctic constitutes huge possibilities of prospective areas. The arctic is an appealing new ventures area. However the climate is extremely demanding, and more technically challenging than any other environment. The environment in the Arctic consists of strong winds, large waves, drifting icebergs and low design temperatures (down to -60°C). The cold and harsh climate proves challenging for materials.

An important concern in arctic environment is the ductile to brittle transition temperature (DBTT). This is the temperature where the material changes from being ductile to brittle, or from fracturing in a ductile manner to a cleavage fracture. The propagation of a cleavage crack in iron and steel requires much less energy than that associated with the growth of a ductile crack. Once a material is cooled below the DBTT, it has a much greater tendency to shatter on impact instead of bending or deforming. Even tough the change of fracture properties at low temperatures has been known for more than a century; the fundamental mechanisms that control the transition have not yet been explained.

The rapid development within nanotechnology has made it possible to conduct small scale fracture experiments. Focused Ion Beam (FIB) milling makes it possible to fabricate micro-cantilever samples. A picoindenter may be utilized in order to conduct fracture experiments of these micro-cantilevers. The principle of mechanical bending of micro-cantilevers by indentation is to apply a load with the indenter tip at the edge of the free extremity of the cantilever. For brittle behavior the critical loading force where fracture occurs may be used to calculate the fracture toughness (K_{IC}). In case of a more ductile behavior the Crack tip opening displacement (CTOD) may serves as an engineering fracture parameter in practical applications. With a picoindnter that can be interfaced with a Scanning Electron Microscope (SEM) it is possible to perform bending of micro-cantilevers while simultaneously image the process, hence it is possible to measure CTOD during loading.

By designing and constructing a cooling system, low temperature micro fracture experiments are possible. The development of innovative nanomechanical testing techniques could lead to a better understanding of fracture properties at low temperatures, quantitative information on local stress requirements for crack propagation and subsequently explain the fundamental mechanisms that control the ductile to brittle transition.

The present work will assess a nanomechanical testing procedure for fracture experiments of micro-cantilevers. The theoretical background will discuss the ductile to brittle transition of bcc metals and different techniques of micro-cantilever fabrication. Additionally fracture toughness calculations and CTOD measurments for micro-sized samples is presented. Further the experimental procedure is explained in detail. Which consists of; Electron Backscatter Diffraction to determined crystallographic orientation, Focused Ion Beam preparation of micro-sized cantilevers, development of a cooling system and in-situ loading by means of a Picondenter interfaced with a Scanning Electron Microscope. Finally the results is presented and discussed.

2 Theoretical background

2.1 Fracture behavior

Fracture toughness is usually used as a generic term for measures of material resistance to extension of a crack. The fracture behavior of a metallic material is an important concern, in particular the theories of elasticity and plasticity. The fracture behavior relates to the micro-mechanism of fracture, and is usually described as being ductile or brittle. In general, the deformation behavior of a material determines which fracture parameter to be used.

2.1.1 Brittle fracture

A cleavage fracture has a rapid propagation, without significant plastic deformation prior to failure. The surface of a brittle fracture often has flat facets and a river pattern formed when the cleavage fracture is forced to re-initiate at the boundary of a grain in a different orientation. The "rivers" tend to merge in the direction of crack growth. On a microscopic level a brittle fracture is breaking of atomistic bonds. Brittle fracture behavior results in the development of rapid and unstable crack extension. Macroscopically, a test specimen demonstrating this mode of fracture has a unique and well-defined point of crack initiation. For brittle fracture, an annular zone of linear elastic deformation surrounds and dominates the crack tip and the initiation toughness dominates the material fracture resistance with only slight additional resistance to crack extension beyond crack initiation. Often the energy required to extend the crack beyond initiation is small, the specimen fails unstably, and no measurement of the fracture resistance beyond initiation is possible [1] [2] [3].
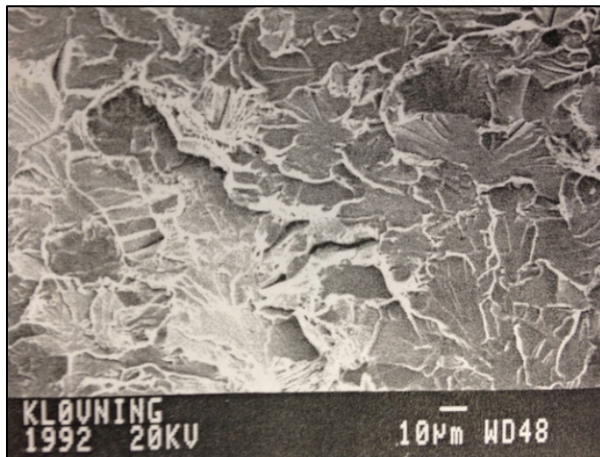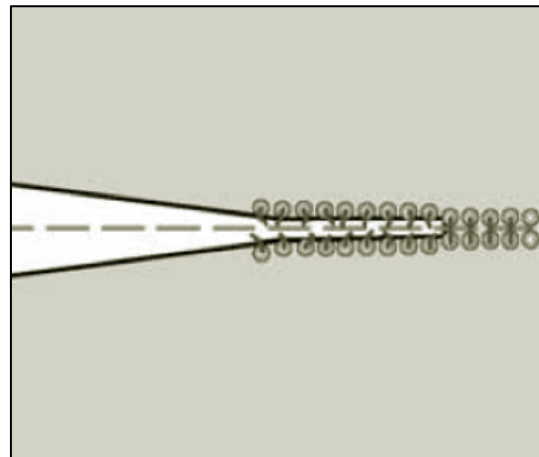

Figure 1: Cleavage fracture in steel [4]

Figure 2: Cleavage fracture [5]

2.1.2 Ductile fracture

In a ductile fracture, however, extensive plastic deformation takes place. In this case there is slow propagation and absorption of large amounts of energy before fracture. As the cracked structure is loaded, local strains and stresses at the crack tip becomes sufficient to nucleate voids. These voids grow, and will eventually coalesce to a crack. Growth and coalescence of microvoids progress as the local applied load increases. The material is being "pulled" apart generally leaving a rough surface. On a microscopic level a ductile fracture exists of nucleation and extension of dislocations. This macro mode of fracture has a continuous process of ductile tearing rather than a point fracture. The tearing resistance to grow the crack

a small increment can be significant. In some cases predominantly elastic conditions can continue to exist throughout. For ductile fracture, the plastic deformation dominates at the crack tip and the material resistance against fracture increases as the crack grows [1] [2] [3].
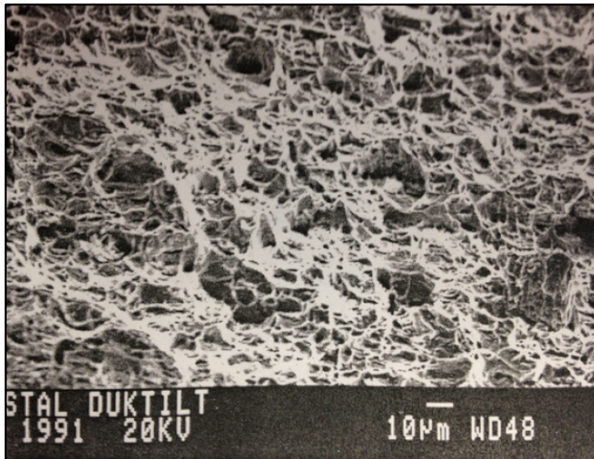

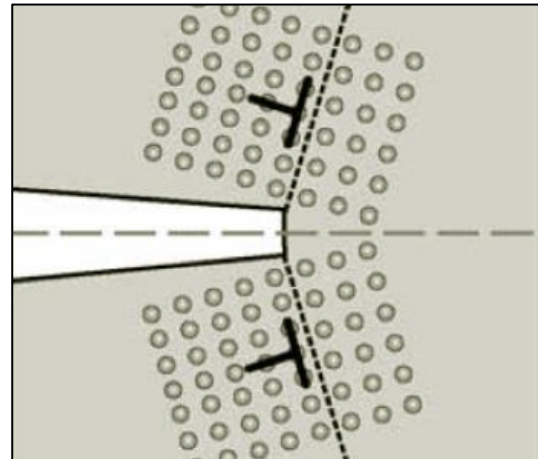Figure 3: Ductile fracture in steel [4]

Figure 4: Ductile fracture [5]

2.1.3 Ductile to brittle transition temperature

An important concern in arctic environment is the ductile to brittle transition temperature (DBTT). This is the temperature where the material changes from being ductile to brittle, or from fracturing in a ductile manner to a cleavage fracture. The propagation of a cleavage crack in iron and steel requires much less energy than that associated with the growth of a ductile crack. Once a material is cooled below the DBTT, it has a much greater tendency to shatter on impact instead of bending or deforming. Around the DBTT there is a reduction of fracture toughness when the temperature decreases [1] [2].
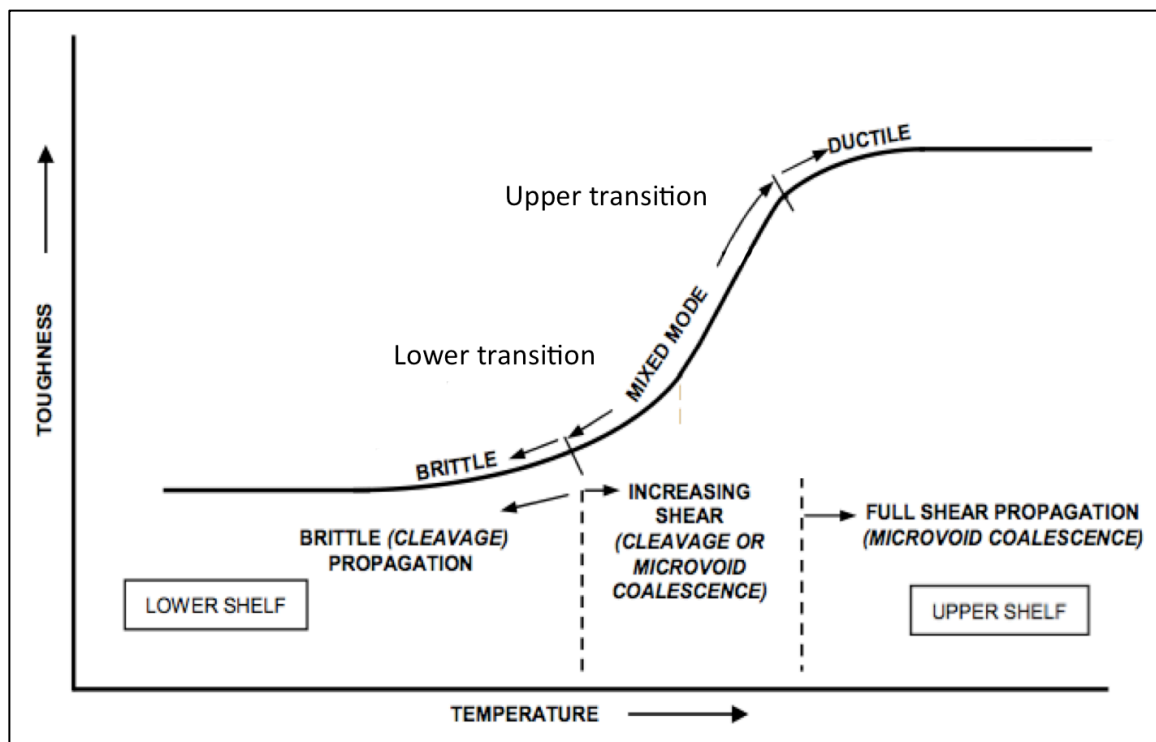
Figure 5: Ductile to brittle transition temperature, adapted from [6]

The DBTT is generally sharper in materials with a BCC lattice than those with a FCC lattice. The fracture toughness of a BCC crystal can change drastically over a very small temperature range. Even tough the change of fracture properties at low temperatures has been known for more than a century; the fundamental mechanisms that control the transition have not yet been explained. The main reason for the lack of a general understanding is probably due to the complex interdependence between a number of parameters such as rate of deformation, mode of loading, model size and geometry, crack size, crystallographic orientations and boundary conditions. The brittle-ductile behavior of BCC crystals has long been an area of intensive study. It is, however, difficult to reach a common quantitative understanding. The following section will attempt to summarize some of the aspects associated with the ductile to brittle transition temperature in BCC metals.

2.1.4 BCC deformation

Plastic deformation occurs by dislocation motion. The stress required to move a dislocation depends on the atomic bonding and the crystal structure. In general the yield process can be viewed as competing with fracture, and whichever process has the lowest stress requirements will dominate. Both yield and fracture stresses usually increase with decreasing temperature, but for BCC the yield is more temperature-dependent. This implies that below a critical temperature, DBTT, the material will fracture before it yields [7].
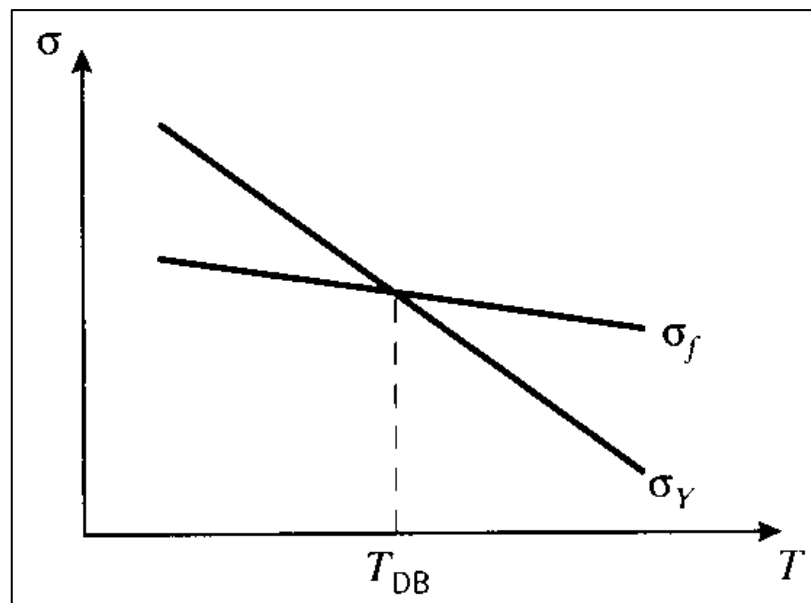

Figure 6: Schematic illustration of the temperature dependence of yield and fracture stress [7].

At high temperatures BCC metals have mobile dislocations, and thus they can sustain large plastic deformations before failing. At low temperatures however the mobility of BCC dislocations decrease. In BCC metals slip occurs in close-packed <111> directions. The shortest lattice vector, i.e. the Burgers vector of the perfect slip dislocation, is of the type ½ <111>. The crystallographic slip planes are {110}, {112} and {123}. In bcc materials dislocation motion is particularly complicated, due to the likelihood of cross-slip. In particular, three {110}, three {112} and six {123} planes share the same <111> direction, which makes it easy for screw dislocations to move around on different planes in a very ill-defined manner. It has been found that the apparent slip plane varies with composition, crystal orientation, temperature and strain rate. Thus, when pure iron is deformed at room

temperature the slip plane appears to be close to the maximum resolved shear stress plane irrespective of the orientation, whereas when it is deformed at low temperatures slip tends to be restricted to a specific {110} plane. Many researchers state that only the {110} slip plane is active at low temperatures [8] [9].

The flow stress of BCC metals, i.e. the stress required to maintain plastic deformation after yield, increase rapidly with decreasing temperature. The flow stress increases to a point where the critical stress for deformation twinning is reached. In twinning each atom only moves a small distance relative to its neighboring atom. This happens much more quickly than slip, and is prevalently formed when there is few slip systems available. The shear process introduced by twin formation is favorable for bond breakage at the crack tip. At low temperature, twin formation and cleavage fracture are cooperative processes in brittle fracture. At higher temperature the twinning becomes weakened, and vanishes at DBTT accompanied by dislocation nucleation. The Schmid law assumes that the only stress component triggering plastic flow of the material is the projected shear stress on the slip system, in the direction of glide, which is called the Schmid stress. The other non-glide component, defined as the normal stress, does not have any effect on the plastic deformation. These assertions are applicable on FCC metals, however not on BCC metals. A feature of yielding is the asymmetry of slip. It is found, for example, that the slip plane of a single crystal deformed in uniaxial compression may be different from the slip plane, which operates in tension for the same crystal orientation. In other words, the shear stress to move a dislocation in one direction in a slip plane is not the same as the shear stress required to move it in the opposite direction in the same plane. Slip is easier when the applied stress is such that a dislocation would move in the twinning sense on {112} planes rather than the anti-twinning sense, even when the actual slip plane is not {112}. In BCC metals, twin and slip mechanisms share common slip systems and twinning is only observed when the temperature is very low and the strain rate is extremely high. In this context, the main source of the plastic deformation is the glide of dislocations, but the resistance to this movement in the twinning and anti-twining directions is asymmetric. This is called the twinning/anti-twinning asymmetry of BCC crystals in the literature and the source of this asymmetry is the strong coupling of the screw dislocation to the BCC lattice, which constrains the core and its properties to adopt the symmetry of the lattice [8] [9].

Low temperature deformation in BCC metals has a strong difference in dislocation mobility between screw and other dislocations characters. Screw dislocations moves slow, the mobility of screw dislocations is therefore expected to control the flow stress. The screw core in BCC metals has a distinctive non-planar character. Each of the slip planes {110}, {112} and {123} contains <111> slip directions and it is particularly significant that three {110}, three {112} and six {123} planes intersect along the same <111> direction. Thus, if cross slip is easy it is possible for screw dislocations to move in a haphazard way on different {110} planes or combinations of {110} and {112} planes, favored by the applied stress. This leads to high lattice resistance to glide of the screw dislocation and strongly restricts screw dislocation mobility. Consequently resulting in a temperature and strain-rate dependencies of the yield and flow stress [10].

D Calliard has reported two papers [11] [12] on kinetics of dislocations in pure iron by means of in situ TEM staining experiments at both room temperature and at low temperature. Figure 7 shows a dislocation source rotating around a pinning point S at room temperature. There is a slow motion of two opposite screw segments and a fast motion of non-screw parts. Indicating that straight screw dislocations glide slowly in {110} elemental slip plane, at a velocity

proportional to their length, whereas curved non-screw parts are highly mobile. Figure 8 shows a dislocation movement at 110K. In this lower temperature range, straight screw segments have a jerky motion in {110} planes, in contrast to the steady motion observed at room temperature.
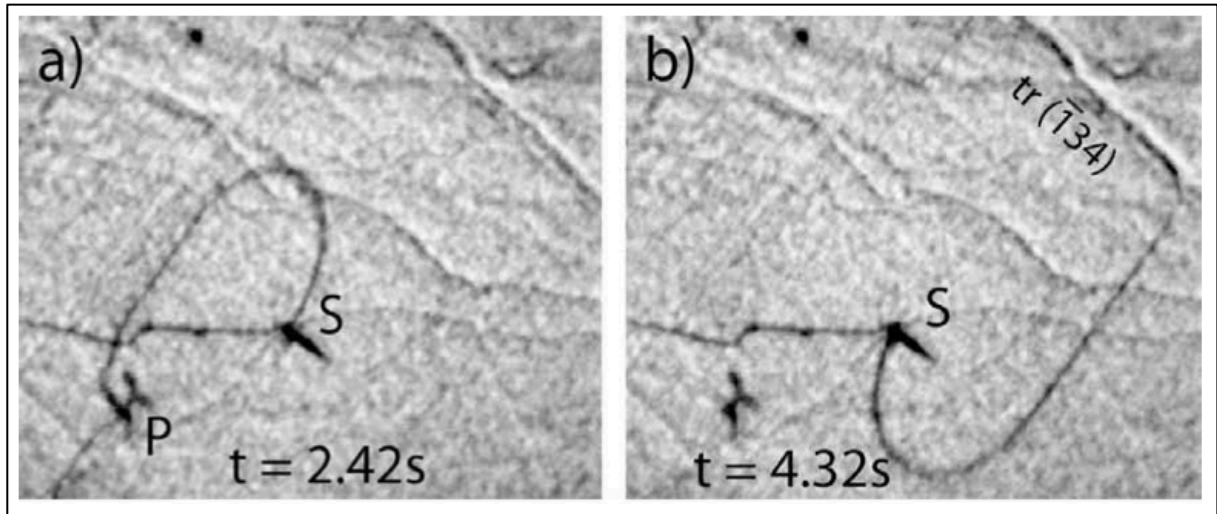

Figure 7: Slow movement of strait screw segments and fast movement of non-screw parts in iron at room temperature [11].
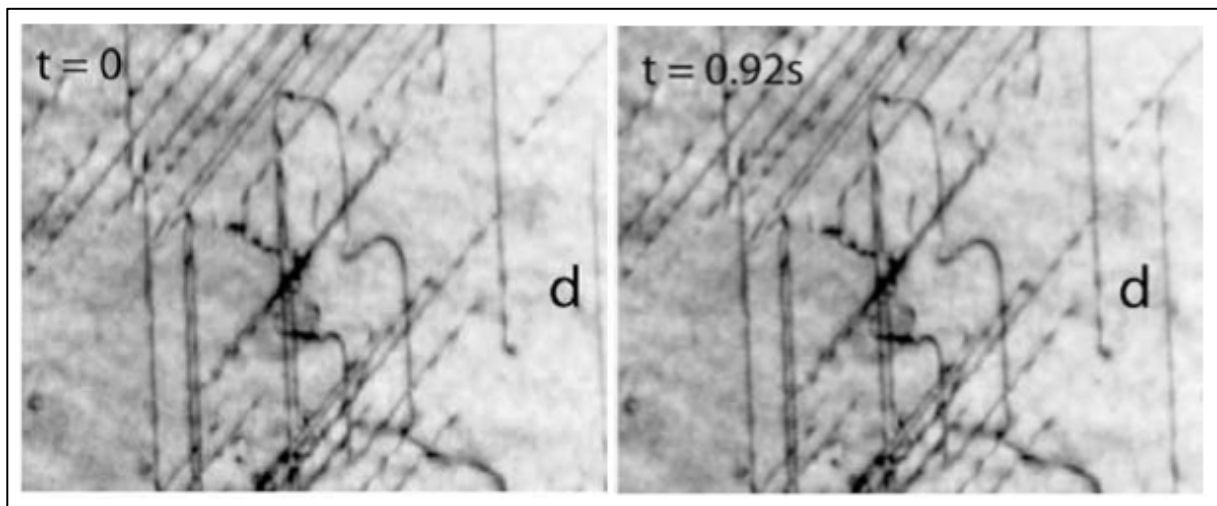

Figure 8: Jerky motion of straight screw segments at 110K [12].

D Calliard later presented a presented another paper [13] analyzing the velocity of screw dislocations in pure iron, as a function of temperature, by means of in-situ TEM straining experiments. Because of the rotational symmetry around the <111> densest direction of slip, the glide resistance is highest for screw dislocations, which have a threefold non-planar structure. Figure 9 shows an example of a dipole expansion with burgers vector ½ <111> in {110} plane at 113K. During the first 0,04s the curved non-screw parts move rapidly to the top and emerges at the foil surface. This leaves two straight screws, which subsequently move relatively slowly apart at increasing velocity.
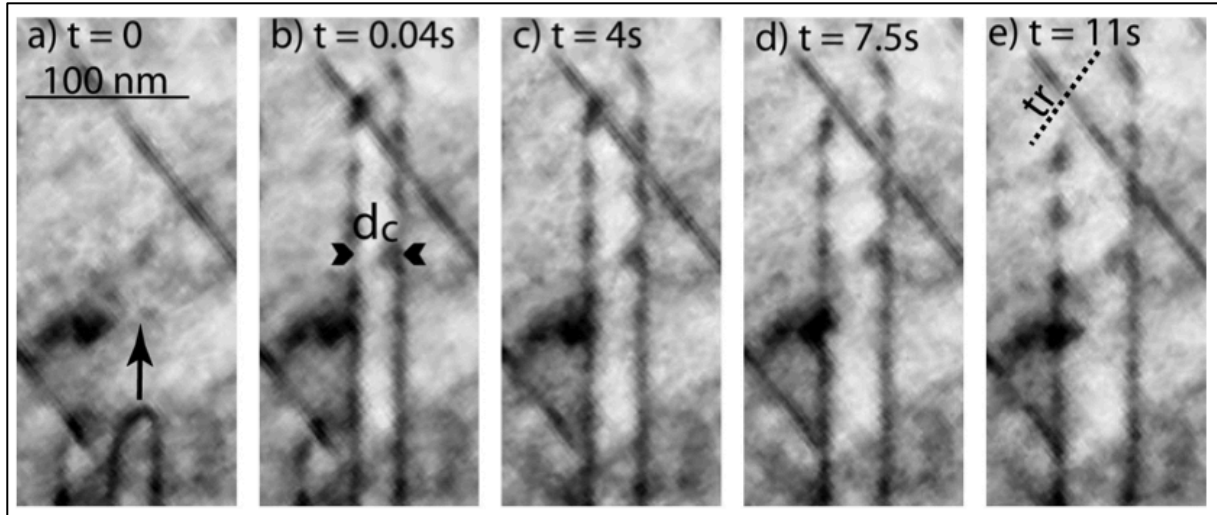
Figure 9: Fast motion of non-screw parts between a) and b), and slow motion of straight vertical screw segments between b) and b), at 113K [13].

2.1.5 Multiple barrier model

Perlade et al. [14] have proposed a so-called multiple-barrier model for cleavage fracture. In this model it is recognized that in order to result in macroscopic brittle fracture, there are several different barriers that have to be overcome. Cleavage fracture of steels most frequently occurs by the dynamic propagation of micro-cracks initiated by slip-induced cracking of brittle second phase particles i.e. carbides or inclusions. Fracture results from the successive occurrence of three elementary events: cracking of a brittle particle, propagation of the micro-crack across the particle/matrix interface and propagation micro-crack across grain boundary.
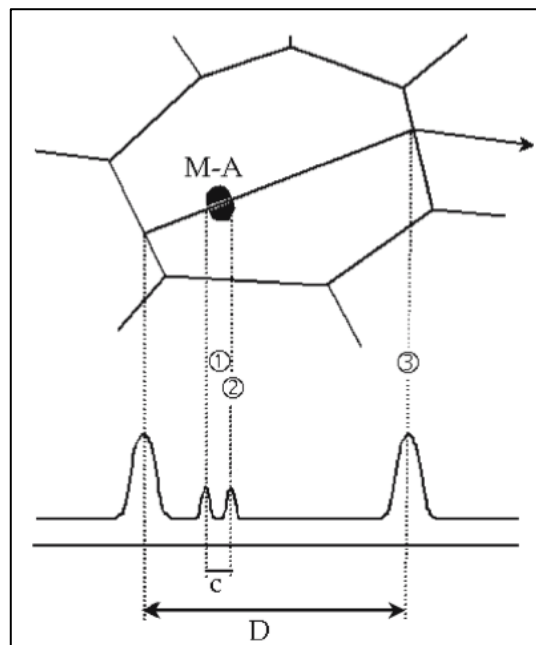
Figure 10: Initiation of a cleavage micro-crack from a particle [5].

A more detailed description of the three step is as followed. Step 1 represents slip-induced crack initiation at or near brittle particle/MA constituent, that immediately reaches the particle /matrix interface. Step 2 exemplifies micro-crack propagation into the matrix across the

7

particle/matrix interface, under the local stress state. The final step, step 3, represent propagation of the grain-sized crack across matrix/matrix interface into the neighboring grain, leading to final fracture.

The micro-mechanisms operating during fracture toughness measurements at increasing temperature are not necessarily the same. In such conditions it would seem preferable to involve a multiple-barrier model to account for the temperature dependence of fracture toughness. Using the weakest link assumption the fracture probability of the specimen is then given by the combine probabilities of these events.

The stress required to propagate a crack through a matrix/matris interphase (σ_{mm}) is low at low temperature, and is assumed to increase with increasing temperature. At elevated temperatures σ_{mm} becomes higher than the stress required for a crack to propagate through a particle/matrix interphase (σ_{pm}). If σ_y is the yield stress of the material and σ_I is the local maximum stress, the effect of temperature on the failure micro-mechanism can be described by considering the four temperature rages as followed.

At very low temperature, $\sigma_{mm} < \sigma_{pm} < \sigma_y$. Final fracture will occur immediately after fracture of the small particle, because σ_I is already higher than σ_y. Thus at very low temperature, fracture is nucleation controlled. At somewhat higher temperature, $\sigma_{mm} < \sigma_{pm}$ but $\sigma_y < \sigma_{pm}$. Upon loading, σ_I increases and micro crack propagates from particle to particle/matrix interface and stop there. As soon as $\sigma_y < \sigma_I < \sigma_{pm}$, i.e the local stress at P/M interface is higher than the σ_y, the crack will propagate into matrix. Failure is controlled by the strength of particle/matrix interface. At high temperature the strength of the matrix/matrix interfaces is high and $\sigma_y < \sigma_{pm} < \sigma_{mm}$. Upon loading σ_I increase and the crack is stopped at a matix/matrix interphase, additional loading increase σ_I further and as soon as $\sigma_I > \sigma_{mm}$ the crack propagates through the grain boundary. Crack propagation is controlled by strength of matrix/matrix interface; witch is strongly influenced by the rotational and angular miss-orientation of the grains. At even higher temperature, σ_{mm} is very high, ductile fracture occurs (possible initiated from particles) before the cleavage cracking can develop.
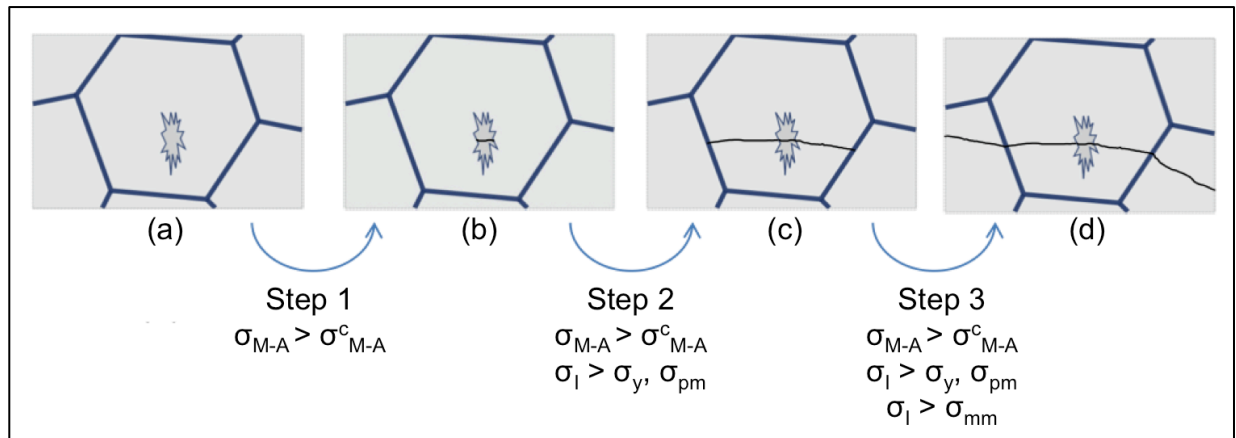

Figure 11: Illustration of the multiple barrier model, adapted from [14].

Application of a multiple barrier model puts more requirements for determination of material properties. The crack-arrest properties of the material will play an important role. A challenge related to this would be to obtain quantitative information on local stress requirements for crack propagation. Nanomechanical fracture experiments may be applicable; firstly however a fundamental understanding of fracture experiments on a small scale is necessary.

2.2 Focused Ion beam milling (FIB)

The FIB instrument is similar to a scanning electron microscope (SEM), except that the beam that is rastered over the sample is an ion beam (usually gallium) rather than an electron beam. When a high energy Ga^+ ion hit the sample surface it will interfere with the surface material trough elastic and inelastic interactions. The inelastic energy transfer happens when the ion energy is transferred to electrons in the sample. This results in ionization followed by emission of secondary electrons (SE) and electromagnetic radiation from the sample. In the elastic interaction the Ga^+ ions is colliding into the sample atoms followed by series of collisions in the form of a collision cascade. If the kinetic energy from the Ga^+ ion atom exceeds a critical value, the displacement energy, the atom will be displaced out of position. A surface atom displaced out of its position might emit or sputter from the surface. At low primary beam currents, very little material is sputtered. The ejected SE and sputtered ions i.e. positively charged secondary ions (SI) can be collected to form an image. At high primary currents, a great deal of material can be removed by sputtering. The sputtering effect allows milling i.e. precise local removal of material. By means of milling desired 3D geometries can be machined at a nanoscale. [15] Ion beam imaging always results in some sputtering or damage of the sample surface. Most instruments combine a SEM and FIB column; this is called DualBeam. Generally the ion beam will be used for milling and the electron beam for imaging. This allows non- destructive imaging at higher magnifications and more accurate control of the milling progress.

2.2.1 Sputtering yield

Sputter yield is the ratio of the number of the target atoms ejected to the number of ions incident on the target. Quantitative aspects of sputtering are complicated and depend on the material, crystal orientation, ion beam incidence angle, and sample topography. When milling areas with variations in microstructure or mass, grain orientation and topography it is difficult to obtain an even sputtering rate. A free path, i.e. low collision between Ga^+ and sample atoms results in low sputtering yield, and high collision between Ga^+ and sample atoms result in a high sputtering yield. Figure 12 a) and b) illustrates the effect of crystal direction. For figure a) Ga^+ ions will easily move deep into sample, because of the spacing between the atoms due to the orientation of the grain. While in figure b) the Ga^+ ions will early collide into sample atoms. Figure c) illustrates the effect of topography; more material will escape close to a free surface area [15].
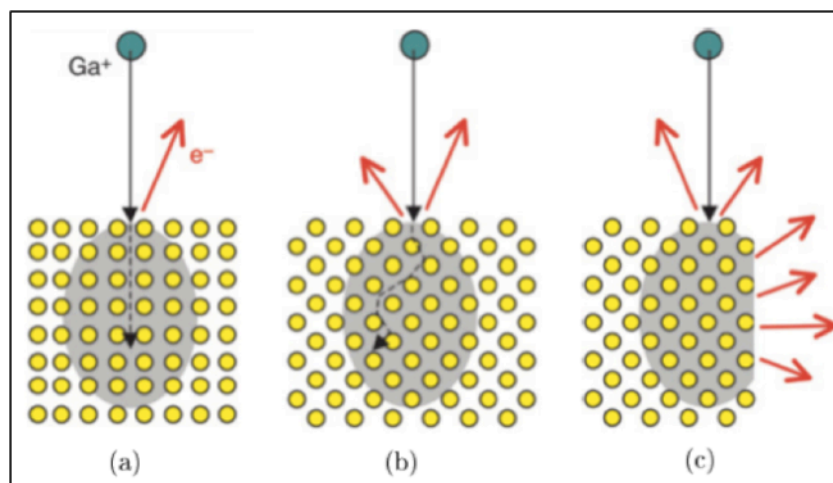
Figure 12: Illustration of the influence of crystal orientation
(a,b) and surface topography (c) on sputtering yield [15].

2.2.2 Re-deposition

Re-deposition is a serious negative complication to milling. As material is sputtered away, some of it will be re-deposited. Re-deposition decreases the effective sputter rate and may alter sputter profiles. The decreased rate is due to the fact that re-deposited material, landing in the area being milled, has to be sputtered a second time. When milling specific geometries the use of several milling steps and pattern geometries is often necessary. This results in re-deposition of sputtered material on already milled surfaces, and thereby changing the sputtered profile and creating unwanted features. The location of re-deposited material is extremely hard to predict and control. Material ejected from the sample during sputtering emerges with a variety of trajectories, and geometrical effects from structural features will affect the location of the re-deposited material.

Re-deposition also limits the depth of the milled patterns. As the beam mills deeper into the sample, sputtered material is not ejected from the crater but remains within it, resulting in a competition between re-deposition and sputtering. Figure 13 shows a schematic view of the milling process of a pillar. The milling process starts at a large diameter and works its way in to the desired diameter of the pillar. During the process sputtered material is re-deposited on the outer end of the circle.
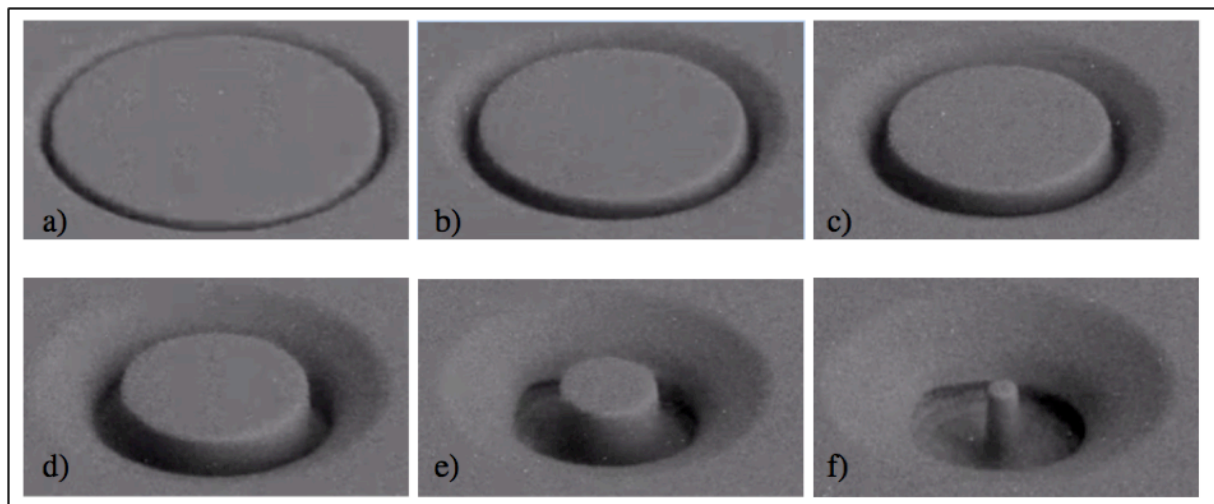
Figure 13: Schematic view of milling process, showing re-deposition of sputtered material [16].

2.2.3 Cantilever fabrication

Milling makes it possible to machine out cantilever samples at a micro scale, and has been performed using a variety of materials. Fracture experiments at micro scale allow local mechanical properties to be evaluated. By this it is possible to investigate selected areas within crystalline materials. The milling quality is dependent on the ability to operate the beam to remove the required amount of material from a defined area in a controllable manner. A selection of different techniques has been reported in the literature, and will be summarized in the following section.

One method is to machine cantilevers on a bulk sample [17] [18] [19] [20] [21]. In order to remove base material and produce a freestanding cantilever the sample must be tilted. For the first bottom edge the sample will be tilted 45° with respect to ion beam. The second bottom edge is accessed by a 180° rotation with respect to the sample. It is however not possible to produce a square cross-section, due to the configurations of the stage movement in the FIB. The achievable geometries by this technique have a symmetric cross section on the vertical axis, but not in the rectangular axis. Figure 14 illustrates the main steps of the milling procedure and finished freestanding cantilevers, both with a triangular cross-section and with pentagon cross-section. When loading the cantilever with a pentagon cross-section a constant crack width during the initial crack growth is maintained.

This method requires very little sample preparation, only basic grinding and electropolishing. Another advantage with this method is that the cantilevers can be machined at any site, resulting in large prospective areas. This makes the method extremely flexibility in regards to choose specific areas. However, the milling procedure involves removal of large amounts of material. When assuming the quantity of removed material to be proportional to milling time, it becomes obvious that it is extremely time consuming, especially if a series of cantilevers is necessary. Milling removal of large amounts of material may also accumulate FIB damage and alter the structure of the material by ion implantation [22].
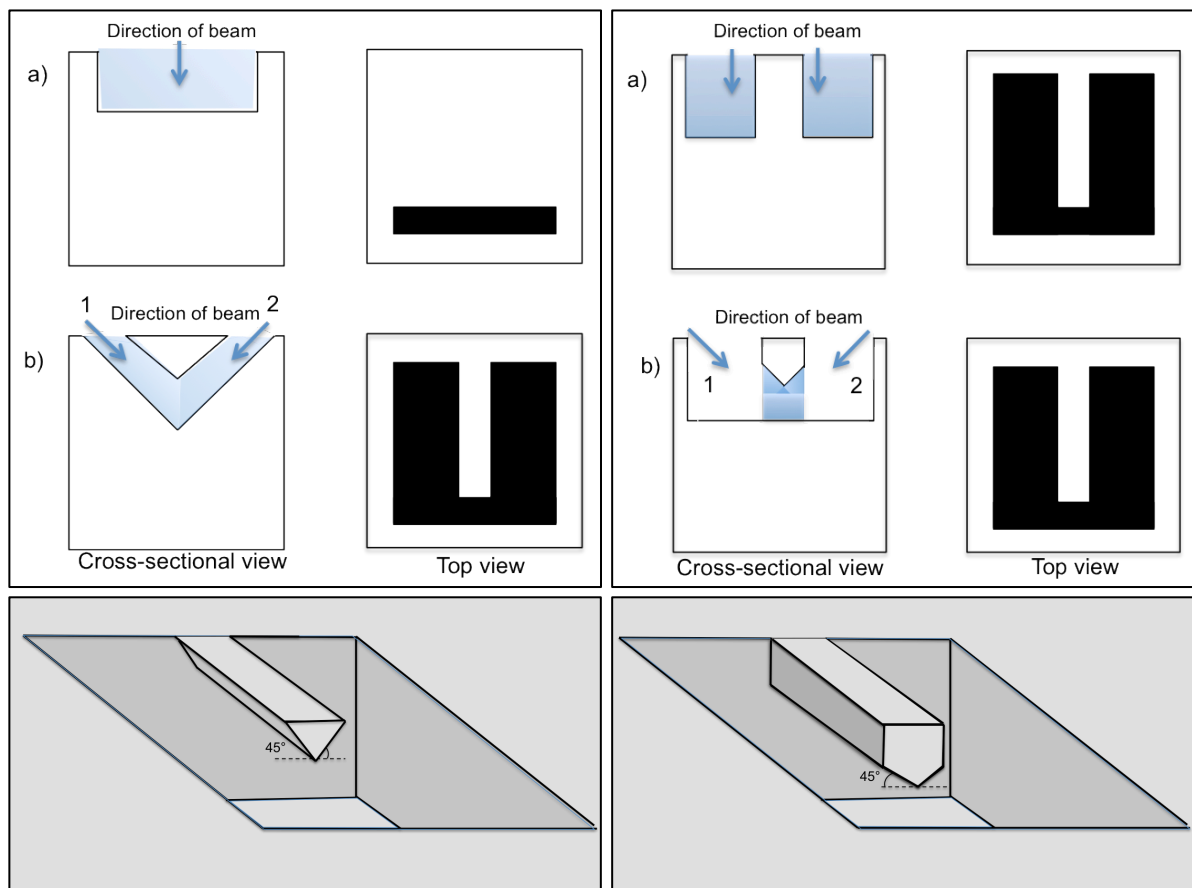
Figure 14: Schematic view of cantilever fabrication in bulk sample with triangular (left) and rectangular cross-section (right).

A second method to fabricate cantilevers is to utilize the free space around the edge of a bulk sample. From a near edge region it is possible to achieve a rectangular cross-section [23] [24] [25] [26] [27]. Figure 15 shows the milling procedure and finished cantilevers with a rectangular cross-section. The horizontal cantilevers requires a manual 90° rotation of the sample. When milling the vertical cantilever no tilting of the sample is necessary. One drawback with the vertical cantilevers is that it is machined rather deep into the bulk sample. If specific area of inters is located by means of EBSD, only the surface is scanned and characterized, leaving the subsurface area undetermined.

By machining cantilever with a rectangular cross-section a constant crack width during loading is maintained. However, this method requires a more thorough sample preparation, since a good surface condition and a sharp edge after grinding and electropolishing is required. Since the cantilever fabrication is restricted to the edges of the sample the prospective areas is limited. The milling procedure involves removal of approximately the same amount of material as the previously describe technique. Milling removal of large amounts of material is as mention time consuming and may accumulate FIB damage.
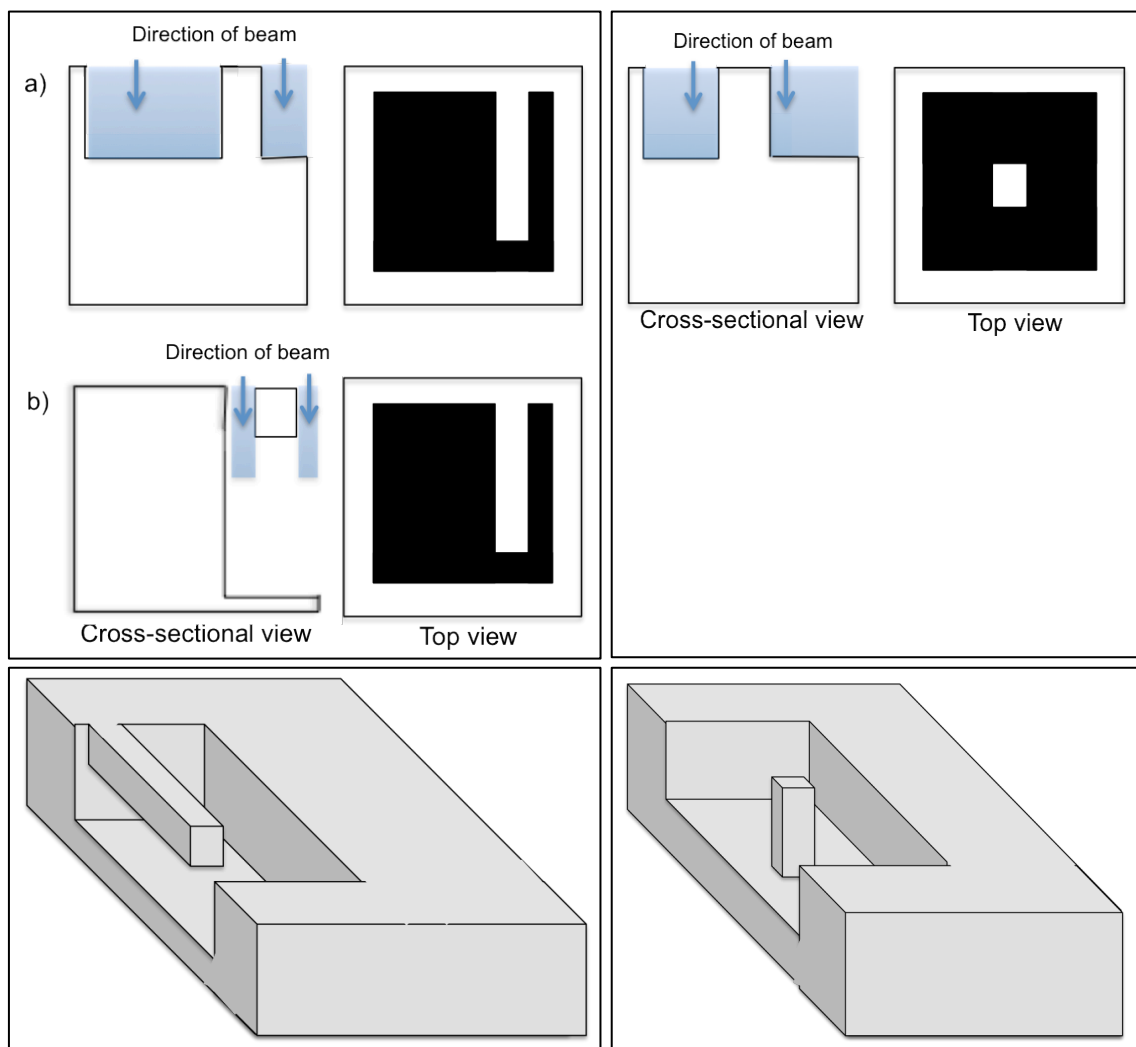
Figure 15: Schematic view of cantilever fabrication on edge of bulk sample with rectangular cross-section, horizontal cantilever (left) and vertical cantilever (right).

A third method is to machine cantilevers on lamellas with a width of some few micrometers. This technique simplifies the milling procedure significantly. Furthermore the milling time is lowered considerably, as hardly any bulk material has to be removed. Figure 16 illustrates the milling procedure and the finished cantilever with a rectangular cross-section. The cantilevers can be machined at any site of the thin film resulting in flexibility regarding specific area selection. This method however requires a more comprehensive sample preparation.

This method has been widely used in testing of thin films [28] [29] [30] [31]. However it is possible to produce a similar thin film from a bulk sample by altering the purpose of a Transmission Electron Microscopy (TEM) sample. The ion slicing technique is well-known preparation method of manufacturing thin freestanding lamellae with a width of some micrometers. Using this ion slicing technique in the first step of the sample preparation will presumable reduce the ion damage in comparison to pure FIB milling, due to the lower acceleration voltage and the use of argon ions instead of gallium [32] [33].
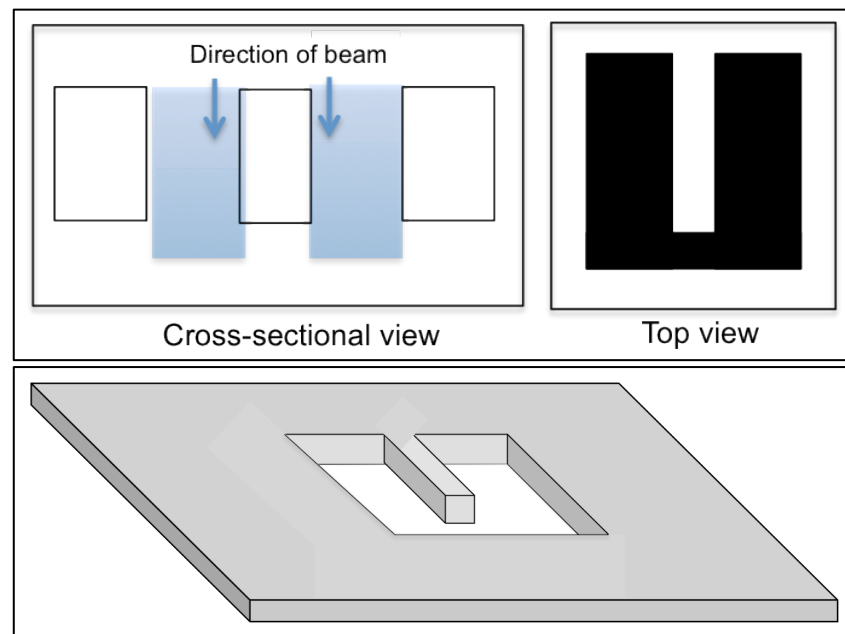
Figure 16: Schematic view of cantilever fabrication with rectangular cross-section on thin film sample.

2.3 Fracture toughness

The K factor was proposed in 1957 by Irwin to describe the intensity of elastic crack-tip fields, and symbolizes the linear elastic fracture mechanics. The stress intensity factor (K) is used to predict the stress state near the crack tip caused by an applied load, and is useful for providing a failure criterion for brittle materials. As the stress intensity factor reaches a critical value fracture occur, this critical value is known as the fracture toughness (K_{IC}) of the material [34].

Picoindentaion may be used to measure the fracture toughness of FIB fabricated micro-cantilever. During the course of the indentation process the load and displacement of the indenter are recorded with very high accuracy and precision. The principle of mechanical bending of cantilevers by indentation is to apply a load with the indenter tip at the edge of the free extremity of the cantilever, and measure the critical load to cause unstable fracture from a pre-existing crack.

2.3.1 Cantilevers with square cross-section

The fracture toughness is dependent on sample geometry, the size and location of the crack and the magnitude of the load. There are several different approaches to calculate the fracture toughness for a micro-cantilever. The following section will present the three main approaches, reported in the literature, for cantilevers with square cross-section, as shown in Figure 17.
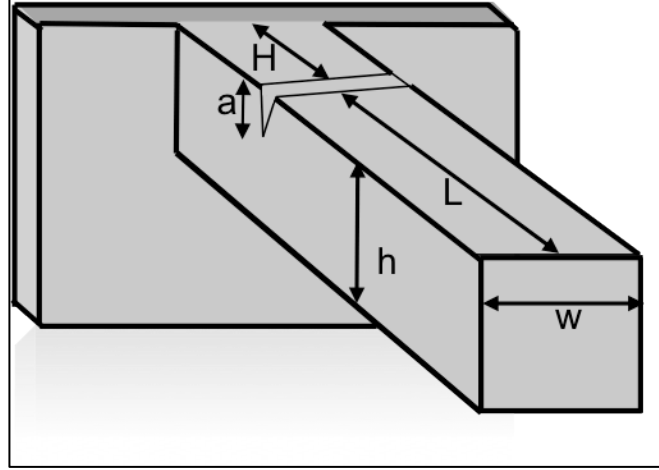
Figure 17: Illustration of a cantilever with a square cross-section.

Armstrong et al. [35] and Takashima et al. [28] [29] have used equations (1) to (3) to calculate the fracture toughness for single edge notched micro-cantilever beam specimens. This approach does not apply to a specific beam geometry, and is used for several different L:h:w ratios.

The critical stress at which the cantilever fractures is used to calculate the fracture toughness

$$K_{Ic} = \sigma_f \sqrt{\pi a}\, f\left(\frac{a}{h}\right) \tag{1}$$

The bending stress on the beam top surface, is given by the linear elastic bending theory

$$\sigma = 6\frac{FL}{wh^2} \tag{2}$$

The dimensionless shape factor $f\left(\frac{a}{h}\right)$ is given by

$$f\left(\frac{a}{h}\right) = 1{,}22 - 1{,}40\left(\frac{a}{h}\right) + 7{,}33\left(\frac{a}{h}\right)^2 - 13{,}08\left(\frac{a}{h}\right)^3 + 14{,}0\left(\frac{a}{h}\right)^4 \tag{3}$$

Wurster et al. [36] used used the fracture toughness equation for a three-point-bending specimen according to ASTM standard E399-12 [37].

$$K = \frac{FS}{wh^{3/2}} \, f\left(\frac{a}{h}\right) \qquad (4)$$

In order to converting the equation for a three-point-bend test to a one-point-bend test Wuster et al. include a factor of 4 since

$$F = \frac{F_{3PB}}{2} \; and \; L = \frac{S_{3PB}}{2}$$

$$K = \frac{4FL}{wh^{3/2}} \, f\left(\frac{a}{h}\right) \qquad (5)$$

The same authors later presented a paper [33] using the equation without the additional factor of 4. This approach does not apply to a specific beam geometry, and is used for several different L:h:w ratios.

The dimensionless shape factor for the above equation is given ASTM E399-12. Wurster et al. used Finite Element Method (FEM) and ABAQUS code to obtain a more detailed analysis of the dimensionless shape factor. Two dimensional, plane stress 8-node biquadratic elements (CPS8) were used. In contrast to the ASTM E399-12 equation, where plane-strain conditions are assumed, plane stress was chosen. Plane stress was used since the size of the sample was so small that surface effects and hence a plane stress field are supposed to prevail.

$$f\left(\frac{a}{h}\right)_{ASTM\,E399-09} = \frac{3\left(\frac{a}{h}\right)^{0,5}\left(1,99-\left(\frac{a}{h}\right)\left(1-\left(\frac{a}{h}\right)\right)\right)\left(2,15-3,93\left(\frac{a}{h}\right)+2,7\left(\frac{a}{h}\right)^{2}\right)}{2\left(1+2\left(\frac{a}{h}\right)\right)\left(1-\left(\frac{a}{h}\right)\right)^{1,5}} \qquad (6)$$

$$f\left(\frac{a}{h}\right) = 4\frac{3\left(\frac{a}{h}\right)^{0,5}\left(1,23-\left(\frac{a}{h}\right)\left(1-\left(\frac{a}{h}\right)\right)\right)\left(-6,09+13,96\left(\frac{a}{h}\right)-14,05\left(\frac{a}{h}\right)^{2}\right)}{2\left(1+2\left(\frac{a}{h}\right)\right)\left(1-\left(\frac{a}{h}\right)\right)^{1,5}} \qquad (7)$$

Matoy et al. [38] and Schaufler et al. [39] also used equation for a three-point-bend test, with the maximum force to calculate the fracture toughness. In these papers the additional factor of 4 was not used.

$$K_{IC} = \frac{F_{max}L}{wh^{3/2}} \, f\left(\frac{a}{h}\right) \qquad (8)$$

However a different dimensionless shape factor is reported. Matoy et al. used the same method of FEM simulations using ABAQUS code. The facture toughness for different a/h ratios was recorded and the function for the shape factor was derived by a cubic fit of the function

$$\frac{K_{IC} w h^{3/2}}{F_{max} L} \ vs \ \left(\frac{a}{h}\right) \tag{9}$$

This shape factor is valid for a/h-ratios between 0,05 and 0,45, and determined for a specific aspect ratio i.e. beam dimension of H:L:h:w = 2:5:2,1:1,7.

$$f\left(\frac{a}{h}\right) = 1,46 + 24,36\left(\frac{a}{h}\right) - 47,21\left(\frac{a}{h}\right)^2 + 75,18\left(\frac{a}{h}\right)^3 \tag{10}$$

During FIB milling it is almost impossible to exactly control the beam dimensions. Iqbal et al. [40] chose different aspect ratios to evaluate if this could affect the resultant geometry factor values. Two different aspect ratios were chosen; H:L:h:w = 2:5:2,1:1,3 → w/h = 0,6 and 2:5:2,1:1,7 → w/h = 0,8. The calculated geometry factor with their derived cubic polynomial fitting is shown in Figure 18 and Figure 19. The measured geometry factor showed in equations (11) and (12) was in good agreement with Matoy et al.

$$\frac{w}{h} = 0,8 \rightarrow \quad f\left(\frac{a}{h}\right) = 1,52 + 24,184\left(\frac{a}{h}\right) - 48,422\left(\frac{a}{h}\right)^2 + 77,608\left(\frac{a}{h}\right)^3 \tag{11}$$

$$\frac{w}{h} = 0,6 \rightarrow \quad f\left(\frac{a}{h}\right) = 1,603 + 23,055\left(\frac{a}{h}\right) - 43,755\left(\frac{a}{h}\right)^2 + 72,106\left(\frac{a}{h}\right)^3 \tag{12}$$
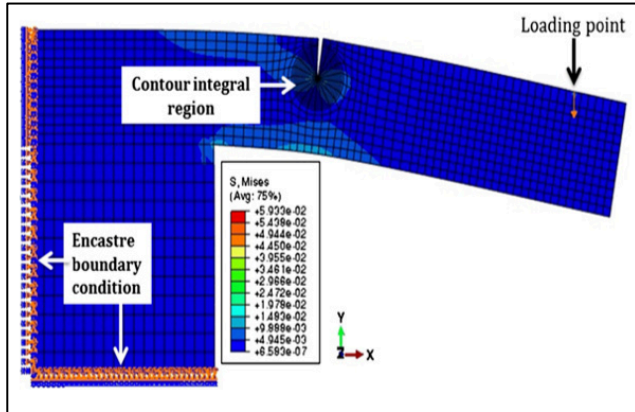
Figure 18: 2-D finite element modeling for determination of geometry factor. Model geometry with boundary conditions [40].
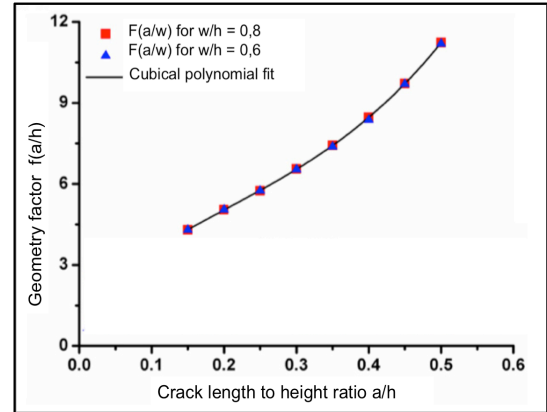
Figure 19: Geometry factors for cantilever beams with different w/h ratios plotted as a function of a/h, adapted from [40].

2.3.2 Cantilevers with a pentagon cross-section

To the best of my knowledge only two papers has reported a thorough review of the fracture toughness calculations for cantilevers with a pentagon cross-section. Zhao et al. [20] suggested the following approach
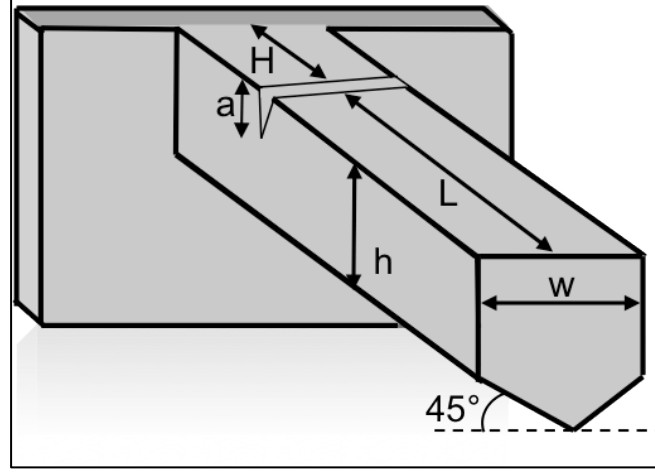
Figure 20: Illustration of cantilever with pentagon cross-section

The fracture stress was approximated as

$$\sigma_f = \frac{FLy}{I} \tag{13}$$

Where the moment of inertia of the beam's cross-section was calculated by

$$I = \frac{wh^3}{12} + \left(y - \frac{h}{2}\right)^2 hw + \frac{w^4}{288} + \frac{w^2}{4}\left[\frac{h}{6} + (h - y)\right]^2 \tag{14}$$

Where y is the vertical distance between the upper surface and the neutral plane, which were expressed

$$y = \frac{\frac{h^2 w}{2} + \frac{w^2}{4}\left(h + \frac{w}{6}\right)}{hw + \frac{w^2}{4}} \tag{15}$$

The critical stress at which the cantilever fractures was used to calculate the fracture toughness

$$K_{Ic} = \sigma_f \sqrt{\pi a}\, f\left(\frac{a}{h}\right) \tag{16}$$

Where the dimensionless shape factor was calculated by

$$f\left(\frac{a}{h}\right) = 1.122 - 1.121\left(\frac{a}{h}\right) + 3.74\left(\frac{a}{h}\right)^2 + 3.873\left(\frac{a}{h}\right)^3$$
$$- 19.05\left(\frac{a}{h}\right)^4 + 22.55\left(\frac{a}{h}\right)^5 \tag{17}$$

17

Maio and Roberts [41] used a similar approach in order to calculate the fracture toughness for micro-cantilevers with a pentagon cross-section. However a slight difference in the moment of inertia equation is reported. As seen in equation (18) an additional factor of $\frac{w^2}{4}$ is used

$$I = \frac{wh^3}{12} + \left(y - \frac{h}{2}\right)^2 hw + \frac{w^4}{288} + \frac{w^2}{4}\left[\frac{h}{6} + (h - y)\right]^2 \frac{w^2}{4} \tag{18}$$

This paper also reports a different dimensionless shape factor

$$f\left(\frac{a}{h}\right) = 1{,}85 - 3{,}38\left(\frac{a}{h}\right) + 13{,}24\left(\frac{a}{h}\right)^2 - 23{,}26\left(\frac{a}{h}\right)^3 + 16{,}8\left(\frac{a}{h}\right)^4 \tag{19}$$

2.3.3 Cantilever geometry effect on dimensionless shape factor

The dimensions of the FIB milled beams may change to some extent due to difficulties of accurately controlling the process. The dimensionless geometry factor is important, so it is necessary to validate the effect of these changes. A previous study attempted to validate these changes by fracture simulations of micro-cantilever beams using Finite element modeling [42]. It was found that the value of the stress intensity factor and the applied force vary with a change in these geometrical parameters. However, the ratio of the stress intensity factor and the applied force stay constant. This paper is based on the equations and experimental results from the previous mentioned paper Matoy et al. [38], with the dimensionless shape factor of

$$f\left(\frac{a}{h}\right) = 1{,}46 + 24{,}36\left(\frac{a}{h}\right) - 47{,}21\left(\frac{a}{h}\right)^2 + 75{,}18\left(\frac{a}{h}\right)^3 \tag{10}$$

First the effect of the crack length to height ratio (a/h) was evaluated. The obtained values of stress intensity factors were plotted against force for different crack to width ratios. The graph in Figure 21 shows that by changing a/h from 0.1 to 0.6 the curve shifted towards the y-axis, which indicates that for same force the larger the crack length the higher the stress intensity factor. The shape factors were calculated for different a/h ratios and then compared to literature values and was found in good agreement.

The effect of the width to height ratio (w/h) was estimated by using the same a/h ratio, as seen in Figure 22. The value of the stress intensity factor for same crack length to height ratio was higher in case of lower w/h ratios but displacement was lower for the same force. It was found that although stress intensity factors and force values are changed the geometry factors calculated had similar values. These results show that when the thickness of the specimen is changed it influences the values of the force and stress intensity factors but the ratio of stress intensity factor to force remains same. Therefore these results give us freedom to choose the thickness to width ratios.

Simulations were then performed to see the effect of loading point (L). The obtained results show the values of the stress intensity factors and force both decrease as seen in Figure 22 Then the geometry factor was calculated. It was found that calculated geometry factors values remain same for the different loading positions and are in good agreement with the literature value with only a deviation in the range of 0.4%.
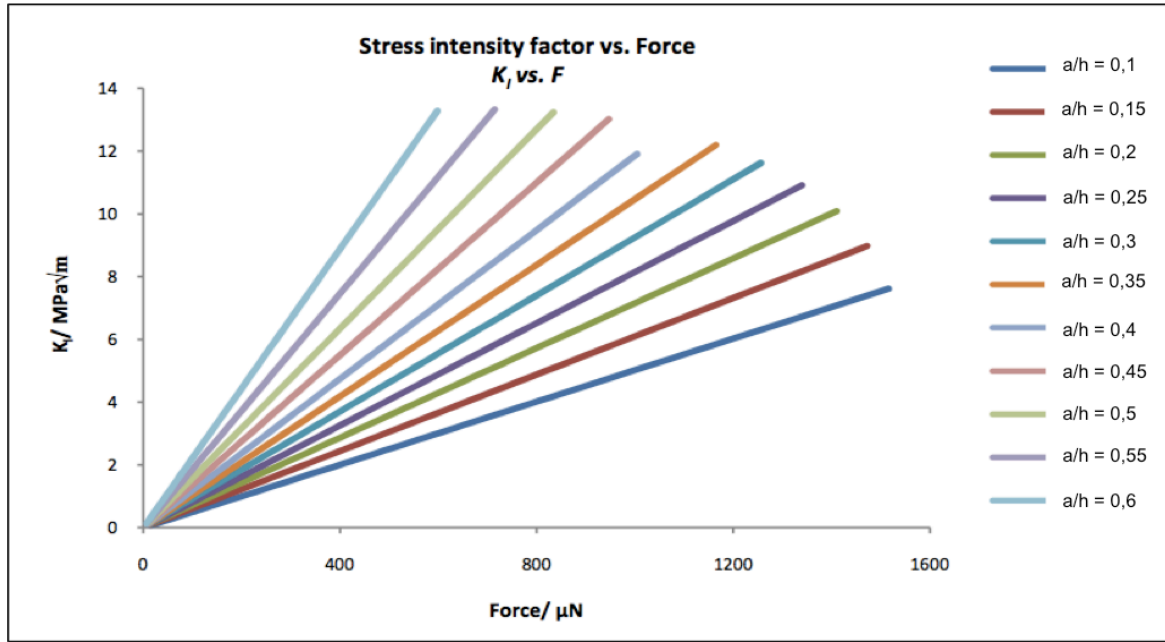
Figure 21: Stress intensity factor for different a/h ratios (w/h = 0,8), adapted from [42].
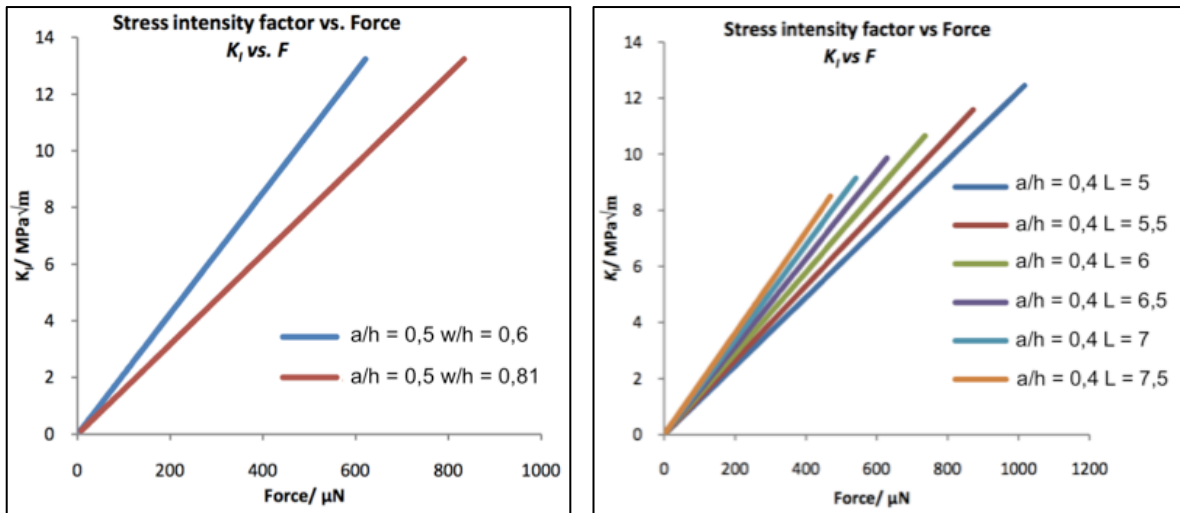
Figure 22: Stress intensity factor for different width to height ratio (w/h, and stress intensity factor for different cantilever lengths, adapted from [42].

2.4 Sample size effects

It is well known that the mechanical behavior at micronoscale differ from macroscopic samples. Metallic materials display significant size effects when the characteristic length scale of non-uniform plastic deformation is close to a micron: the smaller the size the stronger the material. The classical plasticity theories cannot predict this size dependence of material behavior at the micron scale because their constitutive models possess no internal length scale. Attempts to link macroscopic cracking to atomistic fracture are frustrated by the inability of conventional plasticity theories to model stress-strain behavior adequately at the small scales. Some microscopic understanding of plasticity is necessary in order to accurately describe deformation at small length scales.

2.4.1 Crack tip plasticity

The stress intensity factor satisfies only ideally brittle materials, yet most metals normally fail with certain amount of plastic deformation. Simple corrections to the linear elastic fracture mechanics are available when moderate yielding takes place, and may be applied to materials that exhibit small-scale yielding at a crack tip [34]. Nevertheless the stress intensity factor becomes increasingly inaccurate as the ductile behavior of the material increases. When calculating the stress intensity factor the stresses at the crack tip are infinity but in reality there is always a plastic zone that limits the stresses to finite values. The plastic zone is a simple concept to visualize. Within a certain radius of the crack tip, the yield stress is exceeded and the material deforms. Plasticity makes a large contribution to the energy absorbed in crack propagation because plastic deformation at the crack tip blunts the tip and substantially increases the amount of work required per unit crack advance.
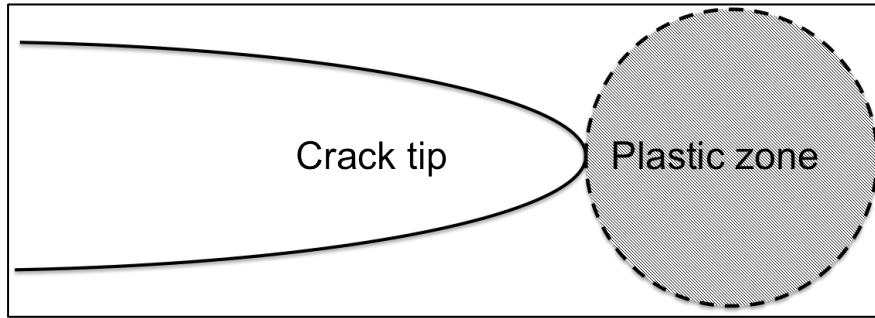
Figure 23: Illustration of plastic zone at crack tip

Inelastic material deformation such as plasticity leads to relaxation of the crack tip stresses. The elastic stress analysis becomes increasingly inaccurate as the inelastic region at the crack tip grows. The material in the plastic zone carries less stress than it would otherwise carry if the material remained elastic. When yielding occurs the stress must redistribute. The forces that would be present in an elastic material cannot be carried in an elastic-plastic material because the stress cannot exceed the yield. The plastic zone must increase in size to accommodate for these forces. A simple force balance leads to an estimate of the plastic zone size [43]

Plane stress
$$r_p = \frac{1}{\pi}\left(\frac{K_{IC}}{\sigma_y}\right)^2 \tag{20}$$

$$r_p = \frac{1}{6\pi}\left(\frac{K_{IC}}{\sigma_y}\right)^2 \tag{21}$$
Plane strain

Models of an elastic, perfectly plastic material have shown that the material outside the plastic zone is stressed as if the crack were centered in the plastic zone, as shown in Figure 25. Thereby softer material in the plastic zone may be accounted for by defining an effective crack length that is slightly larger than the actual crack size [43].

$$a_{eff} = a + \frac{r_p}{2} \tag{22}$$
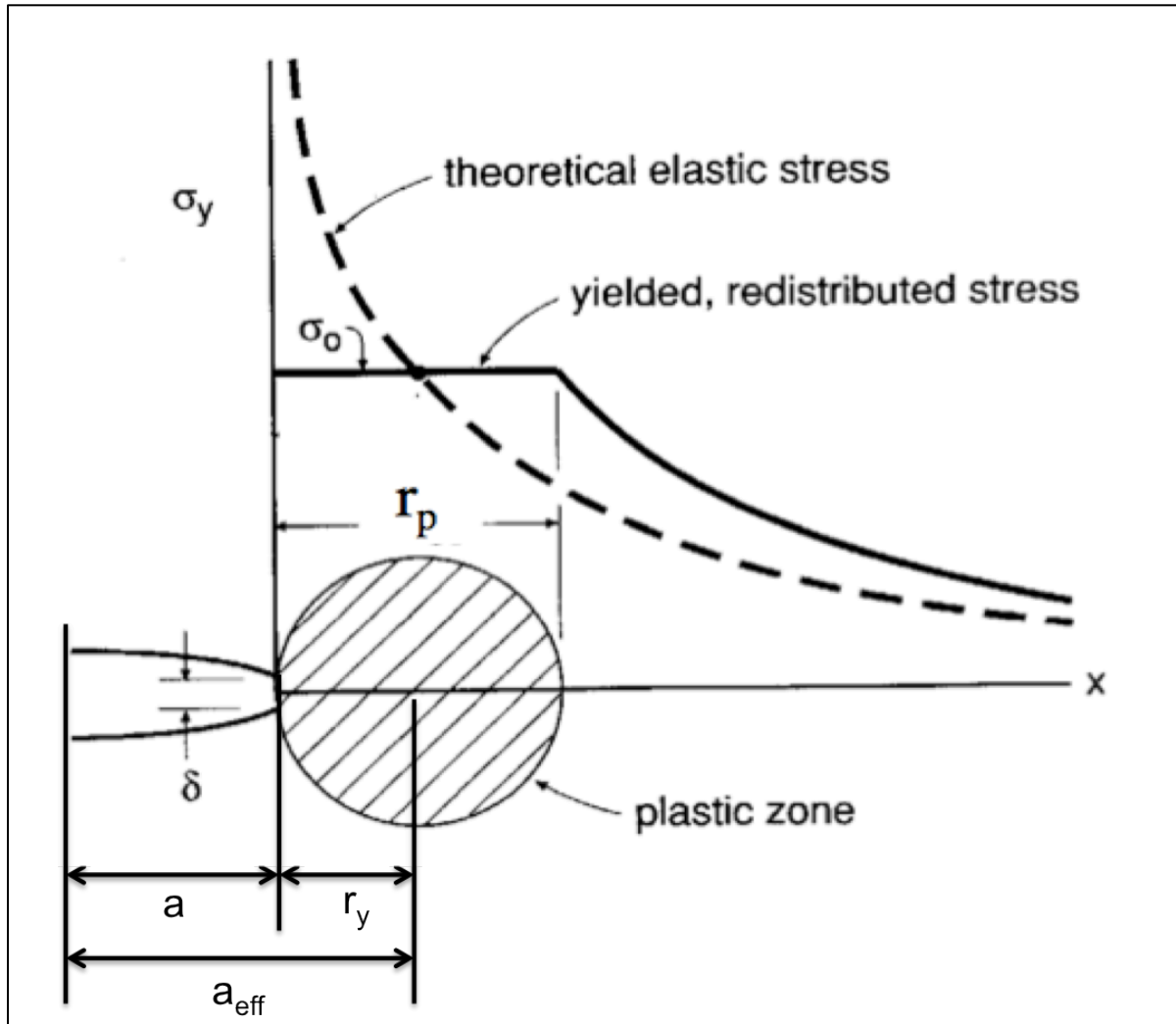
Figure 24: Plastic zone, adapted from [43].

With decreasing sample size the crack tip plasticity becomes increasingly important due to the extent of plasticity, relative to specimen dimension [44]. The size of the plastic zone has to be significantly smaller than the crack length in order for linear elastic fracture mechanics to be applied. Plastic distortion typically occurs at high stresses and the linear elastic solution is no longer applicable close to the crack tip [33]. For more extensive yielding it is necessary to apply alternative crack tip parameters that can take non-linear material behavior into account.

2.4.2 Stress state

The stress through the thickness of a thin plate cannot vary significantly because there are no stresses normal to a free surface, resulting in a biaxial state of stress. In plane stress conditions, there are no out-of-plane stress components but there can be significant out-of-plane deformation, and the material behaves with a significant amount of plasticity. For a thick plate however, the crack is constrained by the surrounding material causing a triaxial state of stress. In plane strain conditions there are little yielding, and the crack tip is loaded to higher stress, and will behave in a more brittle fashion.
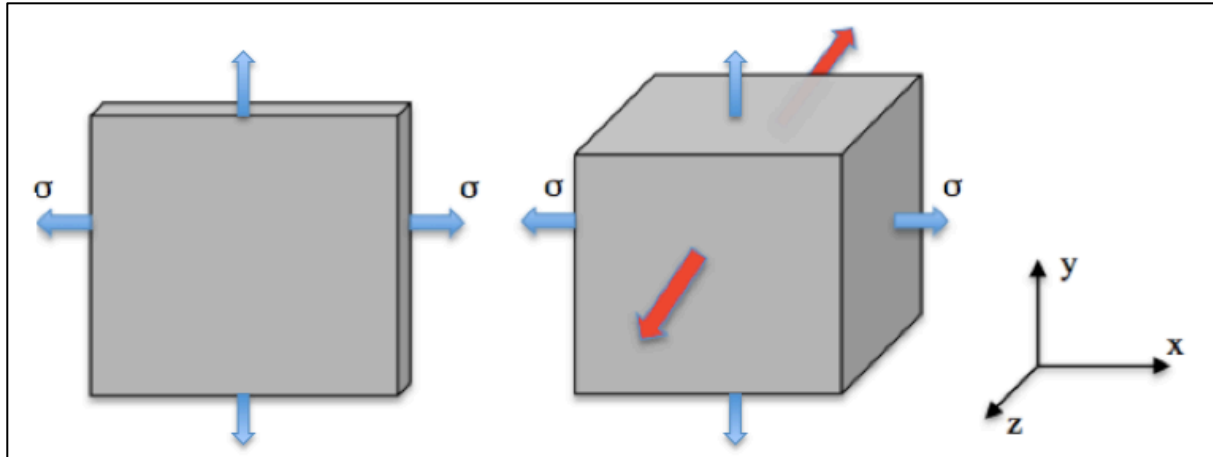
Figure 25: Plain stress (left), plain strain (right)

The stress state can have a significant effect on the fracture behavior. The critical thickness is that which causes the specimen to be dominated by a state of plane strain, as opposed to plane stress. The stress in the through-thickness direction must become zero at the sides of a thin specimen since no traction is applied there. In a thin specimen the stress will not have room to rise to appreciable values within the material. But when the specimen is thicker, material near the center will be unable to contract laterally due to the constraint of adjacent material. Now the through-thickness direction strain is zero, so a tensile stress will arise as the material tries to contract but is prevented from doing so.

The triaxial stress state at the crack tip near the center of a thick specimen reduces the maximum shear stress available to drive plastic flow. It can be stated that the mobility of the material is constrained by the inability to contract laterally. The extent of available plasticity is reduced with increasing sample size. On the microscale it is assumed that higher order stresses do not exist since the crack tip stress field is situated close to free surfaces due to the small sample size.

2.4.3 Dislocation movement

The increase in yield and flow stress of plastic deformation is commonly attributed to the presence of strain gradients in the deformation field. This strain gradient is accommodated by geometrically necessary dislocation (GND). GND represent an extra storage of dislocations required to accommodate the change in shape that arises whenever there is a non-uniform plastic deformation. For a cantilever under loading a certain number of dislocations must be designated to accommodate the curvature. These dislocations do not contribute to plastic strain but act as obstacles to the motion of other statically stored dislocations, and hence contribute to work hardening of the material. Whenever there is a non-uniform plastic deformation there will be an extra storage of material defects compared with uniform deformation at the same strain level. These defects manifest their effect when the characteristic length of deformation becomes sufficiently small. A bending test at millimeter length and above would not experience these effects because they are insignificant at macroscopic tests [45]

Motz et al. [26] attempted to explain the size effect with a common strain gradient plasticity approach. Cantilevers with thickness from 7,5 to 1,0 µm were fabricated with focused ion beam milling and subsequently loaded with a nonoindenter, and a strong size effect was found. They state that the strain gradient is equal to the curvature of the plastically deformed region. In order to accommodate strain gradient there exists a simple arrangement of GNDs as

shown in Figure 26. They assume arrays of dislocations, which perform a small amount of tilting of the crystal. A direct measurement of the strain gradient is not easy to perform. However, for a simple dislocation arrangement as shown in shown in Figure 26 there exist a direct correlation between the strain gradient and the gradient of the crystal orientation. Electron backscatter diffraction (EBSD) was performed and the strain gradient and increase in flow stress due to GNDs was calculated. This model could not explain the strong dependency of the flow stress. The real dislocation arrangement will differ from the simple illustration in Figure 26. It is likely that dislocation sources on more than one slip system will be activated resulting in a complex dislocation arrangement. In such case there would be a higher number of GNDs. However, even with a more complex dislocation arrangement an extremely high dislocation density is needed in order to explain the size effect. The paper suggests that there is a combination of three mechanisms that accommodate the observed size effect; strain gradient plasticity, dislocation pile-up at the center of the beam and limitation of available dislocation sources.

A more realistic dislocation distribution is shown in Figure 27, including the pile up of dislocations in the center of the beam. For clarity, only one type of slip system is chosen, which is aligned by an angle of 45° to the beam axis, which is the plane of maximum shear stress. A certain number of dislocation sources are assumed, one per slip plane, which limits the number of active slip planes. The shear stress decreases towards the center and reverses its sign at the center. Thus, the dislocation cannot move freely across the beam center. Subsequently emitted dislocations will form a pile-up at the center that shields the dislocation source. The applied stress, the bending moment, has to be increased for further deformation.
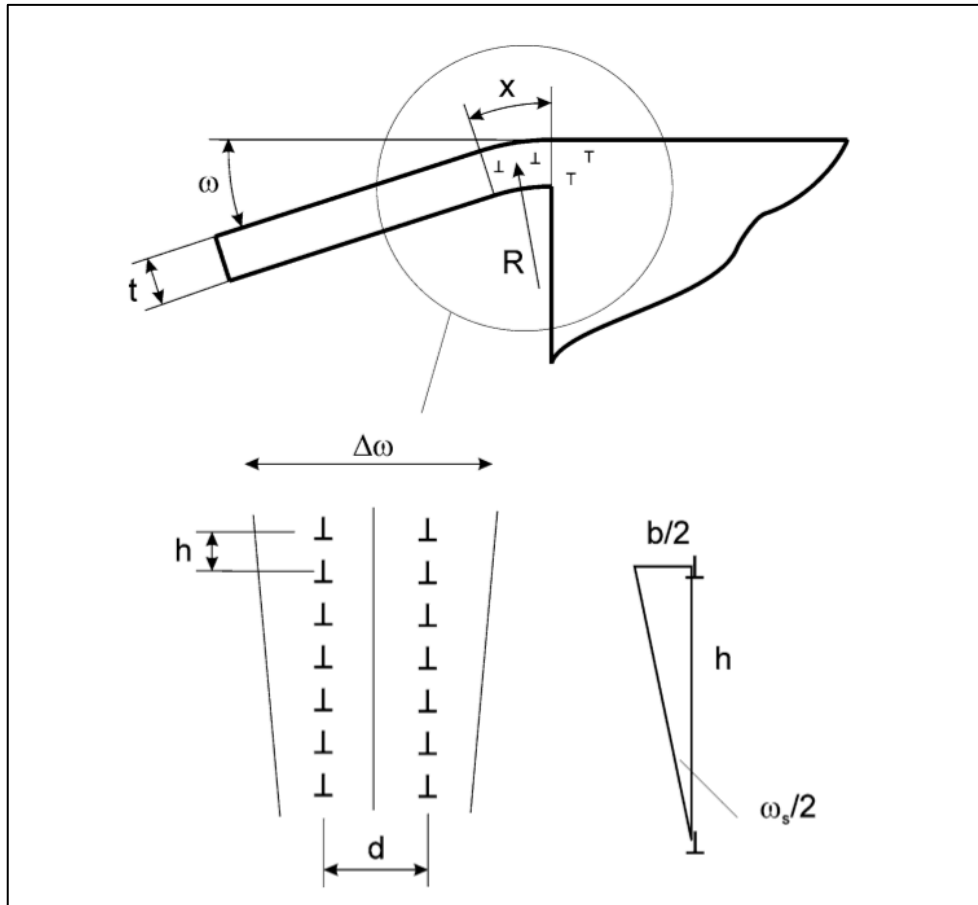
Figure 26: Geometric set-up of the bending beams and optimal dislocation arrangement of GNDs to accommodate the strain gradient [26].
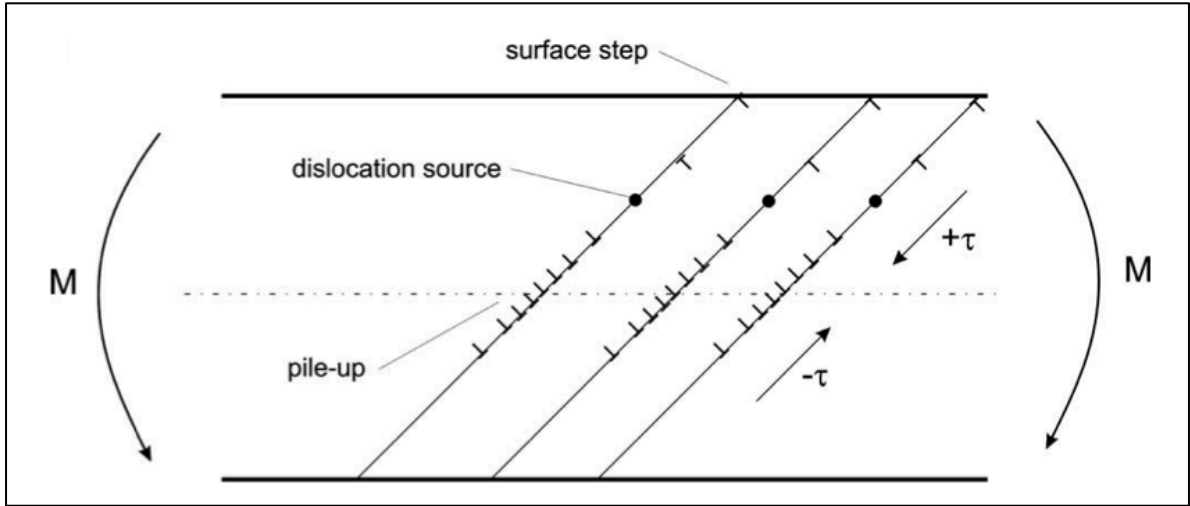
Figure 27: Example of the possible underlying dislocation mechanism for the deformation of these micro-beams [26].

The total number of GNDs is given by the applied strain gradient. If one assumes now that only one dislocation source is available, all GNDs have to be put on one slip plane, which results in a massive pile-up at the beam center and therefore in a very high pile-up stress. Increasing the number of available dislocation sources, the GNDs can be distributed over several slip planes and the pile-up stresses decrease. If there is a huge amount of available dislocation sources, the GNDs can be distributed more or less uniformly and this pile-up effect vanishes. In Figure 28 it is evident that for high dislocation source densities the contribution of the pile-up effect is small, and compared to the strain gradient contribution almost negligible. However, if the source density is reduced the pile-up effect becomes dominant and can explain the high flow stresses.
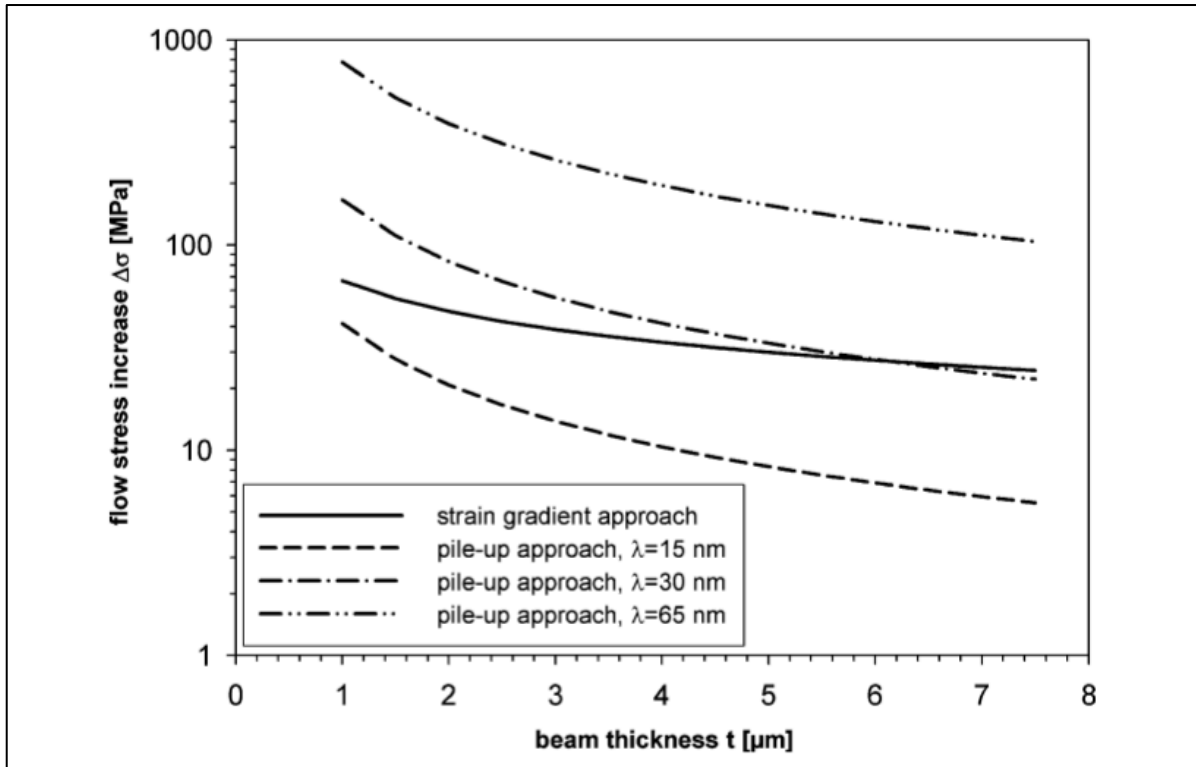
Figure 28: Comparison of the flow stress contributions of the strain gradient and pile-up approach for different mean dislocation source spacing, λ, depending on the beam thickness [26].

Demir et al. [46] presents a mean field breakdown theory where the local availability of dislocation sources, and not GNDs, dominates the mechanical size effect. Cantilevers with thickness between 0,7 and 5 μm were mechined and susequently bent with a nanoindenter. The calculated yield strength of the cantilevers showed a mechanical size effect; smaller is stronger. The GND density estimated form misorientation maps did, however, not explain the resulting size effect. The paper states that after pre-straining, when GNDs build up, they can contribute to the flow stress. However, by using very small critical strains to define the yield strength they explain that size dependency also occurs in samples that are not pre-strained. By this the paper concludes that the size effect is defined by the local availability of dislocation sources.

A reduction of the number of available dislocation sources in the small deformed volume, may hinder plastic deformation. If the number of available dislocation sources is limited, the activity of these has to be very high, and due to the back stress of the emitted dislocations the source can become inactive. In this case a higher applied stress is necessary to re-activate the source again, and the flow stress increases. If the defect density is small the probability of finding a sufficient number of dislocation sources decreases and the strength of the material increases; the material becomes dislocation starved. A dislocation starvation condition may also be due to high ratio of surface volume [26].

Pillar compression has been used to explain the smaller is stronger effect, see for example [47] [48]. Rogne and Thaulow have presented tow papers [49] [50] explaining the size effect and strengthening mechanisms of iron pillars. The papers discuss three different regimes of the mechanical behavior and its influence on the flow stress. The first regime consists of pillars from some few microns to tenths of microns in diameter. The stress-strain curve from pillar compression appears smooth and similar to bulk, but requires higher stresses to deform. This is explained by the existence of large dislocation segments influenced by the truncated volume. The limited volume is constraining the natural dislocation movement and interactions. Dislocation sources i.e. frank read sources are important for plastic deformation by the generation of dislocations, which causes plastic slip. If the distance between pinning points is in the same regime as the pillar diameter it is assumed that it cannot operate as in bulk. The second regime consists of pillars from some few hundreds nanometers to about 1 micron in diameter. In this regime the dislocation source is smaller than the diameter of the pillar. Since the diameter of the pillar is smaller than the average distance between dislocations it is likely that the pillars only contain small dislocation segments. The transduced dislocation segments operate in a stochastic way and need a higher stress to operate. Dislocation networks are not formed and movement of individual dislocations causes plasticity. It is likely that the dislocations will move towards the surface annihilates without multiplying on the way. The pillar reaches a dislocation-starved condition and nucleation of new dislocations becomes the limiting factor. The third regime consists of pillars less than some few hundred microns. The plastic flow is characterized by large elastic segments and an abrupt strain burst. The small volume makes it unlikely that dislocation segments from the initially annihilated dislocation structure is included in the pillars. For plasticity to occur dislocations are nucleated from small defects at the surface.

This chapter has presented different mechanical behavior that contributes to the size effect; strain gradient plasticity, dislocation pile-up at the center of the beam and limitation of available dislocation sources. A simple arithmetic addition of the contributions is not promising, because the contributions are not independent of each other. Dislocations of the different processes will influence each other and, therefore, a strict separation is not possible.

2.5 CTOD

The J-integral was proposed in 1968 by Rice to characterize the intensity of elastic– plastic crack-tip fields, and symbolizes the elastic–plastic fracture mechanics. The Crack tip opening displacement (CTOD) concept was proposed in 1963 by Wells to serve as an engineering fracture parameter, and can be equivalently used as J in practical applications [34]. In case of the ductile behavior the crack faces opens prior to fracture and creates a blunt crack tip. The opening of the crack can be used as an approach to measure the toughness for a material. There are two ways of defining the CTOD. One way is to distinguish the curving of the tip to define the distance (d), and measure CTOD at this defined distance, shown in Figure 29. The second way is to measure CTOD at the intersection between the lines from a 90 angle at the crack tip, shown in Figure 30.
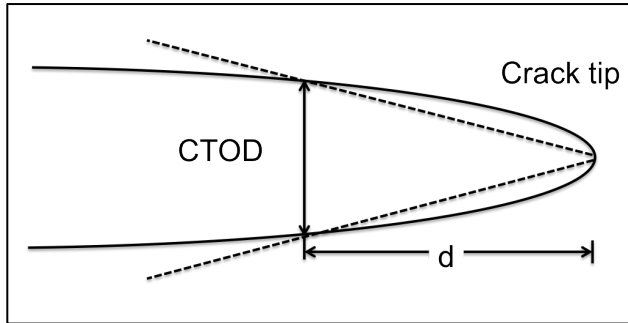
Figure 29: CTOD at a defined distance from crack tip
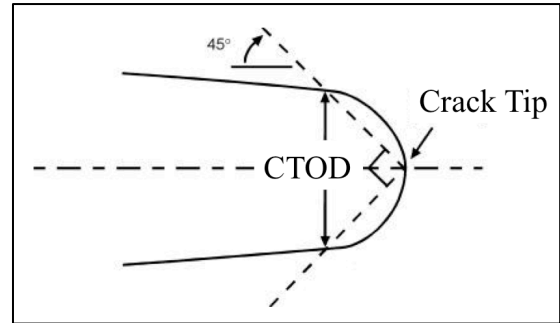
Figure 30: CTOD at interphase with 90 angle

2.5.1 Direct measurement

With a picoindnter that can be interfaced with a scanning electron microscope (SEM) it is possible to perform bending of micro-cantilevers while simultaneously image the process. In-situ experimentation techniques rely on video from the electron microscope to correlate to the mechanical data. By this it is possible to directly measure CTOD during loading. One drawback with this approach is the difficulty of accurate measuring. Measuring these very small differences in distance requires high resolution and good image contrast.

2.5.2 Hinge model

An easier way to measure the opening of the crack is by measuring the crack mouth opening displacement (CMOD). The plastic displacement at the crack mouth is related to the plastic CTOD through a triangles constitution. The model assumes a rigid body rotation around a plastic hinge point i.e. the apparent center of rotation in Figure 31. The method was developed by Hollstein and Blau and is referred to as the plastic hinge model [34] [51] .

$$CTOD_{pl} = \frac{r_p(h - a_0)CMOD_1}{r_p(h - a_0) + a_0} \tag{23}$$
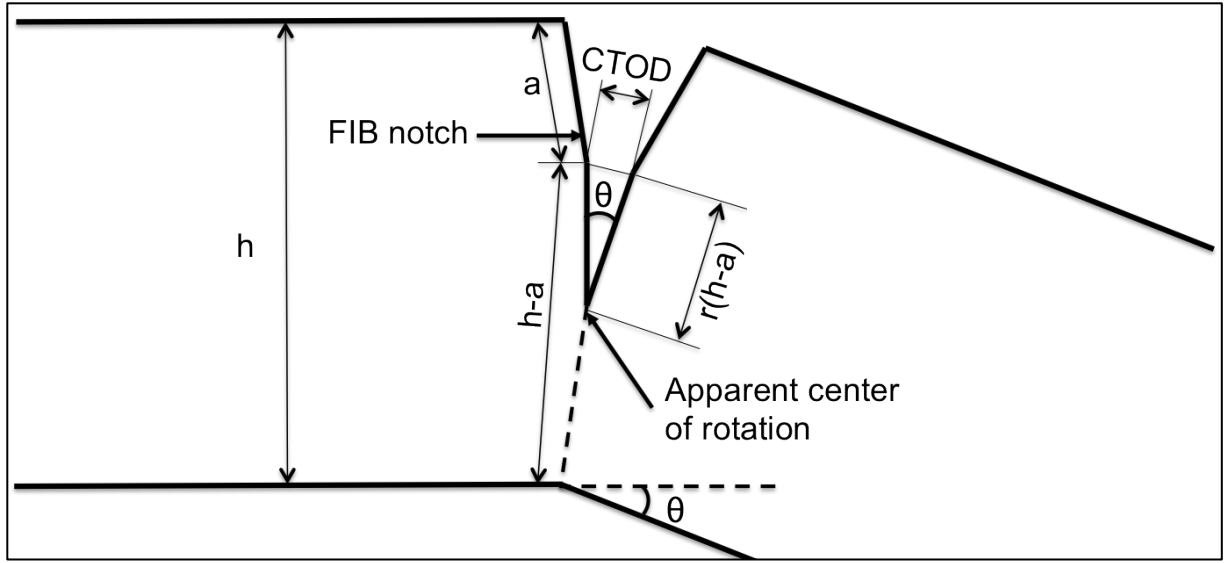
Figure 31: Plastic CTOD, adapted from [33].

Equation (23) is valid for a two point bending test of a beam with a square cross section. An estimate to relate this equation for cantilevers with a pentagon cross-section is to define a new height (h'), which will be slightly larger than the original height (h). The difference between one point bending and two-point bending is not believed to have a significant effect on the rotational center. Estimation of new height based on original cross section area:

$$h' = \frac{A_{crossection}}{w} \tag{24}$$

In order to order to apply the plastic hinge model to both plastic and elastic-plastic conditions the total CTOD can be calculated by the contributions determined from the plastic CMOD in terms of the hinge model, and the elastic component from the applied stress intensity factor

$$CTOD = CTOD_{el} + CTOD_{pl} = \frac{K^2(1-v^2)}{2E\sigma_y} + \frac{r_p(h'-a)CMOD_1}{r_p(h'-a)+a} \tag{25}$$

For the double gauge model the center of rotation is believed to be approximately 45% of the ligament ahead of the crack tip, which results in $r_p = 0.45$. The drawback with this method of measuring CTOD is the uncertainty of the exact location of the center of rotation. The literature reports that the r_p value is not a constant, but dependent on the a/h ratio and material properties [34]. This value may strongly affect the accuracy of the calculated CTOD, which will be further discussed in the following chapter.

2.5.3 Double gauge model

CTOD δ5 has been reported in the literature as a technique for measuring Crack Tip Opening Displacement. The concept of the CTOD δ5 is to determine the crack tip opening in a direct way by measuring the relative displacement of tow gauge points. CTOD is measured locally next to the crack tip and is independently of the global behavior. This direct approach does not need any prior analysis on structural components, and allows any specimen geometry. CTOD$_{δ5}$ measures the crack opening locally next to the crack tip and is independently of the global behavior. The method however assumes a triangular shaped crack [52]. By measuring CMOD at two different points, at a certain distance from the crack tip, CTOD can be calculated from trigonometric functions. During loading the crack edges can be difficult to

distinguish. In order to differentiate exact measuring points two marks can be made on the top of the cantilever with a known distance from the crack edge (l_1). By this the measuring points are well define. Additionally two marks on the side edge of the cantilever, with a known distance form the crack (l_2), should be machined. When the cantilever is loaded these marks are used as reference points. By measuring the length L during loading and subtracting the known distance l, CMOD can be calculated. When $CMOD_1$ and $CMOD_2$ have been determined, these values can be used to determined crack length (a) and CTOD.
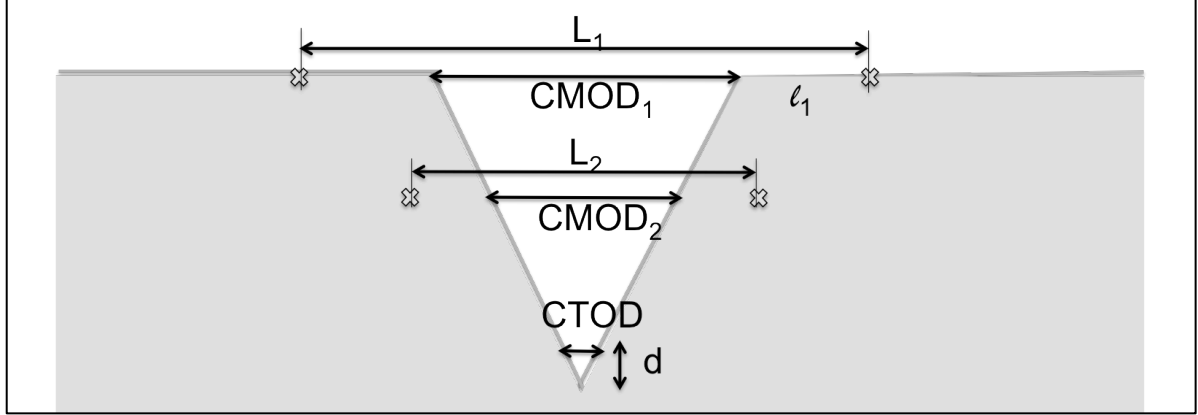
Figure 32:
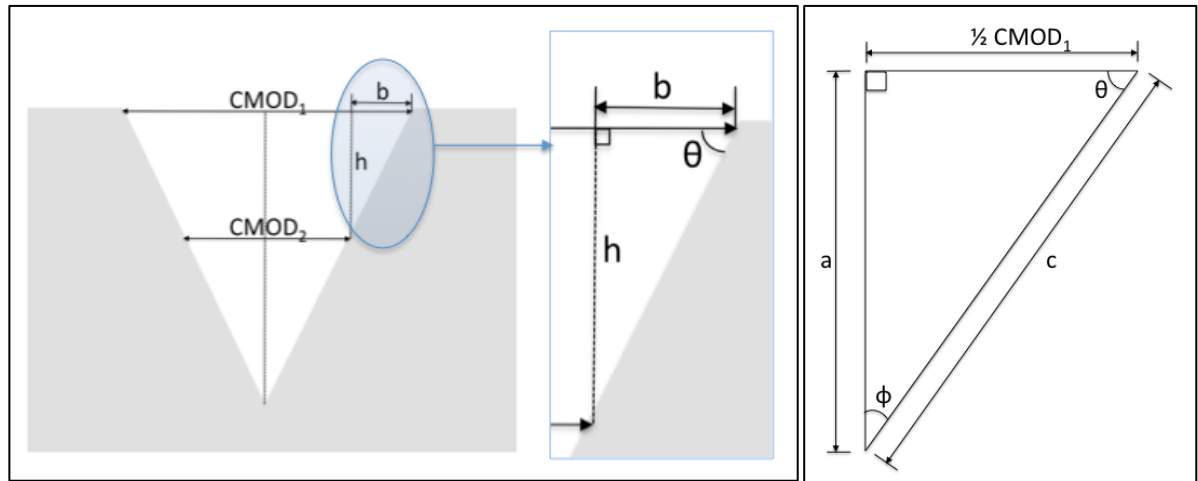
Figure 33:

$$CMOD_1 = L_1(before\ loading) - L_1(after\ loading)$$
$$CMOD_2 = L_2(before\ loading) - L_2(after\ loading) \quad\quad (26)$$

$$b = \frac{CMOD_1}{2} - \frac{CMOD_2}{2} \quad\quad (27)$$

$$r_p = \tan\theta \cdot \frac{1}{2}CMOD_1 \quad where \quad \tan\theta = \frac{b}{h} \quad\quad (28)$$

$$CTOD = CMOD_1\frac{d}{a} \quad\quad (29)$$

Enrique M. Castrodeza et al. [53] has presented a paper assessing the available methodologies for critical CTOD measurement . The papers experimentally evaluate the difference between the hinge model, hereafter called CTOD, and the double gauge model hereafter called $CTOD_{\delta 5}$. The material used in these studies was Fiber Metal Laminates. In all cases the critical toughness values obtained by the two methodologies were different. These differences between critical values led to a more detailed analyze of the evolution of traditional CTOD against $CTOD_{\delta 5}$ up to the first instability. It can be seen from Figure 34 that traditional CTOD values were smaller than $CTOD_{\delta 5}$, for low loads. Reduced differences between both parameters at the beginning of the tests can be observed; for large displacements, however, there was an overestimation of traditional CTOD. It was then decided to analyze the r_p evolution. Figure 35 shows CTOD calculated with different r_p values vs $CTOD_{\delta 5}$, indicating the substantial effect the uncertainty of the exact position of the rotational center has. Using $CTOD_{\delta 5}$, the r_p evolution was analyzed and plotted as a function of CMOD. A great variation of r_p from near zero values up to approximately 0.4 at critical point is seen in the resulting graph in Figure 36, indicating an irregular behavior. These results point out that the $CTOD_{\delta 5}$ method proved most accurate.
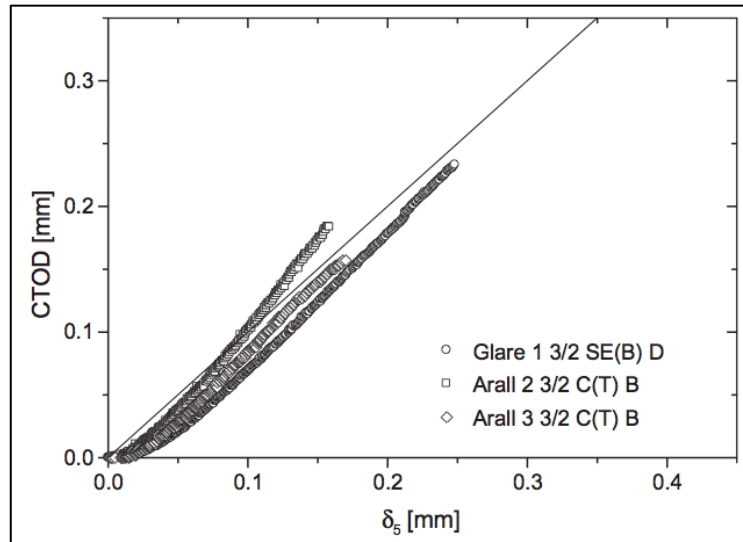
Figure 34: CTOD vs $CTOD_{\delta 5,}$ adapted from [53]
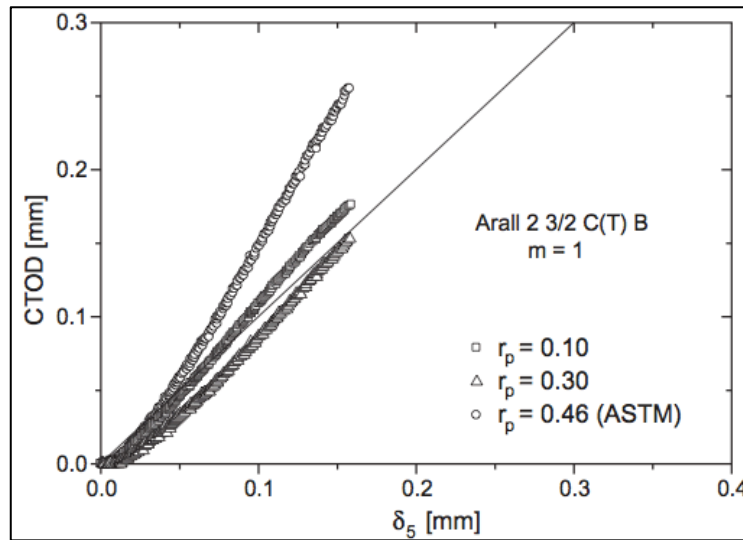
Figure 35: CTOD calculated with different r_p vs $CTOD_{\delta 5}$ [53]
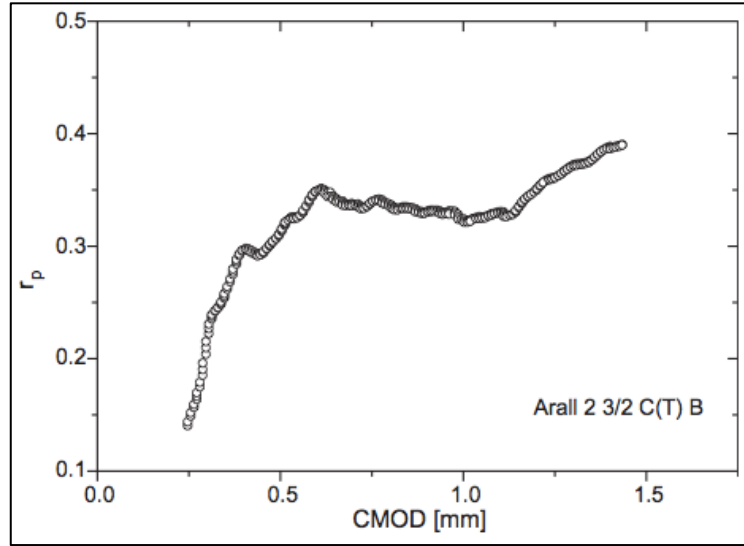
Figure 36: Analyses of the r_p evolution vs CMOD [53]

2.5.4 Crack tip opening angle

Another way of measuring the opening of a crack is the Crack Tip Opening Angle (CTOA). CTOA is defined as the average angle of the two crack surfaces measured at a point behind the crack tip, and may be used as a material property for an efficient characterization of large amounts of crack extensions. CTOD δ_5 measurement technique can be used to determine CTOA.

$$CTOA(\phi) = \tan^{-1}\left(\frac{\frac{1}{2}CMOD_1}{a}\right)$$

(30)
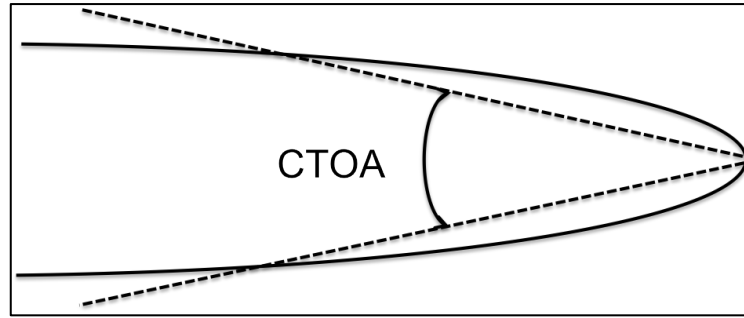
Figure 37: Crack tip opening angle (CTOA)

However, the distance at which CMOD is measured can have a significant effect on the resulting CTOA. E. N. Johnston [54] attempted to analyze the effect of the location of the measuring points for CMOD on the resulting values for CTOA. In the early stages of crack propagation the crack flanks experience several phases in general shape/separation. The general failure process for a metallic material that undergoes large amounts of plastic deformation near a pre-existing sharp crack in low constraint conditions has been shown to consist of three distinct phases: (1) crack blunting (2) stable crack extension, (3) unstable crack extension after maximum load carrying capacity is reached. Due to these phases differences in measurement methods may produce different values of CTOA. In general the "surface crack tip" is the visible point on the surface where the crack flanks come together. The "reference range" is a small range, which is not far behind the surface crack tip while the "baseline range" extends longer and is further behind the surface crack tip.
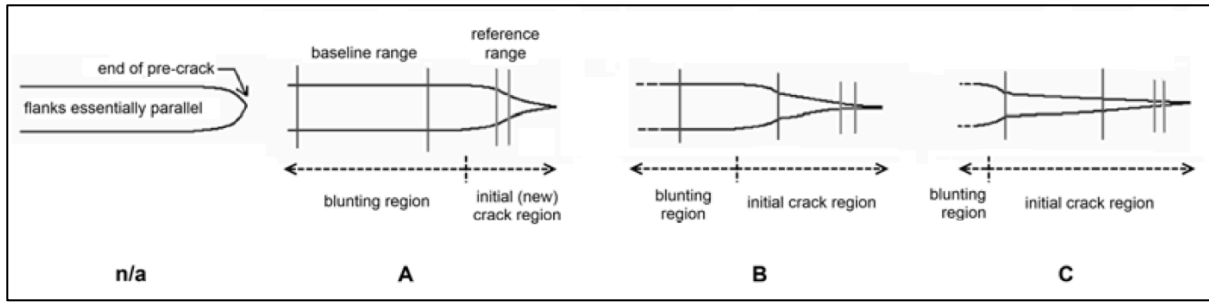
Figure 38: Illustration of the defined phases of crack propagation [54]
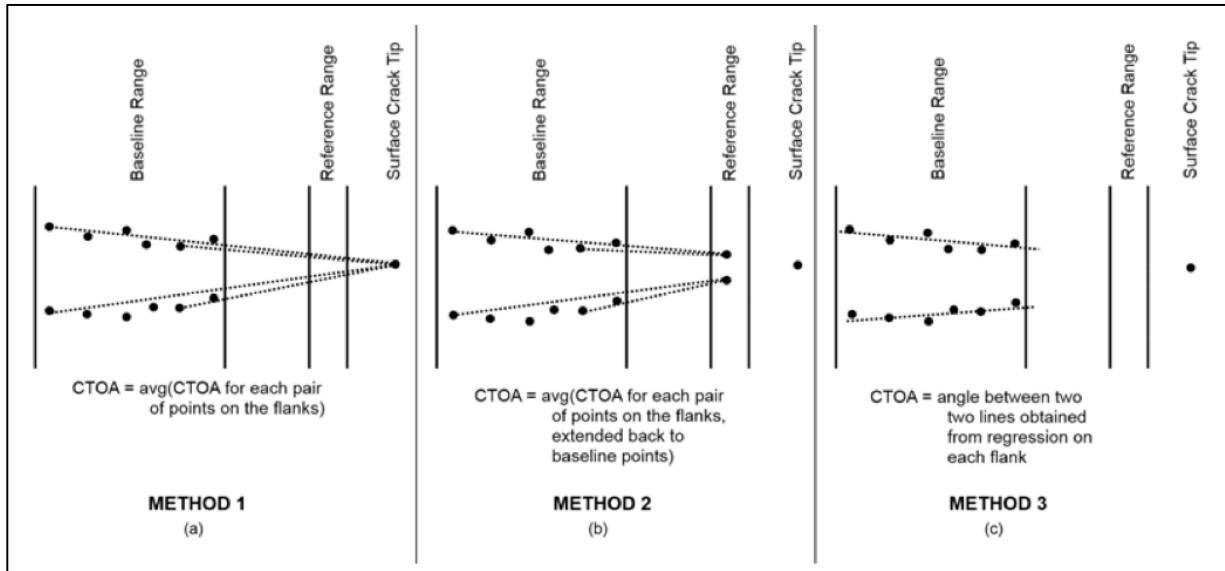
Figure 39: Illustration of different measuring methods [54]

Generally speaking, the CTOA values obtained from Method 1 start high and then decrease to a nearly constant value. Method 1 does not include the reference range, so Phase A does not affect the CTOA values. Due to the nature of Method 1, as the baseline range enters the initial crack region at Phase B, the CTOA values begin to decrease and continue decreasing through Phase C. This is due to the crack flanks being closer together in the initial crack region.

Rather than to use the crack tip, method 2 uses a pair of points on the crack flanks within the reference range are used in the measurement and the angle is calculated based on distances between the flanks. An important note on this method is that the vertex of the angle defined by the extended flanks is not forced to meet the crack tip. If the vertex of the measurement angle is located, it may converge at a point behind or beyond the actual crack tip. Method 2 begins at a high value as Method 1 did, but begins lower than the initial value for Method 1. When Phase A occurs, the CTOA values for Method 2 increase sharply because this is where the difference between the displacement in the baseline range and the reference range increases sharply. When Phase B occurs, the measured CTOA values begin to decrease and continue decreasing through Phase C. The decrease at Phase B occurs because the baseline range begins to enter the initial crack region where the flanks are closer together. Since the vertex of the extended lines is not forced to lie at the surface crack tip and may actually extend beyond it, a slightly lower constant CTOA value than Method 1 may be obtained entering into Phase C.

Method 3 defines a sets of points in the baseline range only and uses linear regression to fit a line to these points for each flank, this method also does not force the defined lines to

intersect the surface crack tip. If the defined lines are extended to their vertex, it may lie behind or beyond the actual crack tip. Method 3 also starts at a high CTOA value, but begins at a value lower than the initial value for both Methods 1 and 2. Measurements in the reference range are also not included in Method 3, so Phase A does not have an effect on the CTOA values of this method. At Phase B, a sharp increase in CTOA values is observed. This is because the tip of the regression lines closest to the crack tip are drawn closer together as the baseline range enters the close flanks in the initial crack region. As the baseline range exits the blunting region completely in Phase C, the ends of the regression lines furthest from the crack tip are also drawn together. This makes the lines more parallel and causes a decrease in the measured CTOA values.
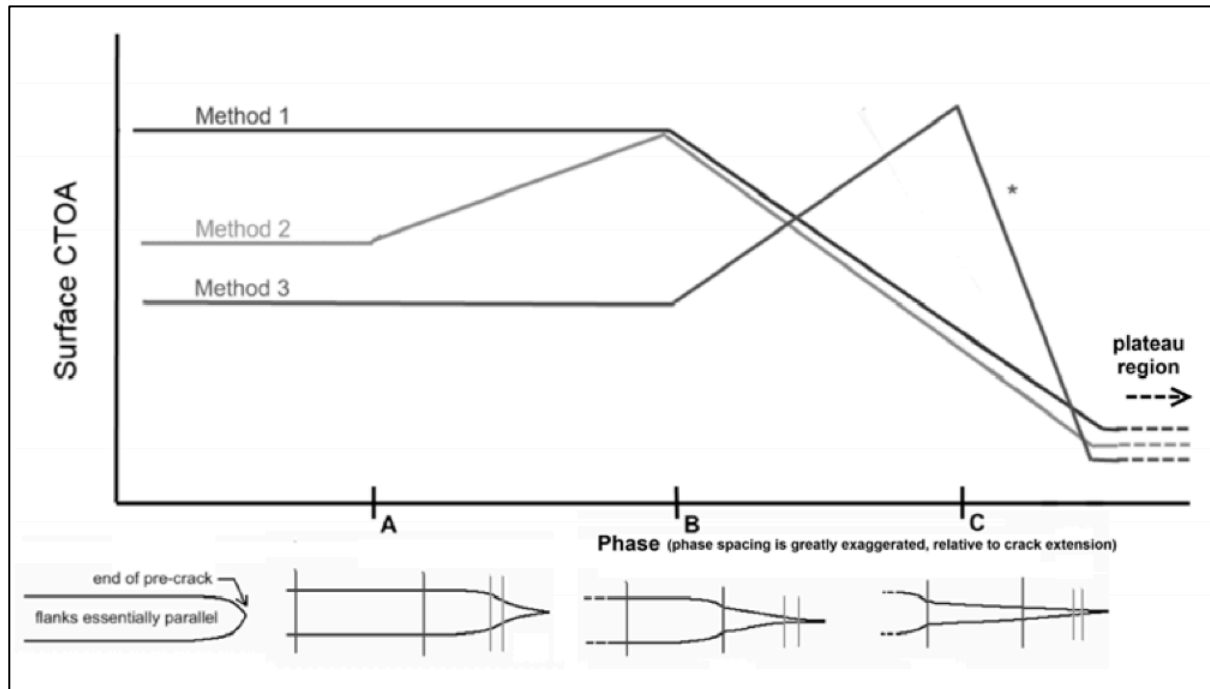
Figure 40: Idealized trends for each measuring method in the initial non-constant CTOA region [54]

As explained by E. N. Johnston the distance from the crack tip to the measuring point have a distinct effect on the measured CTOA in the early stages of crack propagation. However, when dealing with very ductile materials a blunt crack tip may not propagate, the crack flanks may merely move apart. In this case the distance from the crack tip to the measuring point will have an even bigger effect on the resulting CTOA. The measured CTOA in both cases will be increasingly accurate with decreasing distance between crack tip and measuring point.

3 Material and experimental procedure

3.1 Material

The sample used in this study was a polycrystalline single-phase bcc α-iron provided by Alfa Aesar GmbH & Co KG-A Johnson Matthey Company. The purity of the iron is very high (99,995%) making the crystallographic orientation homogeneous within each grain. The sample is heat treated in a high vacuum furnace in order to obtain enlarged grains. The sample had a circular surface area of $1cm^2$ and a height of 5mm.

3.2 Sample preparation

For EBSD scans the sample surface must be sufficiently smooth. The metallographic preparation of the samples requires several steps. In order to obtain the desired finish, different grinding discs were used, finer for each step (P800 / 25,7μm, P1200 / 15,3μm, P2400 / 6,5μm). Between every step the sample was rotated 90° in order to make sure that the lines from the previous step were fully removed. Mechanical grinding and polishing, result in significant deformation to the surface layer. Therefore, it is necessary to remove the damaged layer by electropolishing in order to be able to analyze the crystallographic directions using EBSD. The sample was elctropolished using 95% Methanol (CH3OH) and 5% Sulfuric acid (H2SO4). The optimal conditions for the electropolishing were obtained by trial and error, with different variables of voltage and time, constantly checking the surface in an optical microscope. The optimal conditions were ultimately defined as a cell voltage of 15V, and a time of 60s.

The sample was marked using a macro indenter. A 6x6mm area was indented, with 2mm between each indent. Point A_1 was given coordinates (0,0). A double indented (A_2) was made in the first corner in order to know the exact coordinates when the sample is rotated, as shown in Figure 41.
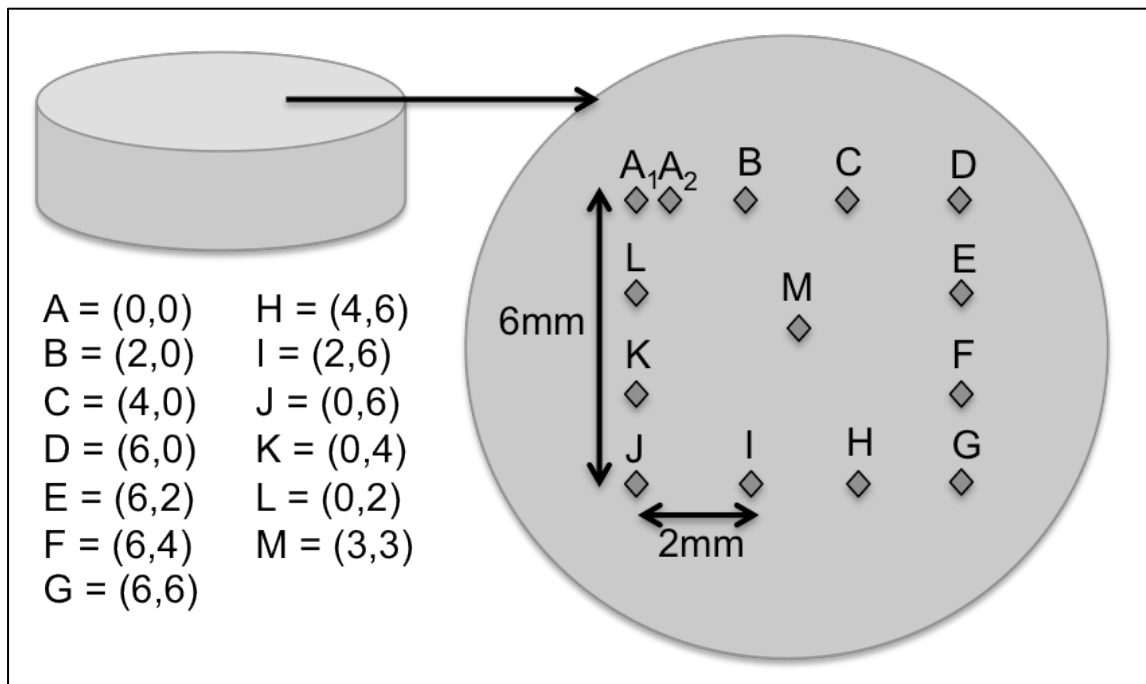
Figure 41: Marking of sample.

3.3 Characterization of crystallographic orientation

In order to know the crystal orientation of the surface grains, an EBSD analysis were conducted. With the EBSD analysis results, grains with suitable orientation can be located and further utilized to fabricate cantilevers. The EBSD scans were conducted on a Hitachi SU-6600 FESEM. At a woking distance of 24mm, required for EBSD analysis, this SEM can scan an are of approximately 2,5x2,5mm maximum. In order to map a large area of the sample surface, 9 scans (3x3) were conducted, with an area of overlapping shown in Figure 42.
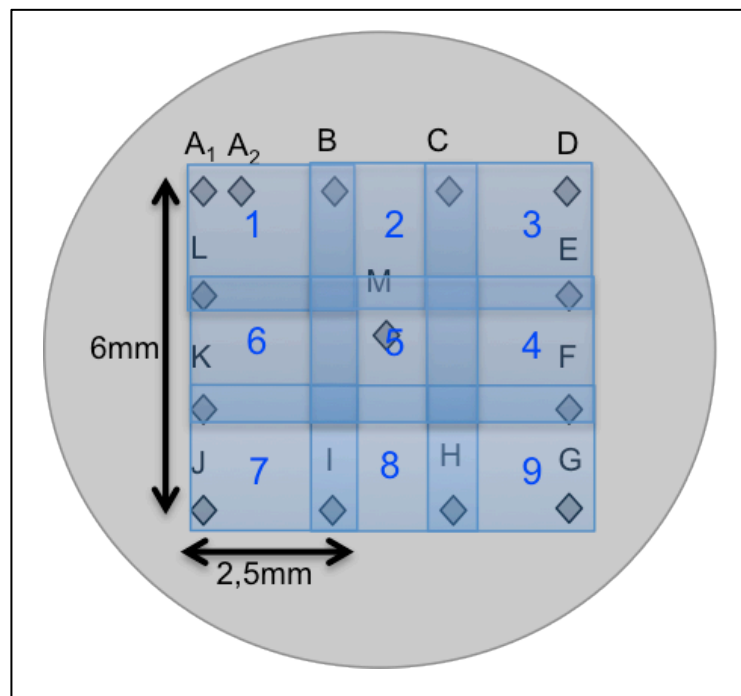
Figure 42: EBSD scan area

The area of interest was scanned using the software Nordif. The system requires 5 calibration points and one acquisition point. To ensure reliable results these points should have clear diffraction patterns. To ensure clear diffraction patterns overlaying patterns must be avoided, optimal parameters must be defined and the background light needs to be removed, so that the light bands in the patterns are well defined. The parameters for the EBSD scans are listed in Table 1.

Table 1: EBSD parameters

Parameter:	Value:	Parameter:	Acquisition settings:	Calibration settings:
Acceleration voltage:	20,0kV	Frame rate:	800fps	100fps
Working distance:	26,6mm	Resolution:	96x96px	240x240px
Tilt:	70°	Exposure time:	1200fps	9950fps
Step size:	5μm	Gain:	7	5

To indicate the stored diffraction pattern TSL OIM data collection was used. The patterns are extracted and converted to bitmap files, giving a color-coded map of the surface grains. Each color represents a different crystal direction, as shown in Figure 43.
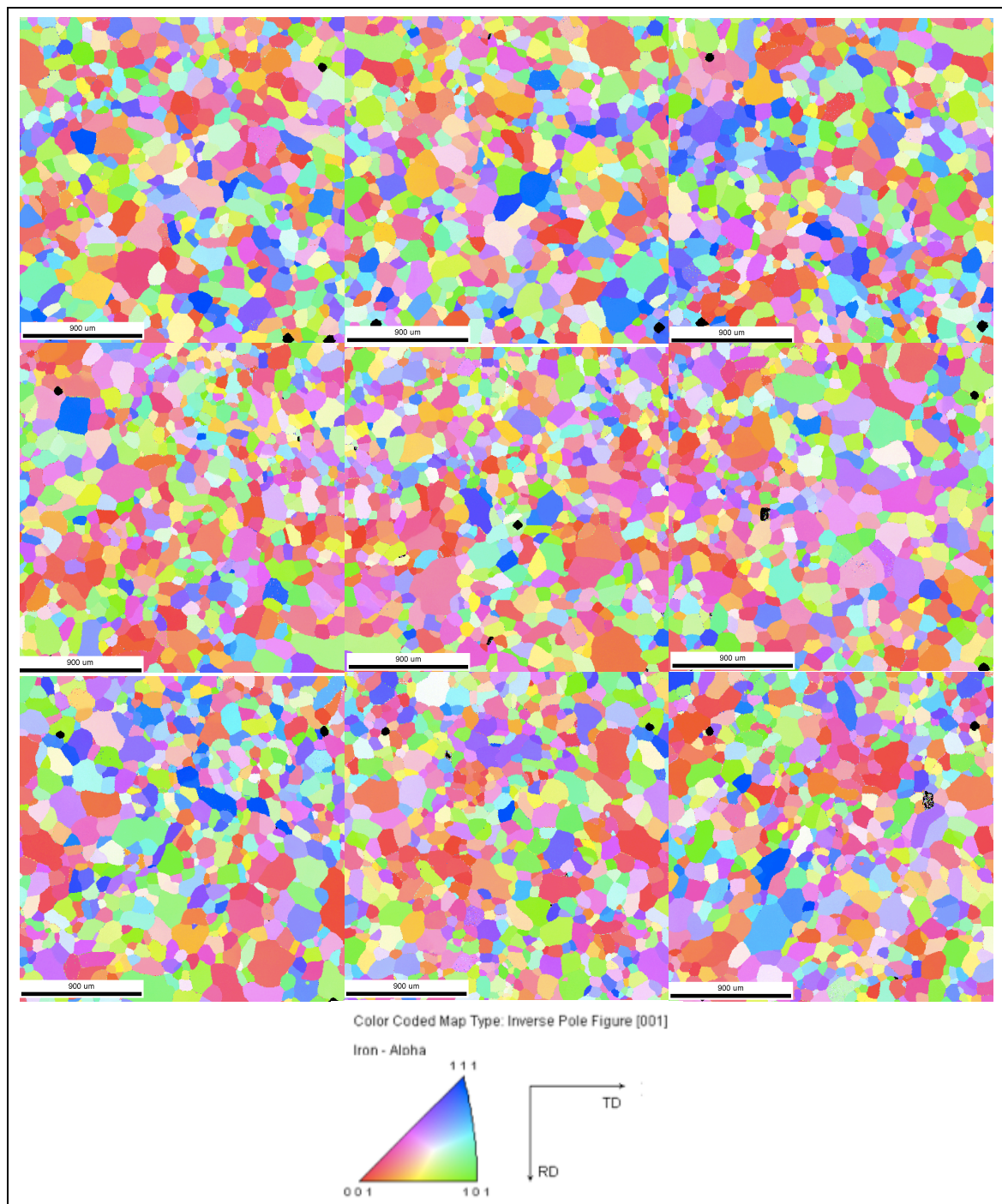
Figure 43: OIM color coded map

An OIM analysis was performed, highlighting the grains of interest. Figure 44 shows the resulting color-coded crystal direction map. The blue grains have a <100> direction parallel with the RD direction. The red grains have a <100> direction parallel with the TD direction. The grains chosen for machining of cantilevers are marked with yellow circles.
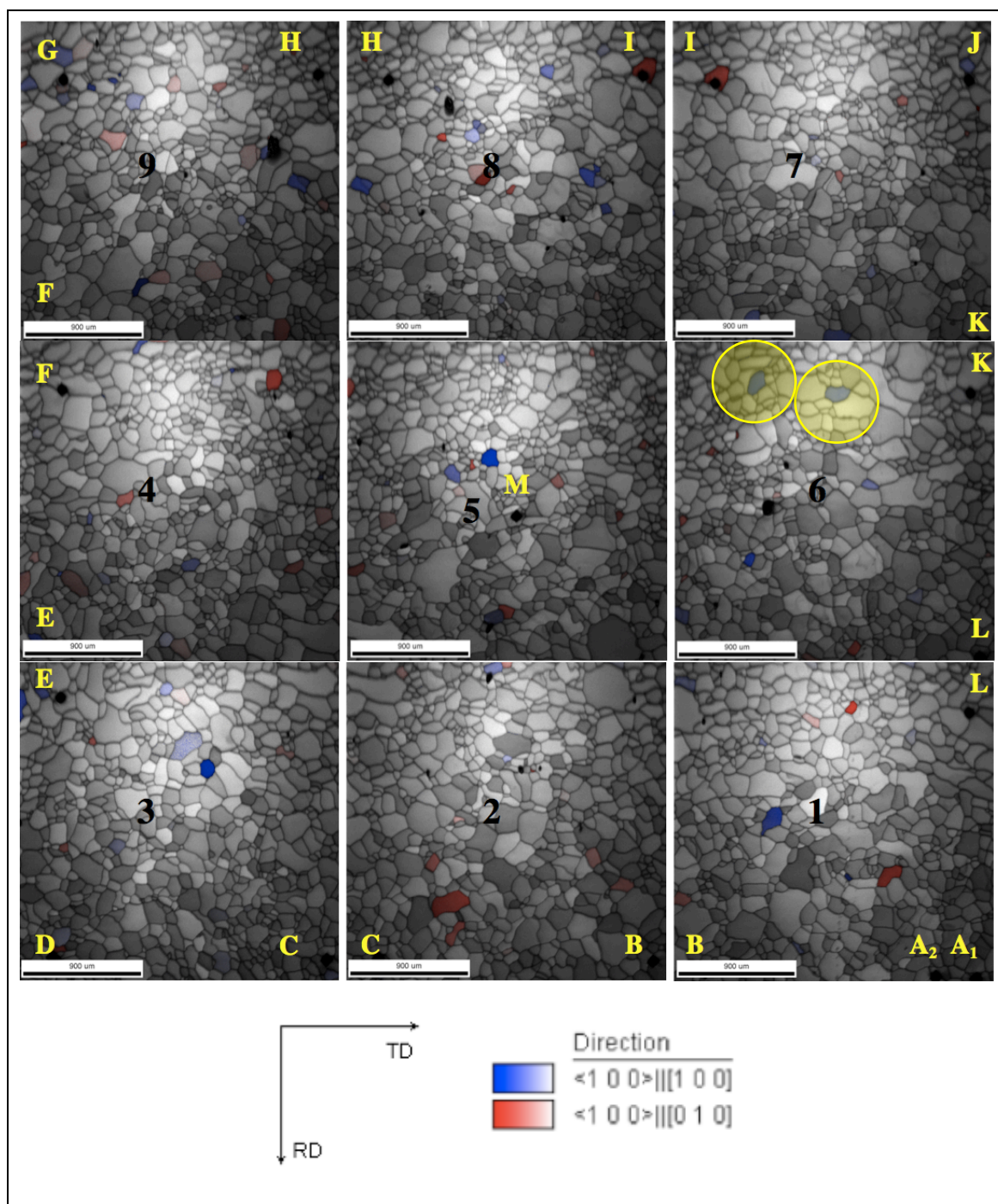
Figure 44: OIM analysis; highlighting grains of interest

3.4 Machining of cantilevers

The machining of the cantilevers was conducted on a FEI Helios DualBeam FIB at NTNU Nanolab. The grains of intereset were located, and the sample was positioned and rotated in order to machine the cantilevers correctly according to the EBSD analysis. When the right location was determined the milling process was initiated. The milling procedure consists of a series of different steps, with consequently individual milling parameters.
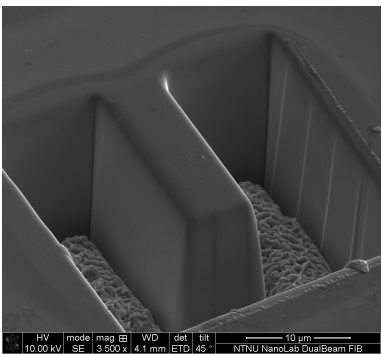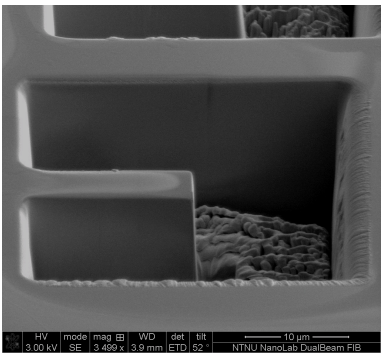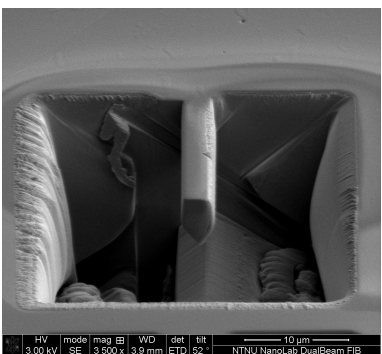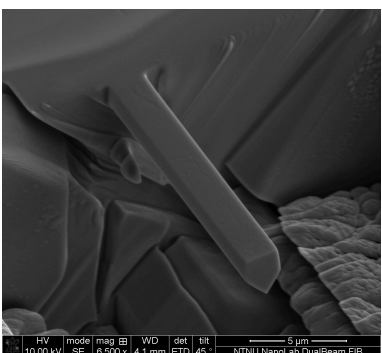
Table 2 lists the different steps in the milling process, with corresponding parameters. Relatively large beam current was used for the initial material removal. A substantial amount of material has to be removed. It is essential to have enough space around the cantilevers, i.e. a large crater, for material re-deposition in the following steps. The area beneath the cantilever also has to be sufficiently deep in order to have enough space for an unknown amount of cantilever deflection during loading. Subsequently lower beam current was used for the final surface milling in order to achieve sharp edges and smooth sides.
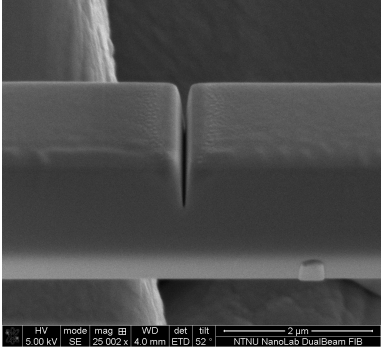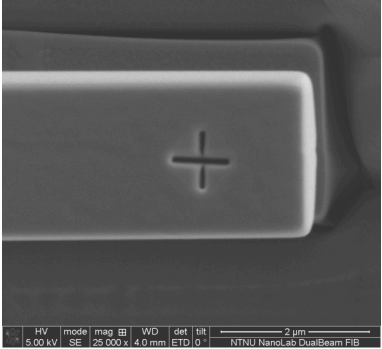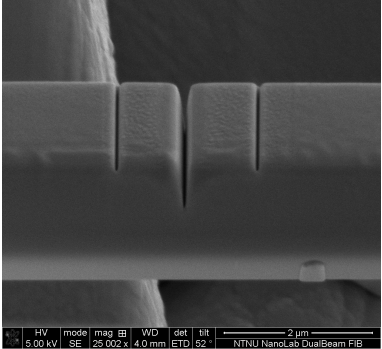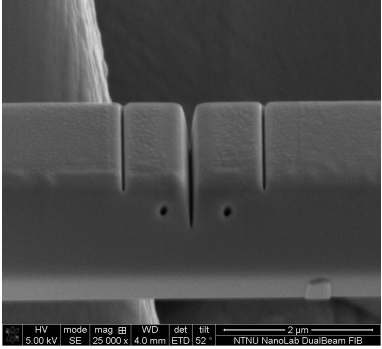
When trying to mill the notch, with only a line pattern, the notch did not reach the desired depth. This is due to re-deposition of sputtered material; when the line pattern reaches a certain depth, the sputtered material is not ejected but remains within the notch, resulting in a competition between re-deposition and sputtering. By using a combination of a rectangular and line pattern the desired depth is achievable. However, when milling the initial rectangular pattern it is almost impossible to avoid removal of material on the side edges of the cantilever. The removal of material on the side edges makes it extremely difficult to determine the crack length. Another method was thereby tested. With a series of line patterns a more distinguished notch was obtained. By using a fairly small z value i.e. a small depth value it was possible to place a series of line patterns after one another. In order to achieve the desired depth of the notch, the location of the line patterns were slightly change. One pattern were placed slightly to the left from the first pattern and so on, until a final line pattern were centered in the notch in order to create a sharp crack tip.

On the free edge of the cantilever a cross were machined in order to make it easier to precisely place the indenter during loading. During loading the image quality is limited, which will be further discussed chapter 3.7. In order to make it easier to distinguish the opening of the crack to line pattern were placed at a known distance from the notch. By this it is possible to measure the distance from the two lines and calculate CTOM. On the side edges of the cantilever two marks were made so that CTOD may be determined by trigonometrically functions, as discussed in chapter 2.5.3.

Table 2 shows, as mentioned, the main steps of the milling process. However, it was necessary to do cleanup milling in between the different steps, due to re-deposition. Material ejected from the sample during sputtering emerges with a variety of trajectories, and geometrical effects from structural features will affect the location of the re-deposited material.

Table 2: Milling steps with corresponding parameters.

	STEP 1: Milling of crater **Position:** 90° with respect to the ion beam **Pattern:** Polygon **Size:** 30x30 μm, beam 7x18 μm **Depth:** z = 10μm **Accelerating voltage:** 30,0kv **Beam current:** 20,0nA
	STEP 2: Reducing the length and width **Position:** 90° with respect to the ion beam **Pattern:** Cross-section **Size:** Depending on previous step, beam 4x16 μm **Depth:** z = 6μm **Accelerating voltage:** 30,0kv **Beam current:** 2,7nA
	STEP 3: Milling angled bottom edges **Position:** 45° with respect to the ion beam. One side was milled, then a 180° rotation with respect to the specimen was made in order to access the other side. **Pattern:** Cross-section **Size:** 1st side 20x6 μm, 2nd side 20x3 μm, approximately. **Depth:** z = 10μm **Accelerating voltage:** 30,0kv **Beam current:** 6,5nA
	STEP 4: Final milling of all side edges **Position:** 90° with respect to the ion beam **Pattern:** Cleaning cross-section **Size:** Dependent on side conditions and geometry **Depth:** z = 1μm **Accelerating voltage:** 30,0kv **Beam current:** 0,90nA

	STEP 5: Milling of the notch **Position:** 90° with respect to the ion beam **Pattern:** Several lines **Size:** Width of beam **Depth:** z = 0,5μm **Accelerating voltage:** 30,0kv **Beam current:** 1,5pA
	STEP 6: Milling of mark for loading location **Position:** 90° with respect to the ion beam **Pattern:** Two lines **Size:** - **Depth:** z = 0,2μm **Accelerating voltage:** 30,0kv **Beam current:** 1,5pA
	STEP 7: Milling of marks on top of cantilever **Position:** 90° with respect to the ion beam **Pattern:** Line **Size:** Slightly shorter than the width of the beam **Depth:** z = 0,2μm **Accelerating voltage:** 30,0kv **Beam current:** 1,5pA
	STEP 8: Milling of marks on side edge of cantilever **Position:** 90° with respect to the ion beam **Pattern:** Circle **Size:** 70nm in diameter **Depth:** z = 0,2μm **Accelerating voltage:** 30,0kv **Beam current:** 1,5pA

3.5 Low temperature in-situ test set-up

Extensive works has been put into designing and constructing a cooling system in order to perform in-situ experiment with a picoindenter interfaced with a SEM, at low temperatures. The developed cooling system consists of a liquid nitrogen tank mounted on an SEM port, which is connected to the sample through a coldfinger. It is essential that the coldfinger have good thermal conductivity between all components in order to achieve temperatures relatable to arctic environments. Another SEM port is used for temperature measurements. The port has a feedthrough so that the temperature measuring instrument is connected to the sample. An additional SEM port is reserved for the electrical connection from the picoindenter. The above described set-up is schematically shown in Figure 45. The available space in the SEM chamber is restricted, and consists of fragile and expensive parts. When designing the set-up it was extremely important to consider the limited space, and to ensure safe handling of both the picoindenter and the SEM.
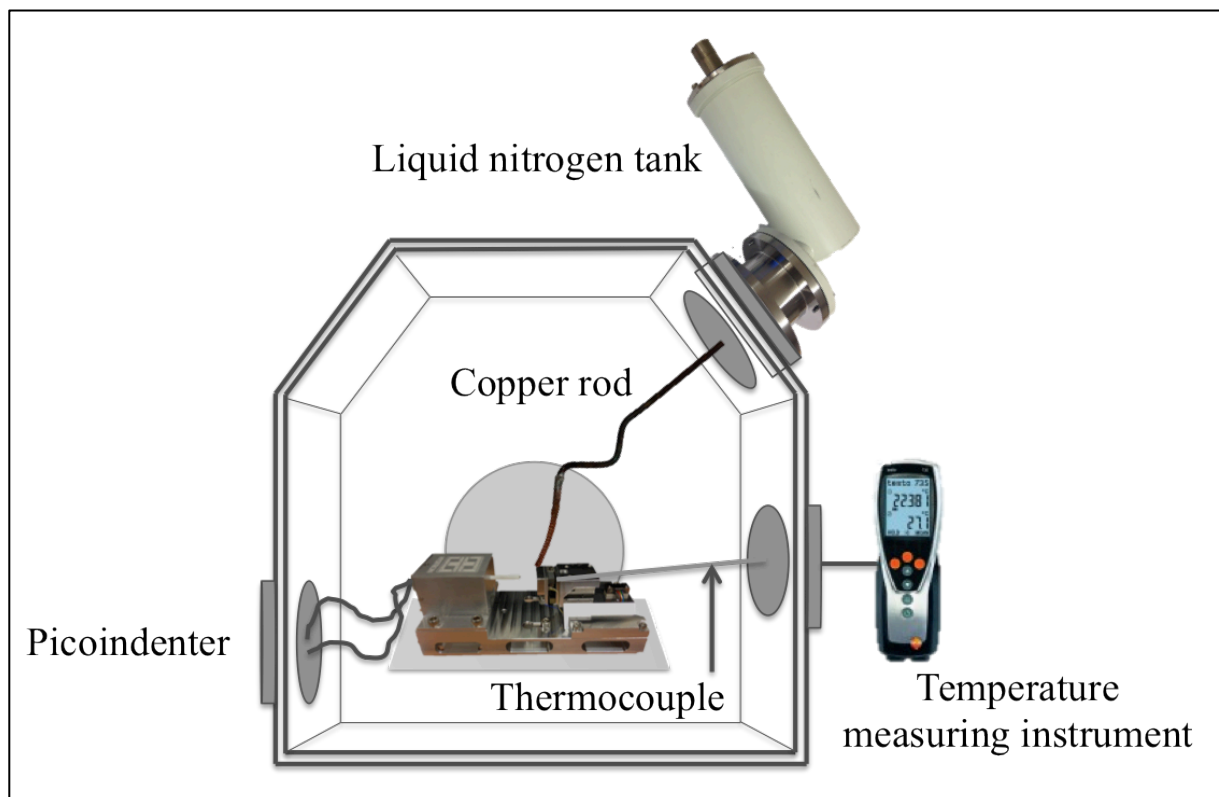
Figure 45: Schematic illustration of the cooling system.

The cooling source i.e the liquid nitrogen container was provided by another institute at NTNU. However the existing flange to connect the liquid nitrogen tank to the SEM port was not compatible with the SEM at our institute. Therefor a new flange with the right dimensions had to be machine. Measurements were made and the flange was machined at the Fine Mechanical Workshop at NTNU. Figure 46 shows the liquid nitrogen tank with the new flange. The liquid nitrogen tank is connected to a coldfinger. The coldfinger consist of a solid copper rod, a flexible copper stocking, a copper plate, and a brass stub. The solid copper rod had to be machined so that it would fit in the the SEM chamber. The dimensions and angles of this rod had to be precisely measured due to limited space. It was essential that the SEM stage could be safely operated when the copper rod was installed. A flexible wire was used in order to be able to bend it into the right dimension and angle. This wire was then used as a template to machine the final solid copper rod, showed in Figure 50, at the Mechanical

workshop at NTNU. The solid copper rod is screwed in the liquid nitrogen tank. The liquid nitrogen is not in direct contact with the rod, but there is a mechanical contact between the nitrogen container and the copper rod, cooling the rod down. Due to limited space in the chamber it is not possible to install the rod after the tank is mounted on the SEM port. Hence, there had to be a detachable connection between the rod and the rest of the coldfinger. A mechanical connection consisting of a brass clamp, showed in Figure 47, turned out to be a practical solution. The brass clamp contains two screws to squeeze the parts together in order to achieve a tight mechanical connection with good thermal conductivity.

During the experimental testing, small movements of the SEM stage and the picoindenter stage are necessary in order to locate the sample area of interest. Therefor the component connecting the solid copper rod to the sample had to be flexible. Additionally, this flexible connection had to be sufficiently massive in order to obtain good thermal conductivity. The solution was a copper stocking, consisting of several entwined copper threads showed in Figure 49. Initially, the intention was to solder the copper stocking directly to a small copper plate. In order to achieve low temperatures relatable to arctic environment the soldering had to be performed with a metal with good thermal conductivity. The chosen metal was silver, however silver soldering the copper stocking was difficult. Since the copper stocking consists of a large number of very thin copper threads witch burned easily due to the large surface area. This problem was solved using a brass ferrule between the copper stocking and the copper plate. The end of the copper stocking was twinned together and placed inside the ferrule before it was silver soldered. The other end of the ferrule was silver soldered to the copper plate.

A whole was drilled in the copper plate in order to mount a sample stub to it, by this a fairly large contact area is obtain, hence a better thermal conductivity through the system. Standard sample stubs are made out of Aluminum. Aluminum is however not possible to silver solder due the low melting temperature. A new brass sample stub was therefore machined and silver soldered to the copper plate, as showed in Figure 48. The brass sample stub was machined with a long shaft. When it is placed in the picoindenter stage this will ensure a gap of air between the parts resulting in a small contact area between the sample stub and the picoindenter stage, as shown in Figure 51. When the chamber is pumped the vacuum result in minimal cold loss to the chamber environment. A schematic illustration of the coldfinger is showed in Figure 53. The sample has to be mounted on the sample stub. This connection also had to have good thermal conductivity; hence it was not possible to use carbon tape. Fast drying Silver paint (59% silver solids) was tried, but excluded due to poor adhesion. The connection between the sample and the sample stub experiences some force when coldfinger set-up is mounted. The silver paint was replaced by Silver paste (72% silver solids). The Silver paste has a higher content of solid silver; hence a better thermal conductivity, and the adhesion proved sufficient.

Another important part of the set-up procedure is the mounting of the sample relative to the picoindenter probe. After attaching the sample to the stage, the indenter tip must be approached extremely close to the sample surface (approximately 1mm), as shown in Figure 52. This is a sensitive approach and need to be conducted with care and accuracy; hence this must be done before the picoindenter is mounted on the SEM stage. This was another reason why there had to be a detachable connection between the copper stocking and the solid copper rod.

Figure 46: Liquid nitrogen tank with connecting flange.
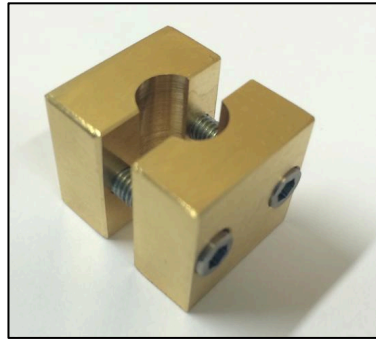
Figure 47: Brass clamp
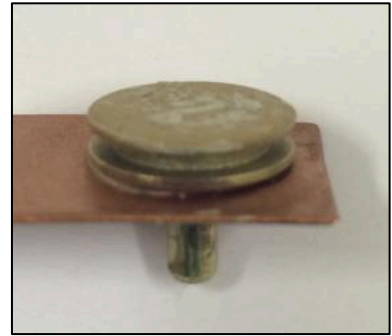
Figure 48: Brass stub

Figure 49: Flexible copper stocking

Figure 50: Solid copper rod

Figure 51: Gap of sir between picoindenter stage and sample stub
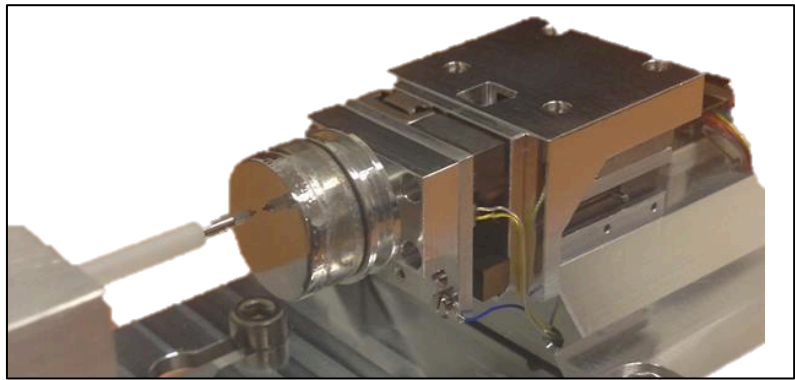
Figure 52: Tip to sample surface distance

Table3:

Material	Thermal conductivity	Melting temperature
Copper (Cu)	385W/mK	1083°C
Silver (Ag)	419 W/mK	962°C
Aluminum (Al)	210 W/mK	660°C
Brass (Cu-Zn)	Approximately 233 W/mK (depending on alloying elements)	Approximately 1000°C (depending on alloying elements)
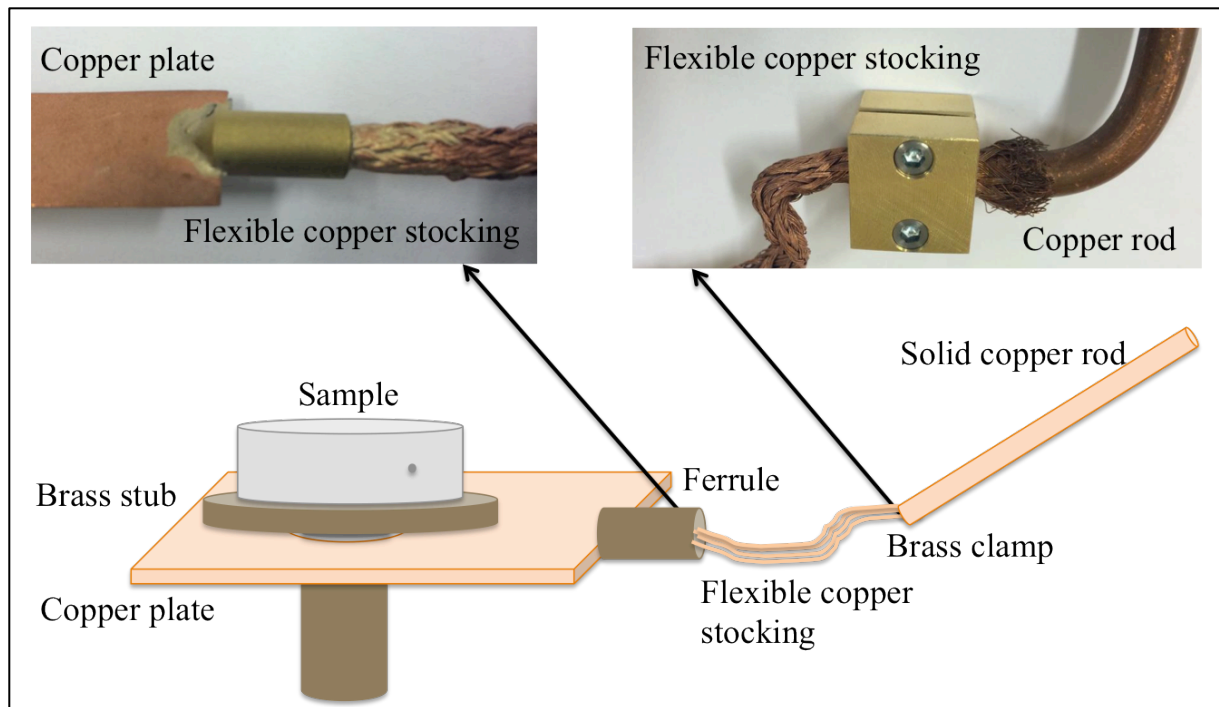
Figure 53: Schematic illustration of coldfinger components and connections

In order to be able to measure the sample temperature during cooling thermocouples were used. The thermocouples had to be directly connected to the sample. Initially, it was decided to use silver paste to connect the thermocouple on the side edge of the sample. However, since the sample is curved and smooth it was difficult to achieve good adhesion. This was resolved by drilling a small whole on the sampleside, with a diameter of 0,6mm and a depth of approximately 3mm. In order to confirm that the connection between the thermocouple and the sample was good enough and the temperature measurements were reliable, another thermocouple was silver soldered to the copper plate. The measured values were in good agreement. Furthermore, the thermocouples had to be connected to a temperature-measuring instrument via a thermocouple extension and compensation cables (TC cables). In order to extend these through the chamber walls a flange with a vacuum compatible feedthrough had to be machined. Different options were discussed and the solution was a SEM flange with a Teflon plug machined at Fine Mechanical workshop at NTNU. The TC cables were pulled trough small wholes in the Teflon plug, as shown in Figure 54. Since Teflon is sufficiently ductile the small gaps between the Teflon plug and the Teflon isolation around the wire will, when the chamber is pumped to vacuum, be sealed. The temperature set-up is illustrated in Figure 56.

The original flange for the electrical connections to the picoindenter was not compatible with our SEM, hence new screw holes had to be machined, as shown in Figure 55. To make sure that all the new flanges and especially the Teflon plug were vacuum tight they were tested, and the chamber pressure was monitored, over a period of three days.
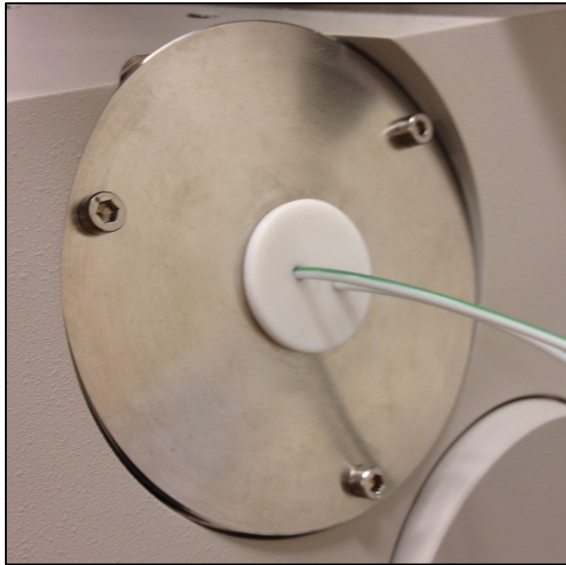
Figure 54: Temperature measurement flange

Figure 55: Picoindenter flange

Table 4: Data for temperature measurement parts

Component	Type	Diameter	Length	Measuring area
Thermocouple extension and compensating cable (TC cable)	B13 with Teflon insulation single pairs, round wire	2mm	500mm	-
Thermocouple	K-element, Cr-CrNi with miniatyr tc miniplugs	0,5mm	500mm	-180→1350 C°
Temperature measuring instrument	Testo 735-1, two inputs for probes	-	-	-200→1370 C°
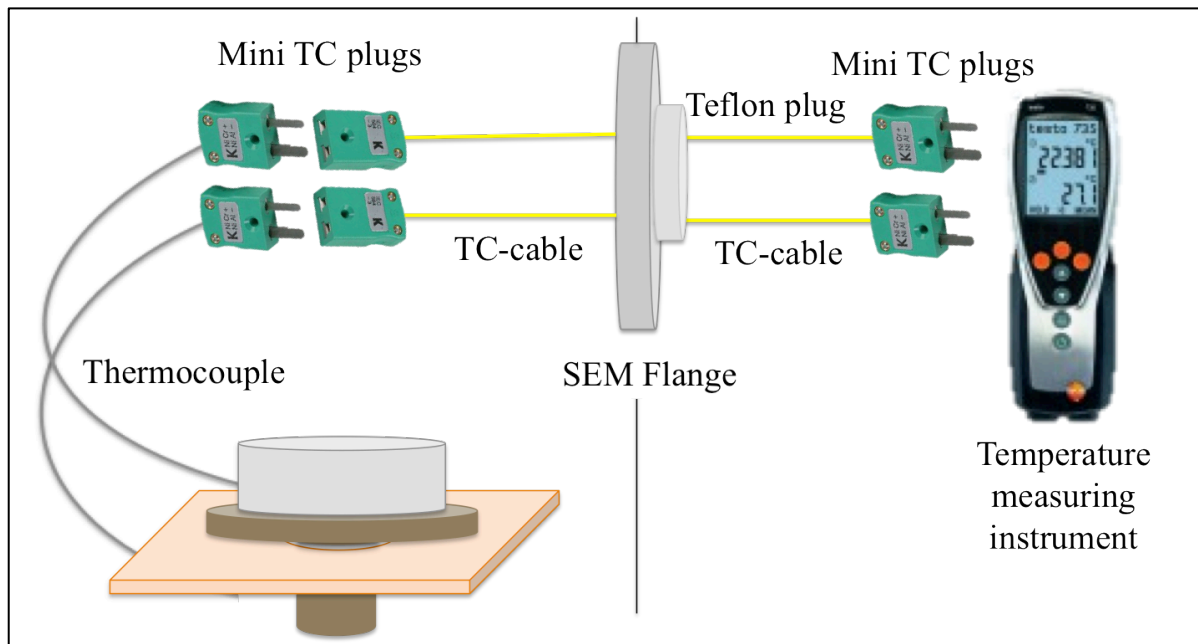
Figure 56: Schematic illustration of temperature feedthrough

With the current set-up it is not possible to control the temperature. The liquid nitrogen has a constant temperature and will continue to cool the sample until it stabilizes at a minimum; consequently additional heating is necessary in order to precisely control the sample temperature. The thermal conductivity of the coldfinger proved to be sufficient; after approximately 1,5h a temperature of -90°C was reached. Precautions were taken during the installation and handling of the equipment, and all the experiments were safely conducted. Figure 57 images the SEM chamber with all components installed.
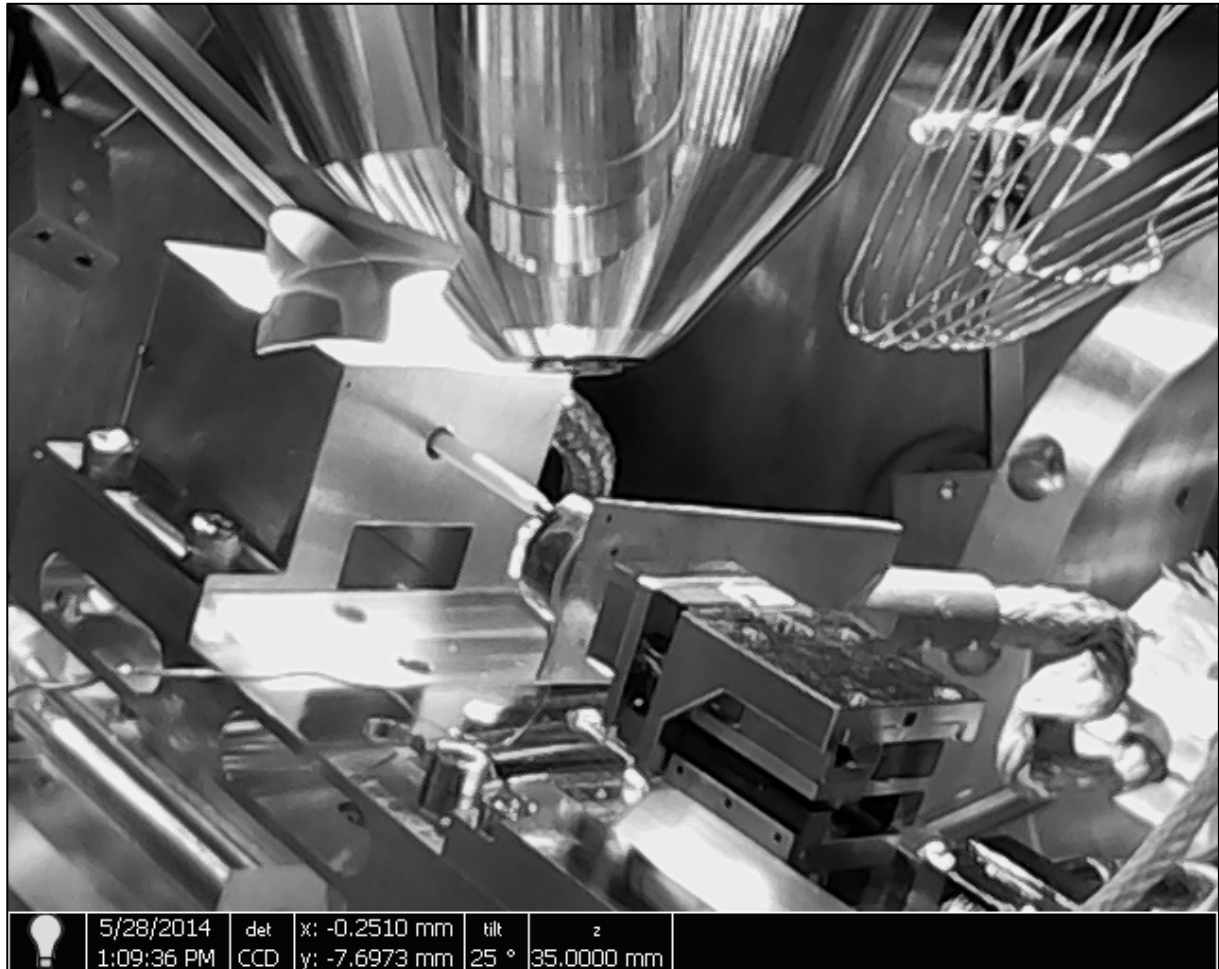
Figure 57: Image of SEM chamber with all components installed

3.6 Thermal drift

Thermal drift may affect the accuracy of the indentation process. The sample is cooled down, however the indenter tip is not. The term thermal drift refers to the change in the displacement signal, while the normal force on the indenter remains constant. Thermal drift occurs when any component in the load frame expands or contracts in response to changing thermal gradients, resulting in the measurement of apparent displacement that is not a true reflection of a material's force-displacement response. During testing at room temperature, thermal drift is generally low and assumed to be constant throughout the test. However when cooling the sample, there is potential for larger thermal gradients and fluctuations in the load frame, thus leading to higher drift rates, increased variation in drift rate from one indentation to the next, and even a progression of drift rate over the duration of a single test. The introduction of a vacuum and short indentation time reduces the drift to some extent, however it is not removed entirely.

In order to evaluate thermal drift when the sample is cooled down a series of single indents, with a berchovich tip were performed, at room temperature and at low temperature. A maximum load of 10000mN was chosen, followed by unloading down to 5000mN, the force was than hold constant for 300s before final unloading. An open loop (drift correction) feedback was used for all indentations. A typical loading curve for the performed indents is shown in Figure 58.
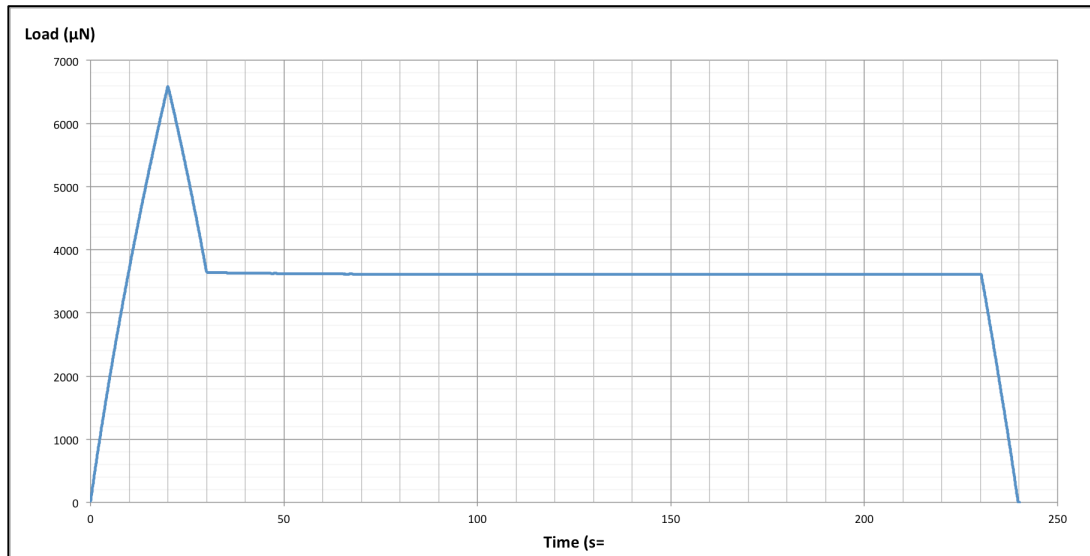
Figure 58: Loading curve

3.7 Cantilever loading

The bending experiment was carried out using a Hysitron PI 85 picoindenter placed in an FEI ESEM. The SEM stage must be correctly located, so that the indenter tip is imaged. The coordinates was determined to be; x = -1,1800 y = -15,500 R = -30. When the tip is visible in the SEM image the tilt angle must be defined. The work function of the picoindeter is optimal up 30° tilt, above this value the measured data might be inaccurate. At a 0° tilt the surface of the specimen is not visible. Different tilt angles were investigated, and optimal tilt was determined to be 25°. At 25° tilt the whole side edge of the cantilevers is visible and the top surface of the beam is recognizable making it possible to position the indent accurately. The working distance strongly affects the image quality. Due to the size of the picoindenter and limited space inside the SEM chamber a large working distance is required. An initial working distance of approximately 25mm resulted in insufficient image resolution. In order to safely handle the equipment and avoid contact between the picoindenter and SEM components like detectors etc. the working distance was decreased step by step, with the chamber door open. Between each step the chamber door was carefully closed while closely monitoring the distance between the picoindenter and SEM components. The coordinate at minimum possible working distance was determined to be z = 32, which is consistent with a working distance of approximately 15mm. When the SEM stage position is optimized, the stage will be fixed in this position during indentation.
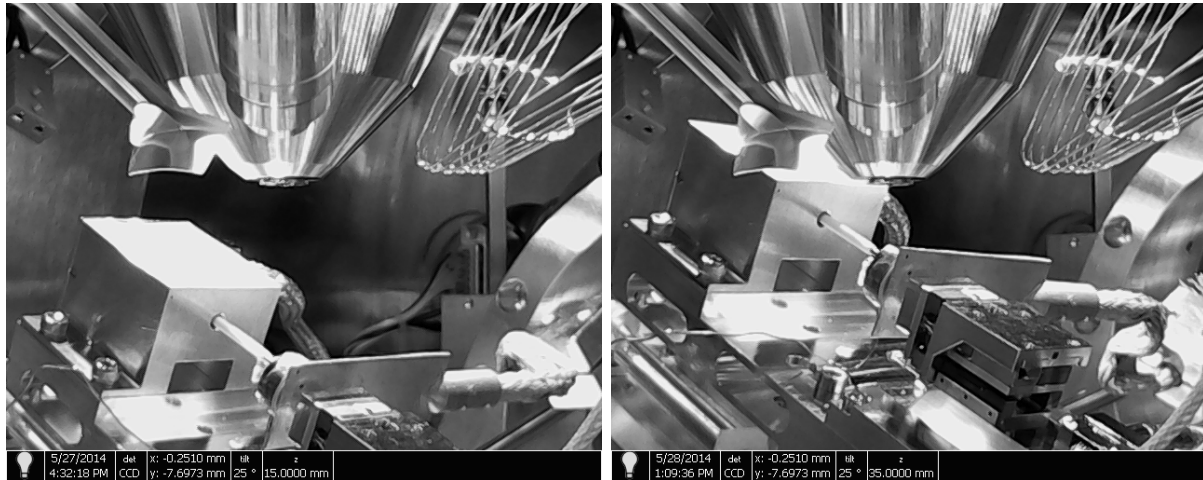
Figure 59: Images of SEM chamber with initial working distance, and reduced working distance.

The experiments was performed with a Berkovich tip, since it is sufficiently sharp to precisely position the indenter at the loading point. By this the length, from the notch at the supporting end to the contact point of loading, can be determined. The use of a sharp tip also avoids problems associated with wedge or cylindrical contact, where torque accurse from misalignment at the contact.

The movement of the picoindenter stage is restricted to 1mm in each direction. In order to be able to locate the cantilevers, the sample must be placed correctly. The picoindeneter tip is not centered at the sample surface; by rotating the sample it is possible to access different areas. If necessary it is also possible to not mount the sample completely centered at the stub. Due to the limited movement of the picoindenter stage, the positioning of the sample is a time consuming process. By the macro indentation marking the approximate position of the cantilevers can be determined visually while mounting the sample, however the exact position is not possible to know until it is visualized in the SEM. This results in a series of trial and error. Between each try the chamber needs to be ventilated, and the sample must be dismantled and re-glued to the stub. It is also important that the sample is correctly rotated so that the cantilevers are imaged from the side by the electron gun.

The indentation is performed by moving the picoindenter stage, and thereby the sample surface, towards the tip. The focus is adjusted at the indenter tip, when the sample is moved towards the tip the surface also approach focus. By this it is difficult to place the indent accurately. In order to determine accurate positioning the sample was moved to the surface near the cantilever. The shadow effect from the tip on the surface gives an indication as to how far away the sample surface is. When the tip is close to the surface an automated approach was performed; with a precise withdraw of 100nm. The sample was then moved so that the tip was centered at the fixed end of the cantilever. A new automated approach was performed; with a precise withdraw of 10nm, by this the approximate point of contact i.e. the position of the indent is determined. The tip was then moved to the cross mark on the free end of the cantilever, and another automated approach was made in order to determined an exact and correct loading point. Images form positioning of the tip is shown in Figure 60.

An image frame grabber creates a video of the SEM images during loading. The resolution, is as mentioned, limited due to the large working distance. In order to be able to distinguish the notch and the crack opening optimal image settings is required. It was also necessary to use a fairly slow scan rate (1µs) in order to reduce the image noise. The loading videos are therefore somewhat irregular and jerky. The cantilevers were tested with open loop (no feedback). The maximum load was set to 10000µN, with a loading rate of 250µN/s. It is important that the loading rate is slow enough, so that it is possible to stop the video at different points in order to measure the crack opening. In order to reduce vibrations q-control value was determined to be 0,08.
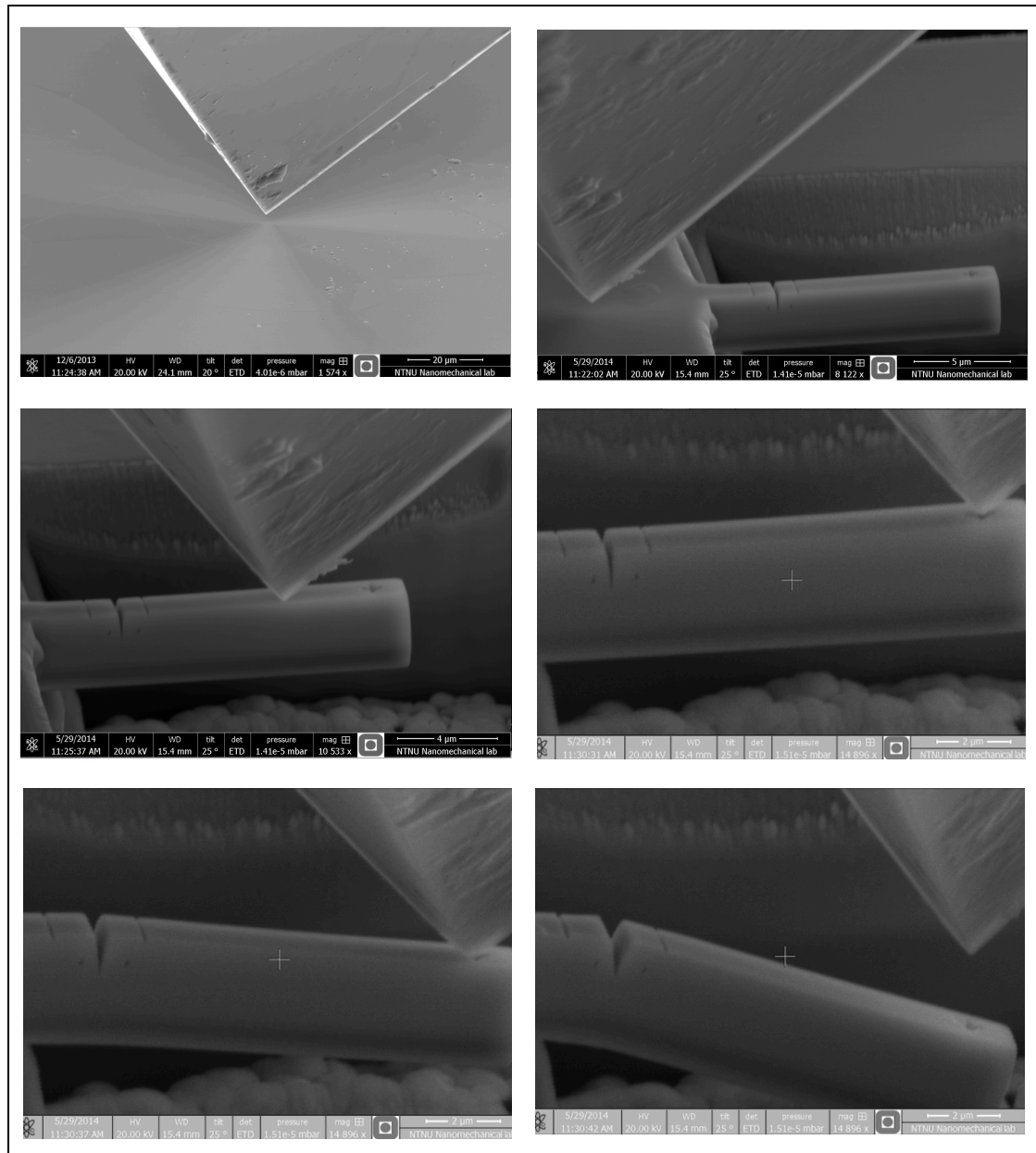
Figure 60: Images showing correct and precise positioning of the indenter.

4 Results and discussion

4.1 Cantilever dimension and quality

The milling scheme discussed in experimental details explains the main steps of the procedure. However the milling process showed hard to predict and control. The small dimensions of the beam require high accuracy in positioning of the different patterns; a small misalignment of the pattern in one of the steps may cause large deviation from the desired geometry. By this no cantilever can be treated the same, although the main steps are similar the procedure have to be evaluated and modified throughout the process. The difficulty of accurately controlling the milling procedure resulted in slightly different cantilever dimensions. Table 5 lists the different dimensions, and images of all finished cantilevers are shown in Appendix A: Cantilever dimensions. As mentioned, the fabrication of cantilevers is time consuming. If a small inaccuracy was made in one of the final steps, resulting in slightly undesired geometry the cantilevers was not rejected due to time limitations. The height was measured on both side edges of the cantilevers and an average value was determined. The cross-section area is calculated based on the width, the average height and the additional triangular shape at the bottom.

The notch is machined with a series of line pattern, placed on top of each other. When the first line pattern is finished the position is optimized and the next one is initiated. This optimization may result in slight differences in the depth of the notch over the width of the cantilever. The depth of the notch i.e. crack length on both side edges was measured, and an average value were determined. The sputtering rate also affects the notch depth; close to free edges sputtered material can easily escapes resulting in a deeper notch at the side edges compared to the depth at the center of the cantilever. It should also be mentioned that fabricating a notch by FIB milling may not produce a sharp crack tip; there might exist a small notch root radius.

Table 5: Cantilever dimensions

	Height (average) [μm]	Width [μm]	Length [μm]	Crack (average) [μm]	Cross-section area [μm^2]
Cantilever 1	1,7450	1,9100	9,4200	1,2250	4,5983
Cantilever 2	2,335	1,85	10,15	1,2042	5,6934
Cantilever 3	1,5750	1,7300	10,1500	0,8827	3,9401
Cantilever 4	1,8400	1,9500	10,0800	1,1650	5,1188
Cantilever 5	1,8600	1,9500	10,1900	1,1081	4,5240
Cantilever 6	1,3350	1,7100	10,1500	0,6091	3,4499
Cantilever 7	1,2200	1,2600	10,2300	0,8340	2,2617
Cantilever 8	1,1833	1,1300	10,0400	0,6681	1,9059
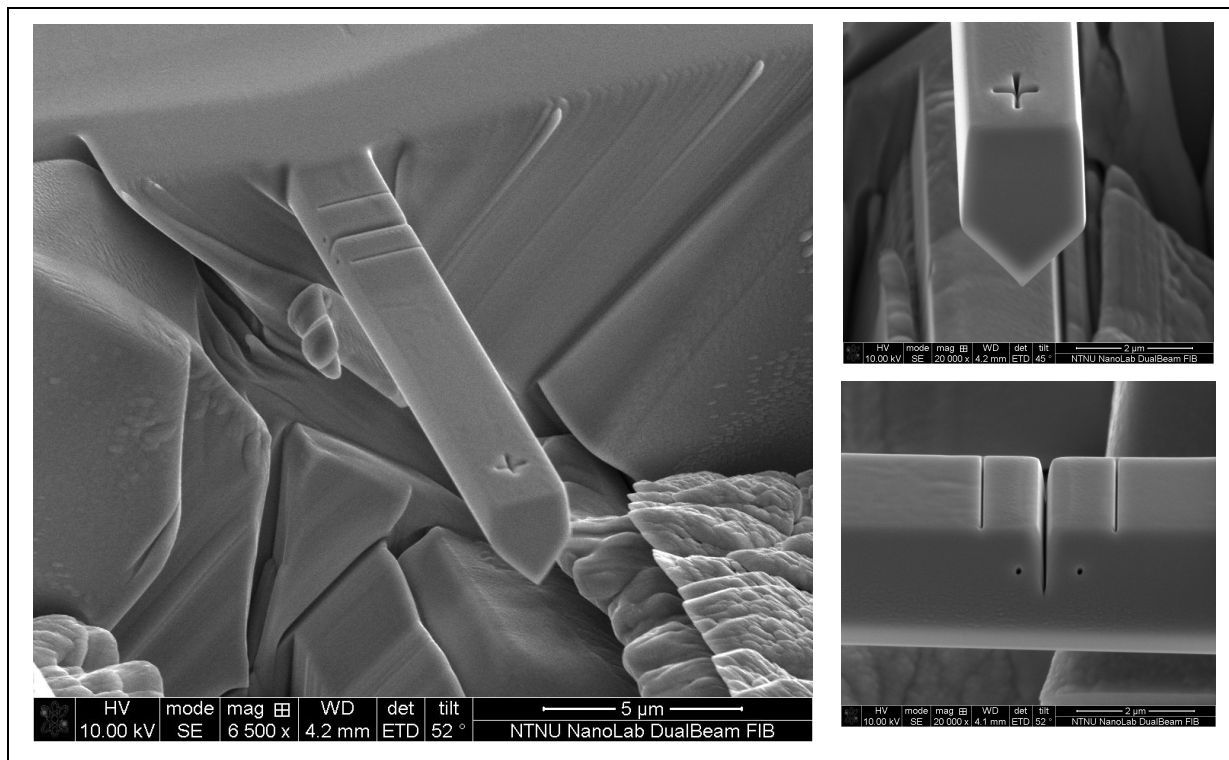
Figure 61: Example of finished cantilever with desired geometry

4.2 Thermal drift

The drift correction performed automatically by the picoindenter system includes a lift height parameter. The tip approaches the surface and the lift height withdraws the probe (10 nm - 2 µm) from the sample surface, then a drift correction is performed before the test begins. Figure 62 represent the load-displacement curve with the automatic drift control. The red curves are for the indents performed at room temperature, while the blue curves represent indents performed at low temperature (-88°C). During the holding segment the force is constant, ideally if there is no drift present, there should not be any displacement during this time. For the indents performed at room temperature minor drift values are displayed, as expected. This is seen from the short horizontal displacement at the constant force around 3600mN. However, the indentations performed at low temperature display significantly larger drift values, as seen by the long horizontal displacement at the constant force around 3600mN.

In order to confirm that the automated drift correction is reliable, the force-displacement curves without drift correction was plotted. Figure 63 indicates that the automated drift correction for the indentation performed at room temperature was applicable. The displacement during the holding segment is smaller for the curves with automated drift corrections, indicating that the influence of drift is reduced. In contrast the indents performed at low temperatures shows a significantly larger drift with automated drift corrections compared to the curves without drift correction. This indicates that the automated drift corrections at low temperatures are incorrect. Furthermore, a manual drift correction was performed. This was done in order to evaluate why the system calibrates for a wrong drift. The plot is shown in Figure 64, and will be further discussed in the following section.
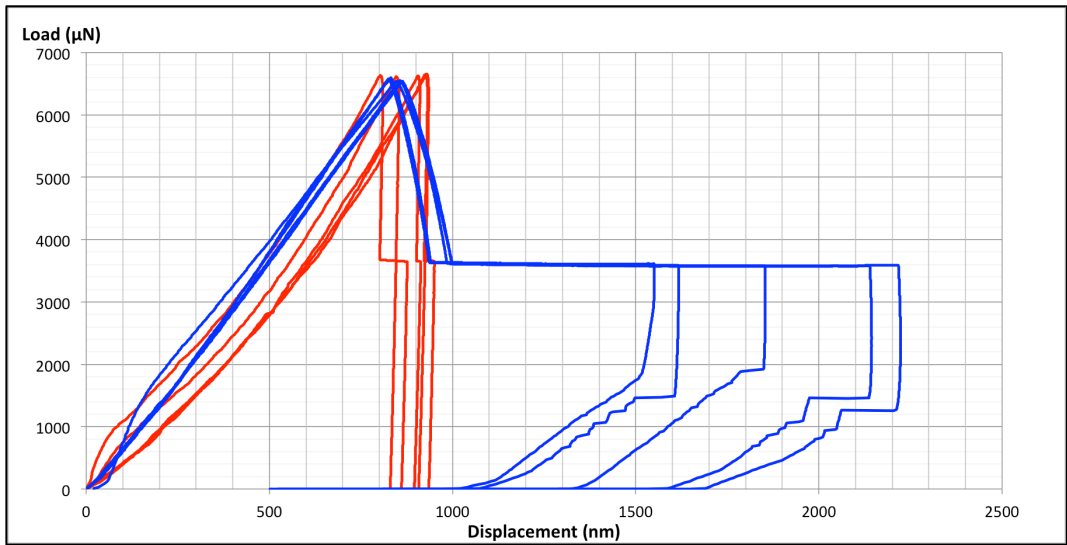
Figure 62: Single indent with holding segment - Automated drift correction
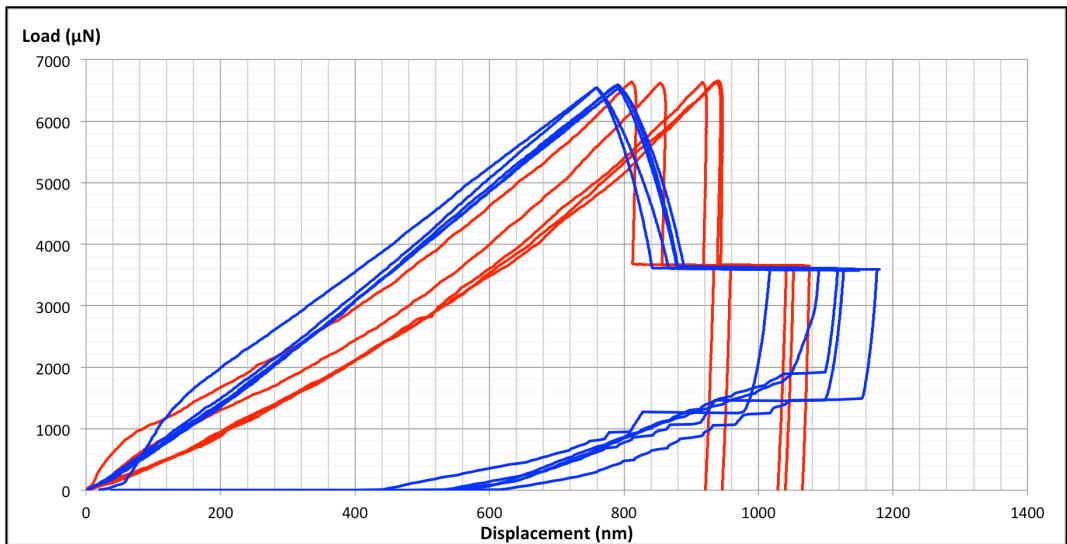
Figure 63: Single indent with holding segment - No drift correction
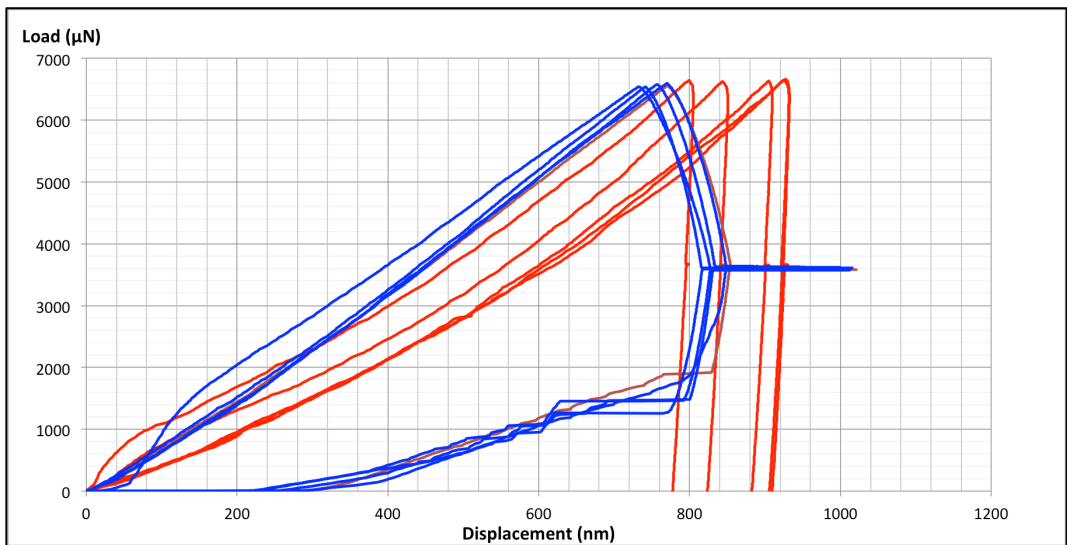
Figure 64: Single indent with holding segment - Manual drift correction

In order to illustrate the effect of the different drift correction, one indentation at room temperature were chosen and the three different drift corrections are displayed in Figure 65. The same was done for one indentation at low temperature, displayed Figure 66. The red curve represents manual drift correction, the blue curve represents no drift correction and the green curve represents automated drift correction. From Figure 65 it is seen that the automated drift correction adjusts the curve correctly, however the manual drift correction is more accurate. From Figure 66 it is seen that the automated drift correction adjust the curve incorrectly; the drift increases. The drift correction data are presented in Table 6. The values for automated room temperature corrections are roughly similar to the values achieved with manual drift corrections. However, the values for automated low temperature corrections differs from the ones obtained by manual drift correction. The values are negative, while for manual drift correction the values are positive. This explains the increased drift seen in the automated drift correction curve.
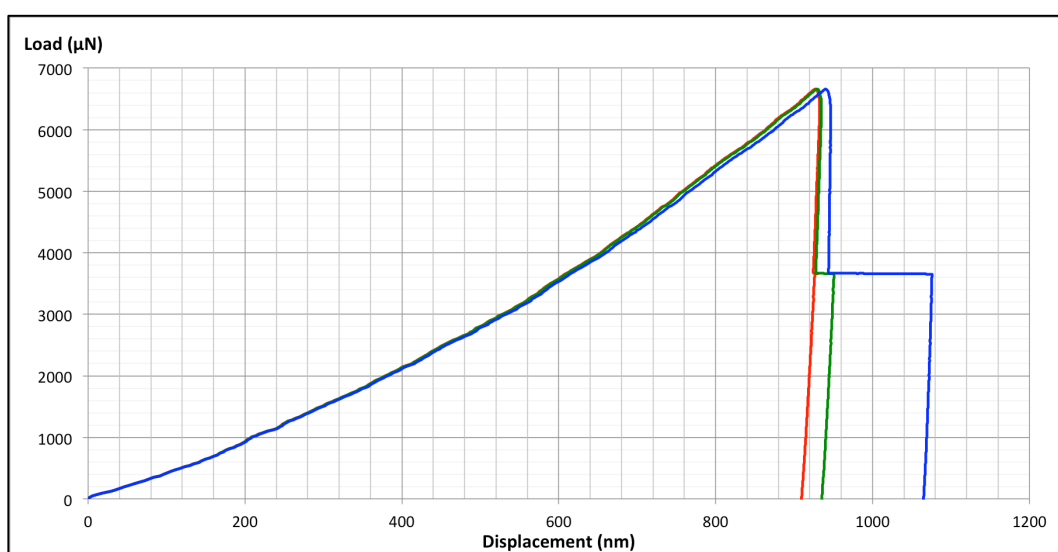
Figure 65: Single indent with holding segment - difference between no drift correction, automated drift correction and manual drift correction - Room temperature
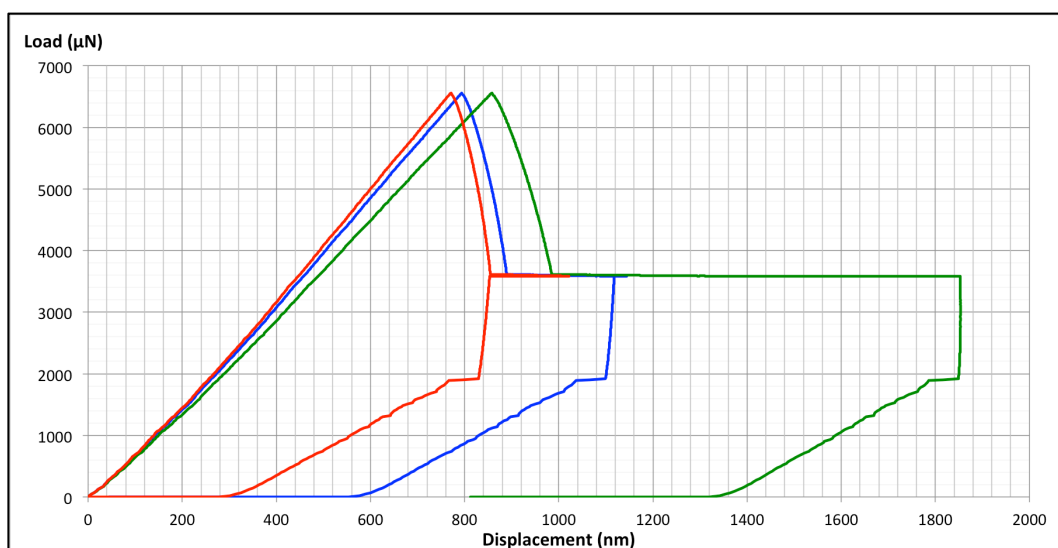
Figure 66: Single indent with holding segment - difference between no drift correction, automated drift correction and manual drift correction – Low temperature

Table 6: Drift correction data

		Automated drift correction [nm/s]	No drift correction [nm/s]	Manual drift correction [nm/s]
Room temp	1	0,5422	0	0,65
	2	0,3811	0	0,6
	3	0,5557	0	0,61
	4	0,5533	0	0,56
	5	0,3563	0	0,51
Low temp	1	-3,1923	0	1,15
	2	-5,2144	0	0,87
	3	-4,3992	0	1,3
	4	-1,9156	0	1,5
	5	-2,0035	0	1,05

In order to evaluate why the system automatically corrected with conflicting drift values, the displacement versus time with no drift correction, for the holding segment with constant force, were plotted. Figure 67 shows red curves for room temperature indentations and blue curves for low temperature indentations. At room temperature the figure shows a constant drift for all indentations. At low temperatures, on the other hand, the drift is initially very high and subsequently stabilizes over time. The drift during low temperature indentation is time dependent. It is assumed that this is due to the different temperature gradients experienced by the tip. In an early stage of the indentation the temperature difference between the tip and the sample is high. After some time the tip approaches the low sample temperature, and the temperature difference is decreased. The secant line estimated for the drift at room temperature shows that the drift is approximately 0,6nm/s. The secant line for low temperature was limited to the initially high drift data. This was done in order to evaluate a worst-case scenario for drift effect on bending experiments performed in a short time interval. The drift at the beginning of the indentations at low temperature is approximately 5,2nm/s.
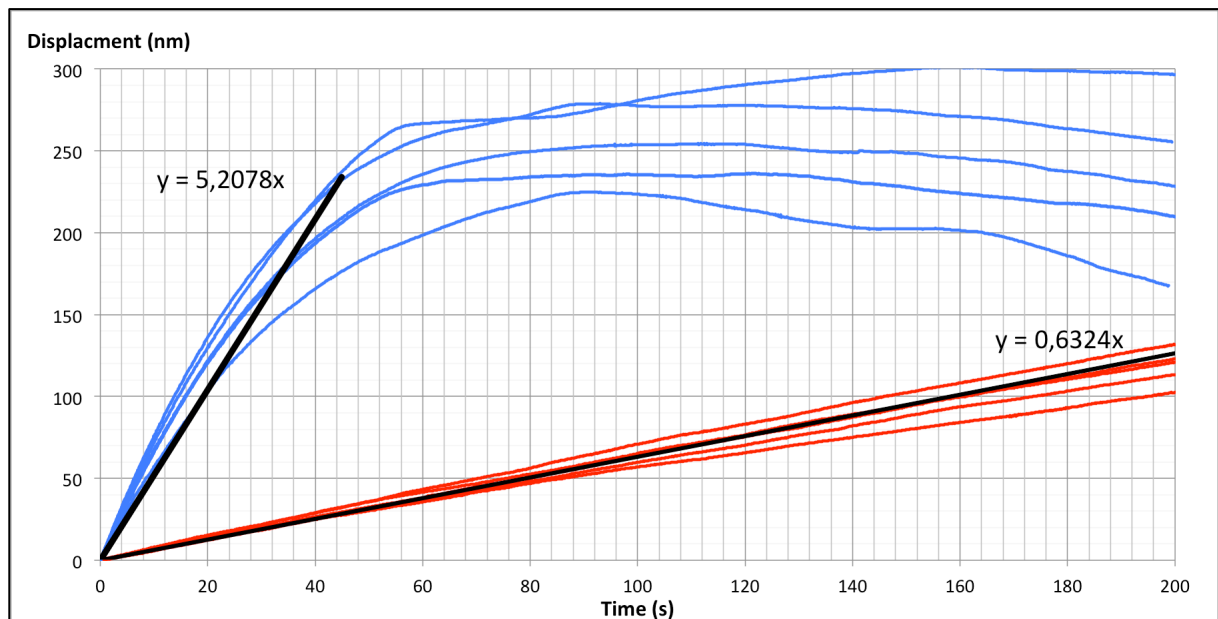
Figure 67 Drift as a function of time for the holding segment with constant force.

4.3 Cantilever loading

During cantilever loading the indentation depth can be a substantial part of the displacement. With a sharp probe the measured displacement may be a combination of cantilever deflection and indentation displacement. However, the load displacement curves with corresponding SEM imaging shows that the tip does not pierce the surface.

The load displacement curves are presented in Figure 68. Cantilevers 1 and 4 is loaded at room temperature i.e. 29 °C. Cantilever 3 is loaded at -70°C, cantilever 8 at -78°C and cantilever 5-7 at -88°C. It is seen from the figure that cantilever 1, 8 and 7 is deformed at rather low loads. This is most likely due to geometry effects. Cantilever 7 and 8 has relatively small cross-section area. For cantilever 1 the notch is machined with a different technique than the rest of the cantilever, as discussed in the experimental procedure.

Figure 68: Load displacement curves for all cantilevers.

Mechanical loading of the cantilevers may result in brittle fracture, limited crack growth and/or plastic deformation through emission of dislocations. All cantilever were plastically deformed during loading, but no fracture occurred. The drop in load for cantilever 4 and 3 might be due to crack extension, however it is not possible to visualize this in the correlated SEM videos. When the cantilevers were examined after loading deformation indicating crack growth was observed. Similar observation was also observed on cantilever 7 and 8, however, not as pronounced. This is in good agreement with the small drop in load in the load displacement curves for cantilever 7 and 8. In Figure 69 a non-linear crack tip is observed, indicating that the crack might have propagated during loading. Figure 70 shows the crack flanks after loading. The image shows that the flank surface is not smooth. This might indicate that the upper part of the flank is the initial notch, and that the bottom part of the flank is due to crack extension. However, the line on the crack flank might originate from the milling of the notch. The notch was, as mentioned, milled with a series of line pattern with slightly altered positions.
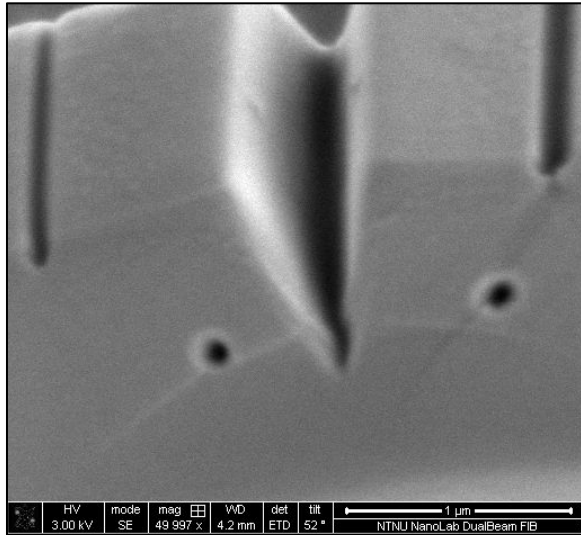
Figure 69: Cantilever 3 after loading, indication a small crack growth
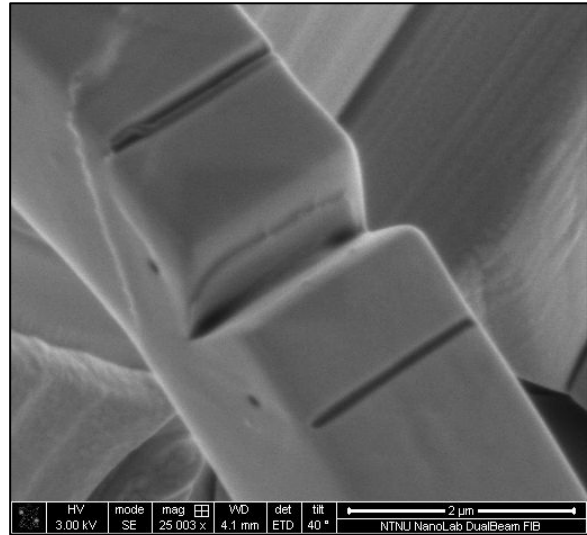
Figure 70: Cantilever 4 after loading, indicating crack growth

Cantilever 7 was loaded three times with the same parameters in order to see if any fracture occurred. The load displacement graph did not record any force i.e. the force values had a constant value of 0 when loading the second and third time. Due to the large displacement during loading and no sudden drops in load the crack extension is assumed to be ductile.
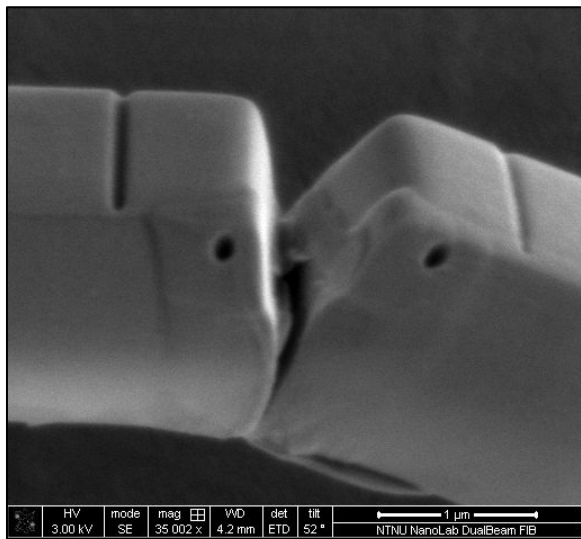
Figure 71: Cantilever 7 after third loading, showing fracture
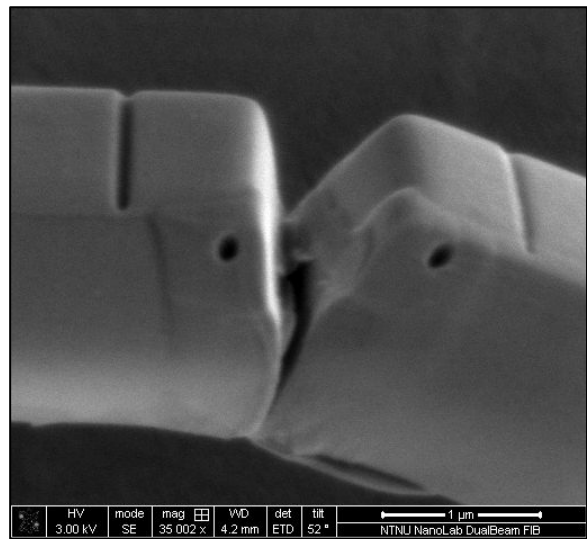
Figure 72: Cantilever 7 after third loading, showing fracture

4.4 Stress intensity factor

The preliminary stress intensity (K_Q) is normally used in order to determined the fracture toughness. Once the K_Q value is found, a series of validation requirements are needed to verify that the test result meets all the constraints and that the K value found is the fracture toughness (K_{IC}). Due to the absence of a fracture the critical tress intensity factor i.e. fracture toughness cannot be determined. However, K_Q was calculated.

A secant line was made with the slope of the tangent equal to the initial linear part of the load displacement curves. Another secant line with a slope of 95% of the first gradient was plotted. The force at the intersection between the second secant line and the load displacement curve is used to calculate the preliminary stress intensity factor.
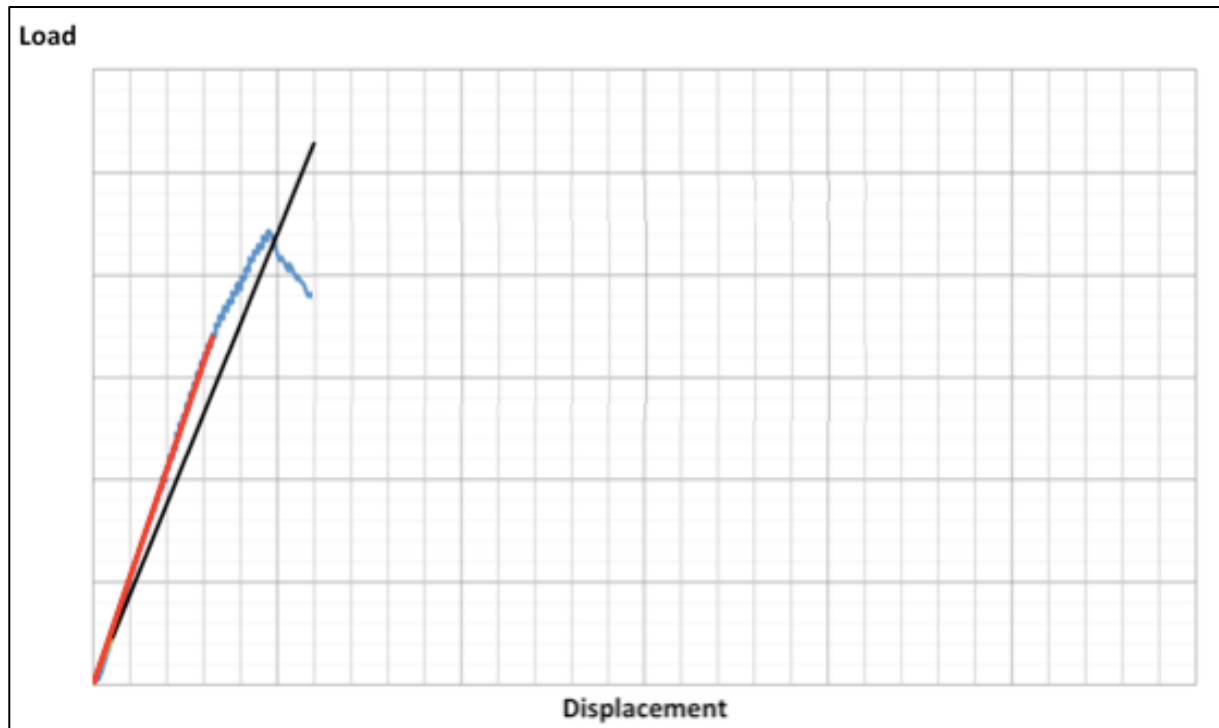
Figure 73: Illustration of load displacement curve, secant line with the slope of the tangent equal to the initial linear part of the load displacement curves and secant line with a slope of 95% of the first secant line.

Figure 74 indicates that most of the load displacement curves have a continuous progress after the interesting point. As mentioned there is a drop in load for cantilever 3 and 4. The maximum force prior to these drops is fairly close to the intersecting point. However, there is a continuous progress of the curve after the drop. The preliminary stress intensity values calculated for cantilever 3 and 4 might indicate the stress at which a small crack growth occurs, and blunting of the crack could explain the continued progress of the curve after the drop. All load displacement curves are presented individually in Appendix C: Individual load displacement curves.

K_Q values may indicate the stress value to cause the first deviation from ideal elastic behavior by dislocation movement and plastic deformation. The intersecting point between the secant line and the load displacement curve is approximately at the endpoint of the initial elastic part of the curves.
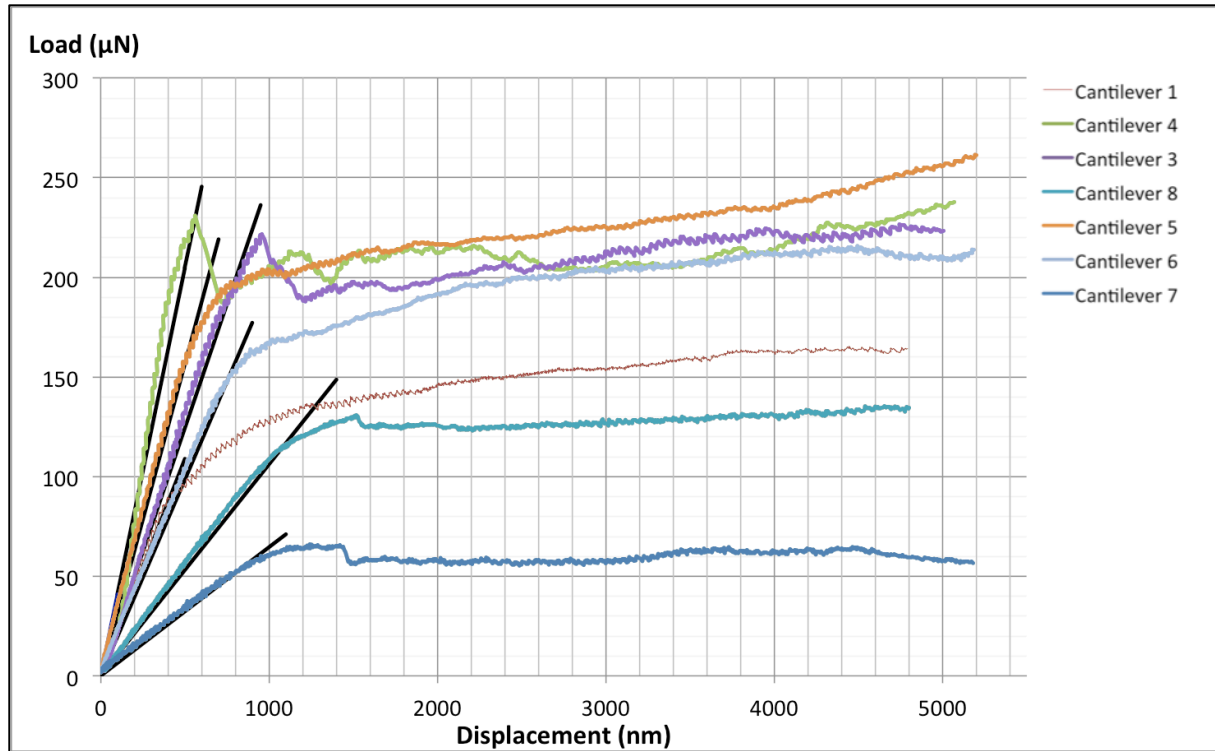
Figure 74: Illustration of secant line with a slope of 95% of the initial linear region of the load displacement curves.

As described in the theoretical background there are several different methods i.e. equations to calculate the stress intensity presented in the literature. Five different methods are presented in Table 7. Method 1 is for cantilevers with a pentagon cross-section. Method 2-5 is for cantilevers with a square cross-section. It is seen from the table that method 4 result extremely high values, compared too the other methods. To the best of my knowledge the method was only used in one paper, and the author of this paper later presented another paper where the stress intensity was calculated by method 5. By this Method 4 is excluded. Method 2,3 and 5 shows fairly similar values. Method 2 is used in several papers, including analysis of the influence of cantilevers geometry effect on the dimensionless shape factor. It is thereby decided that the values obtained with method 1 and 2 will be used for further discussion. A detailed description of all stress intensity calculations is presented in Appendix E: Calculation details.

Table 7: Stress intensity calculated by different methods

	Temp [°C]	Force [μN]	K_Q Method 1[1] [MPa√m]	K_Q Method 2[2] [MPa√m]	K_Q Method 3[3] [MPa√m]	K_Q Method 4[4] [MPa√m]	K_Q Method 5[5] [MPa√m]
Cantilever 1	29	91,860	3,4935	4,1789	4,7712	18,4703	4,6176
Cantilever 4	29	230,830	6,4594	8,1282	8,9081	34,2666	8,5667
Cantilever 3	-70	221,180	6,3176	8,8528	9,4939	37,5163	9,3791
Cantilever 8	-78	115,150	7,2438	10,8588	11,6531	45,9517	11,4879
Cantilever 5	-88	173,320	4,1949	5,3833	5,8186	22,6290	5,6572
Cantilever 6	-88	152,430	3,6636	5,7834	6,2002	26,1553	6,5388
Cantilever 7	-88	54,540	4,7903	6,5810	7,4178	28,5398	7,1349

[1] Equations (13)-(17)   [4] Equations (5) and (7)
[2] Equations (8) and (10)   [5] Equations (4) and (7)
[3] Equations (1)-(3)

The stress intensity factors calculated by Method 1 are lower than the ones calculated with method 2. Method 2, is as mentioned for cantilevers with a square cross-section, hence the additional triangular shape at the bottom of the cantilevers is not accounted for. This results in a higher crack to height ratio (a/h), which explain the deviation. The obtained values for both methods are consistent with ductile behavior. As mentioned, cantilever 1, 8 and 7 has slightly different geometry than the remaining cantilevers. If these cantilevers are excluded due to geometrical effects, the remaining cantilevers show a decreasing stress intensity factor with decreasing temperature.

Table 8: Stress intensity values and influencing factors

	Temp [°C]	K_Q (method 1) [MPa√m]	K_Q (method 2) [MPa√m]	Crack to height ratio (a/h)	Cross-section area [μm²]	Deviation between side height [μm]	Deviation between crack length [μm]	Non uni. bending
Cantilever 1[1]	29	3,5	4,1789	0,7020	4,5983	0,190	0,410	Yes
Cantilever 4	29	6,4594	8,1282	0,6332	5,6934	0,040	0,210	
Cantilever 3	-70	6,3176	8,8528	0,5604	3,9401	0,070	0,395	
Cantilever 8[2]	-78	7,2438	10,8588	0,5646	5,1188	1,094	0,593	Yes
Cantilever 5	-88	4,1949	5,3833	0,5958	4,5240	0,46	0,744	Yes
Cantilever 6	-88	3,6636	5,7834	0,4563	3,4499	0,190	0,051	Yes
Cantilever 7[3]	-88	4,7903	6,581	0,6836	2,2617	0,020	0,2358	

[1] Notch machined with different technique
[2] One side edge is shorter than the other
[3] Longer total length; the notch is machined further away from the fixed end

In figure Figure 75 the preliminary stress intensity factor calculated by method 1, for the four cantilever with similar geometry i.e. 3, 4, 5 and 6, is plotted against the temperature. It is seen by the graph that there is a drop in the preliminary stress intensity values between -70°C and -90°C. As mentioned the K_Q values may indicate the stress causing the first deviation from ideal elastic behavior by dislocation movement and plastic deformation. By this the stress at which plastic deformation starts, decrease with decreasing temperature. This is not in agreements with the literature, where it is discussed that the dislocation motion at low temperatures is restricted by the low mobility of screw dislocations.
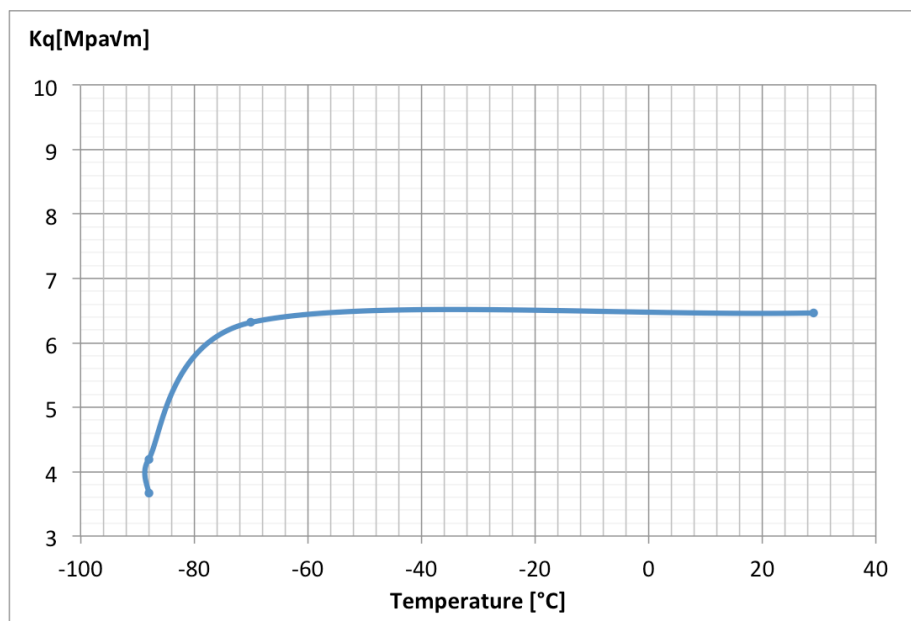
Figure 75: Preliminary stress intensity vs. temperature

As indicated in Table 8 cantilever 1, 8, 5 and 6 displayed a non-uniform bending in the lateral direction when examined after loading. Deformation consistent with compression on one side, and tension in the other side was observed. This may be due to the difference in height and/or crack length. It is seen from the table that the deviation between side heights is larges for these four cantilevers. Another explanation might be a misalignment between the picoindenter probe tip and the cantilever. The non-uniform bending in the lateral direction may affect the results, as the crack is loaded differently at the different sides. The side in tension will experience higher stress than the side in compression.
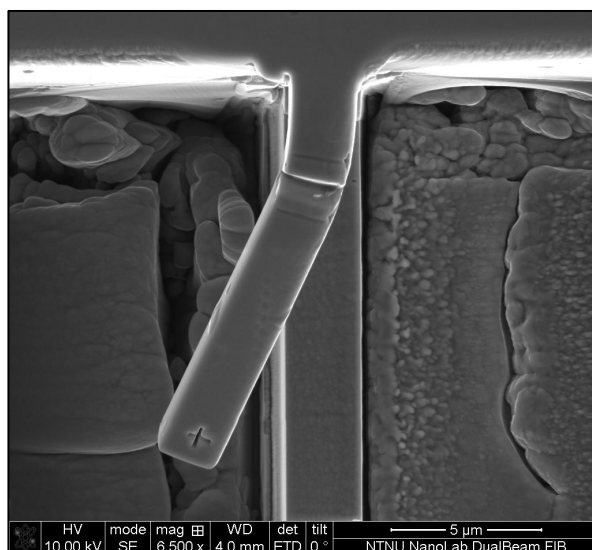
Figure 76: Example of non-uniform bending in the
lateral direction
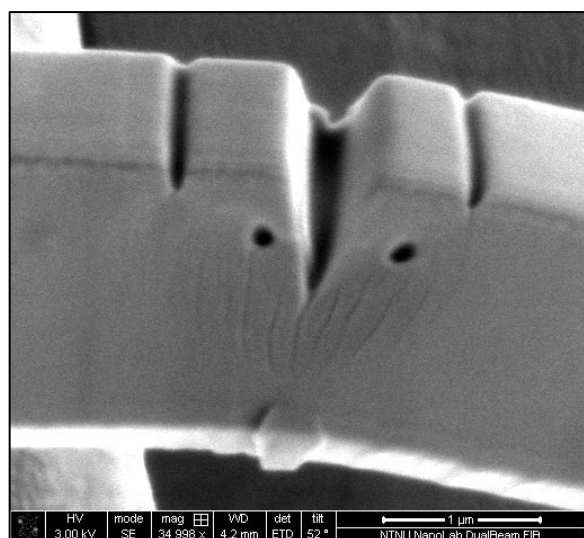
Figure 77: Cantilever 8 after loading, showing
deformation from compression
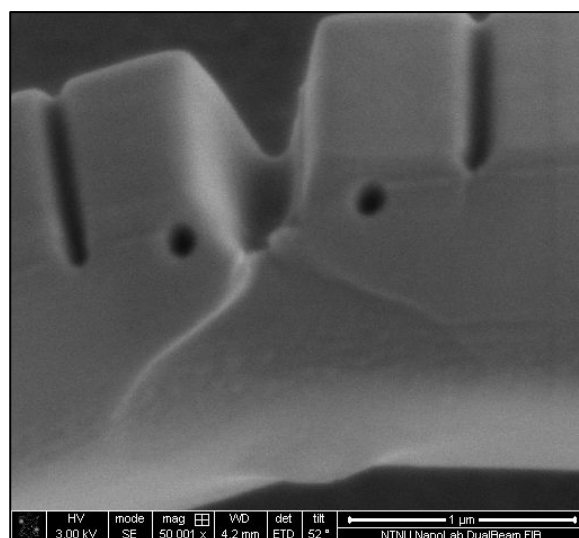
Figure 78: Cantilever 8 after loading, showing
deformation from tension

4.5 Crack Tip Opening Displacement

Direct measuring CTOD during loading was not possible. Due to the long working distance required with the picoindenter set-up the resulting image resolution was not adequate to measure these small differences in distance. CTOD was, however calculated by both the hinge model and the double gauge model. At the force used to calculate the conditional fracture toughness there is as mentioned no deformation of the cantilevers, hence there is no crack tip opening displacement to measure. The decision was made to calculate CTOD at a fixed displacement at the end of the load displacement curves i.e. 4000nm, in order to be able to compare the values.

Table 9 lists the calculated CTOD from the hinge model. CTOD was calculated using the average crack length and average height. The average height is calculated form the two measured side edges; hence the additional triangular shape on the bottom of the cantilevers is not accounted for. CTOD was also calculated using a new height. The new height is calculated from the cross-section area divided by the width. This is an attempt to account for the addition triangular area beneath the cantilevers; hence the new height will be slightly larger than the average height. It is seen from the table that all CTOD values are larger when calculated with the new height. A detailed description of the calculations is listed in Appendix E: Calculation details.

Table 9: CTOD values obtained by the hinge model

	Temp [°C]	CTOD (Average height) [µm]	CTOD (New height) [µm]
Cantilever 1	29	0,0291	0,0550
Cantilever 4	29	0,0453	0,0793
Cantilever 3	-70	0,0924	0,1477
Cantilever 8	-78	0,0643	0,1019
Cantilever 5	-88	0,0543	0,0767
Cantilever 6	-88	0,0988	0,1449
Cantilever 7	-88	0,0444	0,0882

Table 10 lists the calculated CTOD values by the double gauge model. CTOD was first calculated with the average crack length. However, a negative result raised some questions. Since there are some differences in the crack length measured on the two sides of the cantilevers, the decision was made to calculate CTOD based on the crack length on the same side as the other measurements (i.e. $CMOD_1$, $COMD_2$). It should be mentioned that the manual measurements of $CMOD_1$ and $COMD_2$ is extremely sensitive. Several independent measurements were made in order to minimize the risk of wrong or inaccurate values. A detailed description of the calculations is listed in Appendix E: Calculation details.

Table 10: CTOD values obtained by the double gauge model

	Temp [°C]	CMOD$_1$ [μm]	CMOD$_2$ [μm]	Deviation between crack length on side edges [μm]	CTOD (Average crack length) [μm]	CTOD (Crack length on measuring side) [μm]
Cantilever 1	29	0,1846	0,1218	0,410	-0,0218	0,0127
Cantilever 4	29	0,2231	0,1247	0,210	0,0331	0,0502
Cantilever 3	-70	0,3600	0,2206	0,395	0,1243	0,1770
Cantilever 8	-78	0,2537	0,1402	0,593	0,0999	0,0316
Cantilever 5	-88	0,2361	0,1434	0,744	0,0116	0,0870
Cantilever 6	-88	0,2873	0,2275	0,051	0,1505	0,1448
Cantilever 7	-88	0,2622	0,1751	0,2358	0,0680	0,0954

Figure 79 compares CTOD values obtained by the hinge model calculated with the new height, and the values obtained by the double gauge model calculated with the crack length on the measuring side. It is seen that the values does not correlate. The double gauge model is probably the most accurate method since it is a direct approach and independent of the global behavior, whereas the hinge model relies on accurate values for the rotational center. However, the measurements of CMOD$_1$ and CMOD$_2$ are extremely sensitive to inaccurate measurement. The deviation is larges for the smallest CTOD values. This might indicate that the possibility of inaccurate measurement of COMD increase with decreasing measuring length.
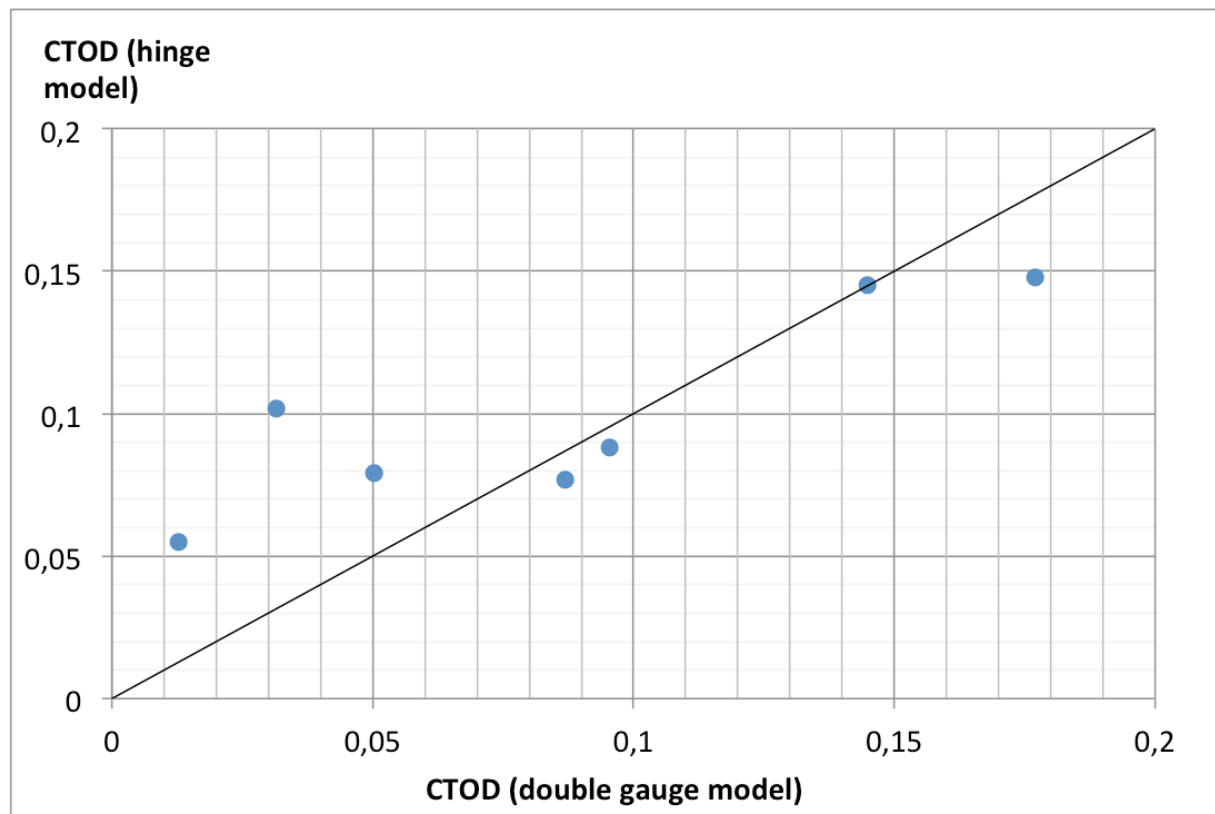
Figure 79: CTOD calculate by the double gauge model vs. CTOD calculate by the hinge model

5 <u>Conclusions</u>

A cooling system interfaced with an in-situ test set-up involving a picoindenter mounted in a Scanning Electron Microscope (SEM), have been constructed. The cooling system consists of a liquid nitrogen tank mechanically connected to the sample via a coldfinger. The thermal conductivity of the cooling system proved sufficient; after approximately 1,5h a temperature of -90°C was reached. Loading of cantilevers at room temperature, -70°C and -90°C were successfully conducted.

The use of a picoindenter combined with a Scanning Electron Microscope (SEM) has shown to be a valuable tool since it allows events observed in the mechanical data to be correlated directly with the corresponding deformation mechanisms witnessed through the electron microscope. In-situ nanomechanical testing at low temperatures is a powerful method, suitable for analyzing brittle fracture behavior at a micron scale.

Mechanical loading of the cantilevers may result in brittle fracture, limited crack growth and/or plastic deformation through emission of dislocations. All cantilever were plastically deformed during loading, but no fracture occurred. Due to the absence of fracture the critical stress intensity factor, i.e. fracture toughness, could not be determined. However the preliminary stress intensity, (K_Q) was calculated using five different methods. The results showed a drop in the preliminary stress intensity values between -70°C and -90°C. The K_Q values may indicate the stress causing the first deviation from ideal elastic behavior by dislocation movement and plastic deformation. By this, the stress at which plastic deformation starts, decrease with decreasing temperature.

It was not possible to measure the Crack Tip Opening Displacement (CTOD) directly during in-situ experiments, due to low image resolution. However, CTOD was calculated with two different methods: the hinge model and the double gauge model, both relying on the measurements of CMOD during loading. CTOD values for the two different methods were compared, however, they did not correlate. The double gauge model is probably the most accurate method since it is a direct approach and independent of the global behavior, whereas the hinge model relies on accurate values for the rotational center.

6 Further work

The work carried out in this project has revealed promising new developments within the field of nanomechanical testing. However, some areas are in need of further considerations.

With the current cooling set-up it is not possible to control the temperature. The liquid nitrogen has a constant temperature and will continue to cool the sample until it stabilizes at a minimum; consequently heating is necessary in order to precisely control the sample temperature. By this an additional heating component connected to the cooling system has to be developed.

When ventilating the SEM chamber after in-situ bending experiments at low temperatures, the copper rod is covered in rime. If the dismantling of the copper rod is not done with extreme care, it might cause contamination of the SEM chamber. However, removal of the remaining liquid nitrogen from the container might reduce the rime problem. This is achievable with a heating device; when the heating device is place in the container the liquid nitrogen will quickly evaporate.

Thermal drift may affect the accuracy of the indentation process. The sample is cooled down, however the indenter tip is not. Thermal drift occurs when any component in the load frame expands or contracts in response to changing thermal gradients. The thermal drift during indentation at low temperature was demined to be approximately 5,2nm/s. This might result in the measurements of apparent displacement that is not a true reflection of a material's force-displacement response. In order avoid thermal drift effects during cantilever loading, a constant temperature of the probe equal to the sample should be maintained. Additional cooling directed at the indenter tip is necessary.

In collaboration with my supervisor the decision was made to use polycrystalline single-phase bcc α-iron for the fracture toughness testing procedure. It is crucial to comprehend the local deformation behavior of iron before attempting to understand the deformation behavior of intricate steel alloys. The present work has lead to a better fundamental understanding of fracture experiments on a small scale. A natural continuation of the present work would be to perform experiments on more complex materials used in arctic environment.

The nanomechanical testing procedure at low temperatures exhibit exciting possibilities, The multiple-barrier recognized that in order to result in macroscopic brittle fracture, there are several different barriers that have to be overcome. The application of this model puts higher requirements on determination of local material properties such the local crack-arrest and quantitative information on local stress requirements for crack propagation. These barriers and properties are temperature dependent; hence low temperature fracture experiments at microscale may contribute to the development of this model. Further development of innovative nanomechanical testing techniques could also lead to a better understanding bcc deformation behavior at low temperatures and subsequently contribute to explain the fundamental mechanisms that control the ductile to brittle transition.

7 **Acknowledgments**

8 Bibliography

[1] T L Anderson, "*Frcture Mechanics Fendamentals and principals*" *chapter 5*, 3rd ed. USA: CRC Press, Taylor and Francic Group, 2005.

[2] K H D H Bhadeshia and Sir R Honeycombe, "*Steels Microstructure and Properties*" *chapter 11*, 3rd ed.: Elsevier, 2006.

[3] W T Becker and S Lampman. "Fracture Appearance and Mechanisms of Deformation and Fracture". [Online]. http://jpkc.fudan.edu.cn/picture/article/348/1b/ee/6dce0ae740cf8673b53e4e96abb8/6ad0c8ee-53c3-4790-a931-211df202df69.pdf

[4] J Hjelen, "*Scanning electron-mikroskopi*".: Metallurgisk Institutt, NTNU, 1989.

[5] C Thaulow, "*Brittle to ductile Trasition*" *Lecture notes TMM4162, Atomistic and Multiscale Material Modeling and Testing, NTNU.*, 2014.

[6] B R S Rogne, ""Applications of Focused Ion Beam (FIB) on Arctis Steels" Master Thesis," Department of Product Development and Materials, NTNU, 2010.

[7] D Roylance. (2001) "Yield and Plastic Flow" Department of Materials Science and Engineering Massachusetts Institute of Technology Cambridge. [Online]. http://ocw.mit.edu/courses/materials-science-and-engineering/3-11-mechanics-of-materials-fall-1999/modules/yield.pdf

[8] T Yalcinkaya. (2011) "Microstructure evolution in crystal plasticity: strain path effects and dislocation slip patterning" Master thesis, Netherland Institure for MAterial Research. [Online]. http://alexandria.tue.nl/extra2/716655.pdf

[9] C H Ersland, ""Atomistic modeling of failure in iron" Doctoral Thesis," Department of Engineering Desing and MAterials, NTNU, 2012.

[10] S Naamane, G Monnet, and B Devincre, "Low temperature deformation in iron studied with dislocation dynamic simulations," *International Journal of Plasticity 26 (2010) 84-92*, 2010.

[11] D Calliard, "Kinetica fo dislocations in pure Fe. Part I. In situ straining experiments at room temperature," *Acta Materialia 58 (2010) 3493-3503*, 2010.

[12] D Calliard, "Kinetics of dislocations in pure Fe. Part II. In situ straining experiments at low temperature," *Acta MAterialia 58 (2010) 3504-3515*, 2010.

[13] D Caliiard, "ON stress discrepancy at low-temperatures in pure iron ," *Acta materialia 63 (2014) 267-275*, 2014.

[14] A Lambert-Perlade, A F Gourdues, J Besson, T Sturel, and A Pineau, "Mechanisms and Modeling of Cleavage Fracture in Simulated Heat.Affected Zone MIcrostructure of a High-Strength Low Alloy Steel," *Metallurgical and Materials Transactions A, Volume 35A March 2004 1039-1053*, 2004.

[15] A M Minor and C A Volkert et al, "Focused Ion Beam Microscopy and Micromachining," *MRS Bulletin Vol 32 May 2007*, 2007.

[16] J Wheeler. "FIB Milling of a GaAs pillar", Downloaded 04.04.2014. [Online]. https://www.youtube.com/watch?v=JPPD5jAwFpM

[17] J Gong and A J Wilkinson, "Anisotropy in the plastic flow properties of single-crystal alpha titanium determined from micro-cantilever beams," *Acta Materiala 57 (2009) 5693-5705*, 2009.

[18] B Z Kupfer, R K Ahmad, A Zainal, and B Jackman, "Fabrication and characterisation of trangule-faced single crystal dimond micro-cantilevers," *Dimond & Related Materials 19 (2010) 742-747*.

[19] Y L Chan, A H W Ngan, and N M King, "Use of focused ion beam milling for investigating the mechanical properties of biological tissues: A study of human primary molars," *Journal of the Mechanical Behaviour of Biomechanical Materials 2 (2009) 375-383*, 2009.

[20] X Zhao, R M Langford, J Tan, and P Xiao, "Mechanical properties of SiC coatings on spherical particles masured using micro-beam method," *Scripta Materialia 59 (2008) 39-42*.

[21] D E J Armstrong, A J Wilkinson, and S G Roberts, "Micro-mechanical measurments of fracture toughness of bismuth embrittled copper grain boundaries," *Philosophical magazine vol 91, no 6, 394-400*, 2011.

[22] F A Stievie and L A Giannuzzi, "*Introduction to Focused Ion Beam*". USA: Springer, 2005.

[23] B R Sørås Rogne and C Thaulow, "Investigation of Nanomechanical Test Methods on Arctic Steel," in *International Offshore and Polar Engineering Confrence* , 2011.

[24] D Kupka and E T Lilleodden, "Mechanical testing of solis-solid Intefaces at the micronscale," *Experimental Mechanics (2012) 52:649-658*, 2012.

[25] J E Darnbrough, D Lui, and P E J Flewitt, "Micro-scale testing of ductile and brittle cantilever beam beam specimens in-situ with a dualbeam workstation," *Mesurment Science and Technology 24 (2013) 055010*, vol. 2013.

[26] C Motz, T Schöberl, and R Pippan, "Mechanical properties of micro-sized copper bending beams machined by the focuse ion beam technique," *Acta Materialia 53 (2005) 4269-4279*, 2005.

[27] S Massl, W Thomma, J Keckes, and R Pippan, "Investigation of fracture properties of magnetron-sputtered TiN films by means of FIB-based cantilever bending technique," *Acta Materialia 57 (2009) 1768-1776*, 2009.

[28] K Takashima, T Higo, S Sugiura, and M Shimojo, "Fatigue crack growth behaviour of micro-sized specimens prepared from electroless plated Ni-P amorphous alloy thin film," *Materials Transactions Vol 42 No 1 68-73*, 2001.

[29] K Takashima and Y Higo, "Fatigue and fracture of Ni-P amorphous alloy thin film on the micrometer scale," *Fatigue & Fracture of Engineering Materials & Structure 28 703-710*, 2005.

[30] K Takashima, Y Higo, and M V Swain, "Fracture toughness test for micro-sized specimens," in *International Confrence on Fracture USA ICF10 0193OR*, 2001.

[31] J McCarthy, Z Pei, M Becker, and D Atteridge, "FIB micromachined submicron thickness cantilevers for the study of thin film properties," *Thin Solid Film, Volume 358, Issues 1–2, 2000, 146–151*, 2000.

[32] S Wurster, C Motz, M Jenko, and R Pippan, "Micrometer-sized SPecimen Preparation Based on Ion Slicing Technique," *Advanced Engineering Materials 2010 12 No 1-2*, 2010.

[33] S Wurster, C Motz, and R Pippan, "Characterization of the fracture toughness of micro-sized tungsten single crystal notched specimens," *Philosophical Magazine Vol 92 No 14 1803-1825*, 2012.

[34] X Zhu and J A Joyce, "Review of fracture toughness (G, K, J, CTOD, CTOA) testing and standardization," *Engineering Fracture Mechanics 85 (2012) 1-46*, 2012.

[35] D E J Armstrong, A S M A Haseeb, S G Roberts, A J Wilkinson, and K Bade, "Nanoindentation and micro-mechanical fracture toughness of electrodeposited nanocrystalline Ni-W alloy film," *Thin solid films 520 (2012) 4369-4372*, 2012.

[36] S Wurster, C Motz, and R Pippan, "Notched-cantilever testing on the micrometer scale - Effects of constrains on plasticity and fracture behaviour," in *European Confrence on Fracture, Dresde, Germany, 2010*.

[37] ASTM Standard, "Standard test methof for linear-eleastic plane-strain fracture toughness Kic of metallic materials ," 2013.

[38] K Matoy et al., "A compartive micro-cantilever study of the mechanical behaviour of silicon based passivation films," *Thin soli films 518 (2009) 247-256*, 2009.

[39] J Schaufler, C Schmid, K Durst, and M Göken, "Determination of the interfacial strength and fracture toughness of a-C:H coatings by in-situ microcantilever bending," *Thin solid films 522 (2012) 480-484*, 2012.

[40] F Iqbal, J Ast, M Göken, and K Durst, "In situ micro-cantilever tests to study fracture properties og NiAl single crystals," *Acta Materialia 60 (2012) 1193-1200*, 2012.

[41] D D Maion and S G Roberts, "Measuring fracture toughness of coatings using focused-ion-beam-mechined microbeams," *Journal of materials research vol20 no2 2005*, 2005.

[42] S Ahmad and K Durst. "Fracture simulations od micro-cantilever beams unsing Finite element modeling" Mini project; Friedrich-Alexander-Universität Erlangen-Nürnberg. [Online]. http://elite-map.tf.uni-erlangen.de/documents/Fracture%20simulations%20of%20micro-cantilever.pdf

[43] T L Anderson, "*Fracture Mechanics - Fundamentals and applications*" *page 61-64*, 3rd ed.: Tyalor and Francis Group, LLC, 2005.

[44] E Taki, Y Kawakami, and K Takashima, "Fracture behvaiour of micro.sized Fe3%Si alloy single crystals," *Journal of Solid Mechanics and Material Engineering Vol1 No6* , 2007.

[45] H Gao and Y Hugang, "Geometrically necessary dislocation and size dependent plasticity," *Scripta Materialia 48 (2003) 113,118*, 2003.

[46] E Demir, D Raabe, and F Roters, "The mechanical size effect as a mean-field breakdown phenomenon: Example of microscale single crystal beam bending," *Acta Materialia 58 (2010) 1876-1886*, 2010.

[47] J R Greer, W C Oliver, and W D Nix, "Size dependence of mechanical properties of gold at the micron scale in the absence ," *Acta MAterialia 53 (2005) 1821-1830*, 2005.

[48] W D Nix, J R Greer, G Feng, and E T Lilleodden, "Deformation at the naometer and micrometer length scales: Effects og strain graidients and dislocation stravation," *Thin Solid Films 151 (2007) 3152-3157*, 2007.

[49] B R S Rogne and C Thaulow, "Strengthening mechanisms of iron pillars," *Not yet published, preprint submitted to Philosophical Megiazine*, 2014.

[50] B R S Rogne and C Thaulow, "Effecct of crystal orientation on the strengthening of iron pillars," *Not yet published, preprint submitted to Materials Science and Engineering*, 2014.

[51] T L Anderson , "*Fracture Mechanics Fundamentals and applications*" *chapter 3.1*, 3rd ed. USA: CRC Press, Taylor and Fracis group, 2005.

[52] G P Nikishkov, J Herens, and K H Schwalbe, "Transformation of CTOD d5 to CTOD dbs and J-intergral for 3PB- and CT-specimens," *Engineering fracture mechanics 63 (1999) 573-589*, 1999.

[53] E M Castrodeza, J E Perez Ipin~a, and F L Bastian, ""Fracture toughness evaluation of unidirectional fibre metal laminates using traditional CTOD (d) and Schwalbe (d5) methodologies"," *Engineering Fracture Mechanics 71 (2004) 1107–1118*, 2004.

[54] E N Johnston. (2012) "Stable tearing chractreization of three materials with three methods" Master thesis, Kansas State University. [Online]. http://krex.k-state.edu/dspace/bitstream/handle/2097/14386/ElizabethJohnston2012.pdf?sequence=3

Appendix A: Cantilever dimensions
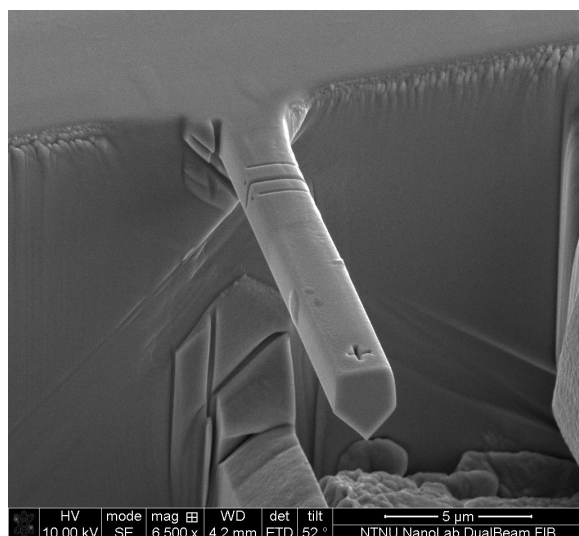
Figure 80: Beam 1
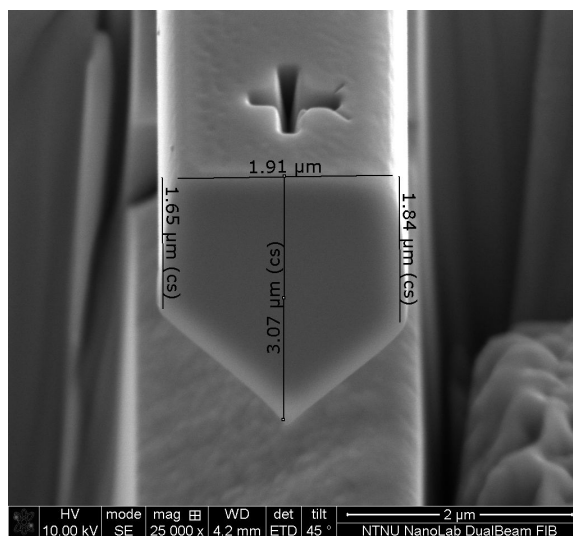
Figure 81: Cross-section
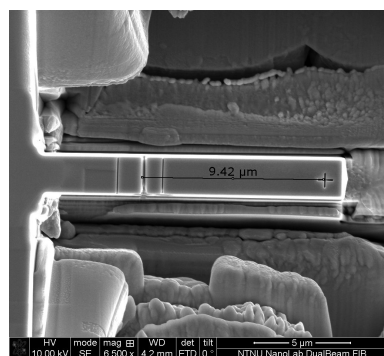
Figure 82: Top view
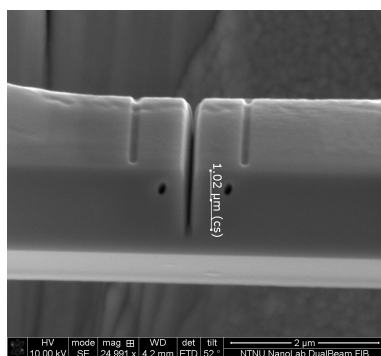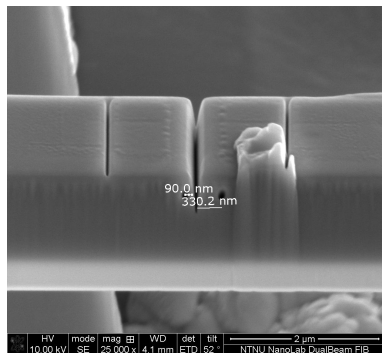

Figure 83: Crack, side 1
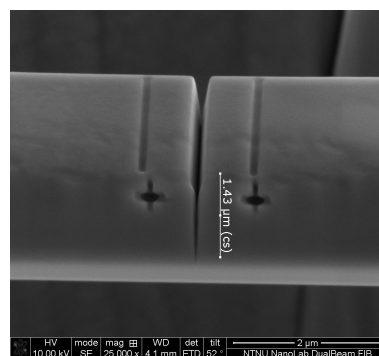
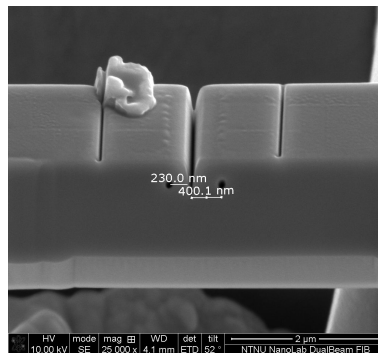Figure 84: Crack, side 2
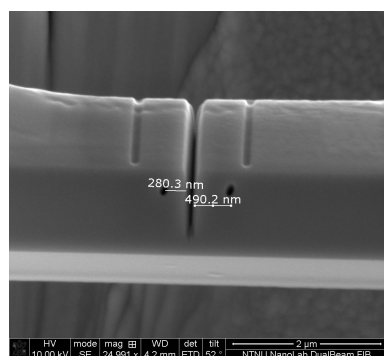
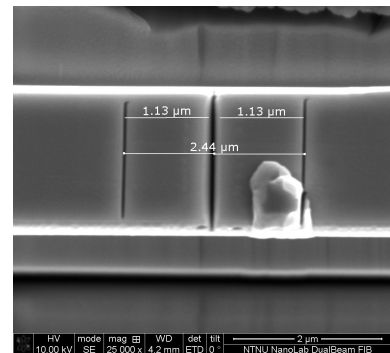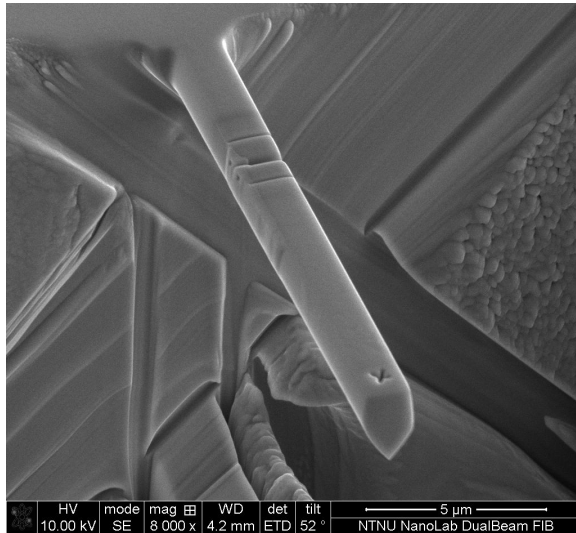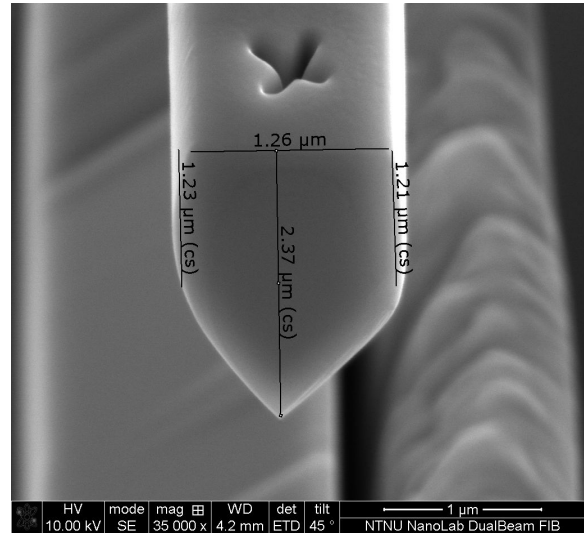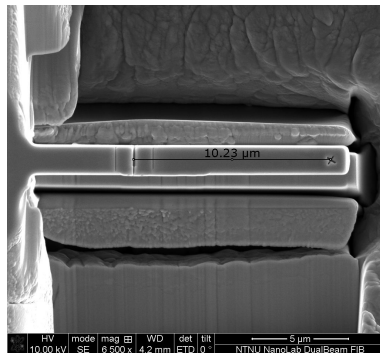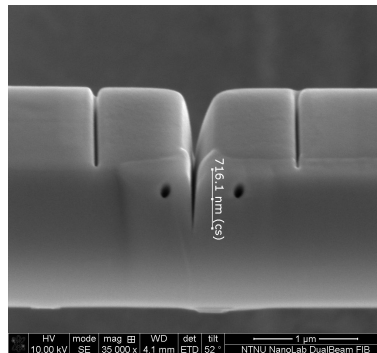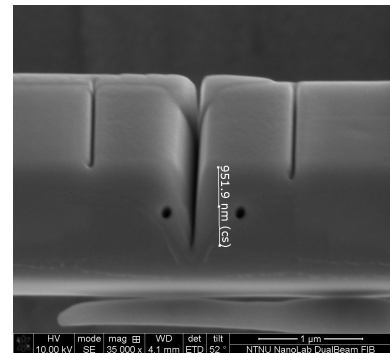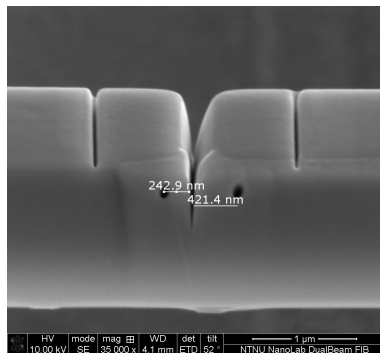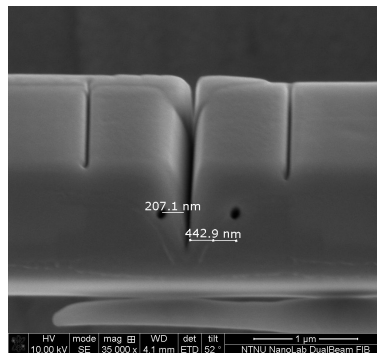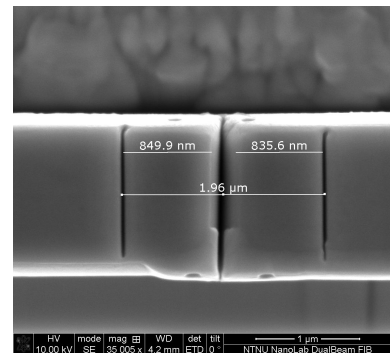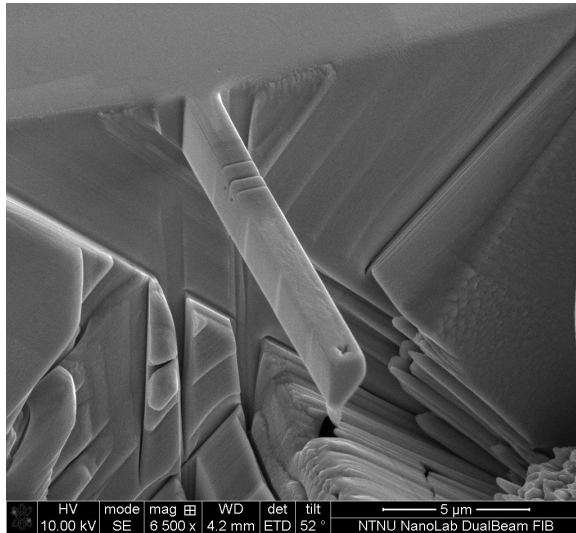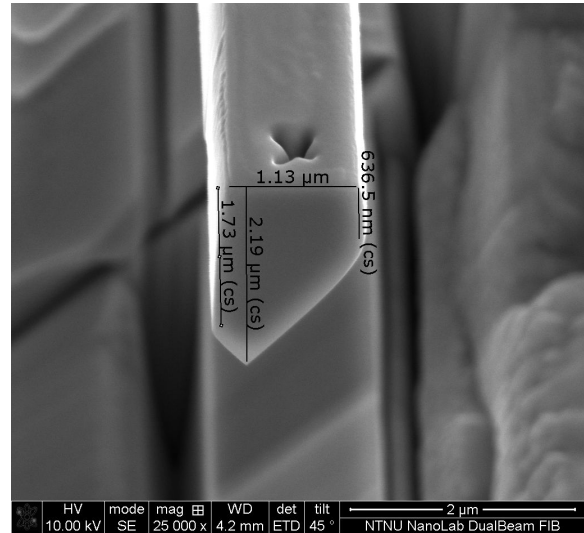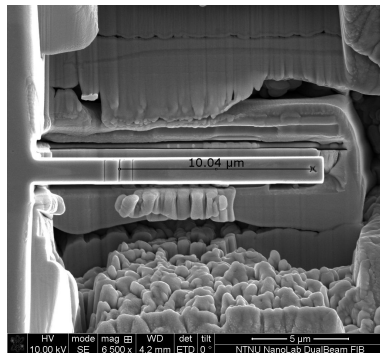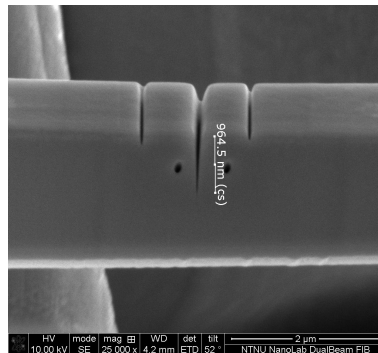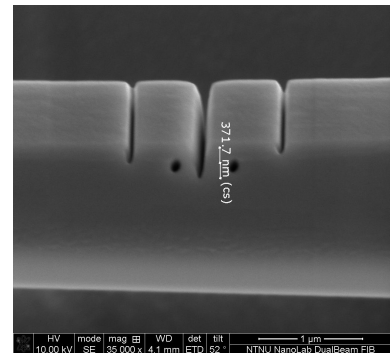Figure 85: Side mark, side 1
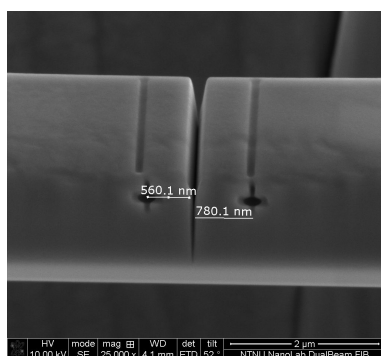
Figure 86: Side mark, side 2
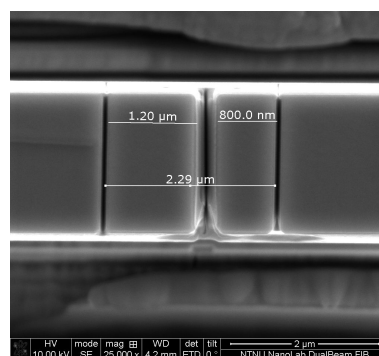
Figure 87: Top mark

Dimension	Value
Height	1,65 / 1,84 μm
Width	1,91 μm
Length	9,42 μm
Crack length, side 1	1,02 μm
Crack length, side 2	1,43 μm
Side mark, side 1	280,3 / 490,2 nm
Side mark, side 2	560,1 / 780,1 nm
Top mark	2,29 μm
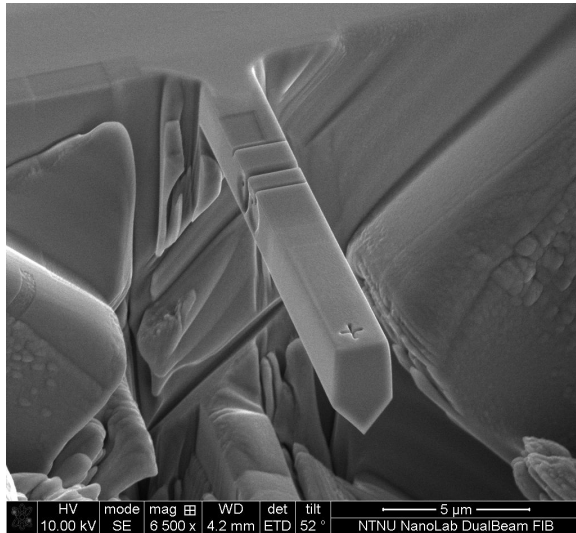
Figure 88: Beam 2
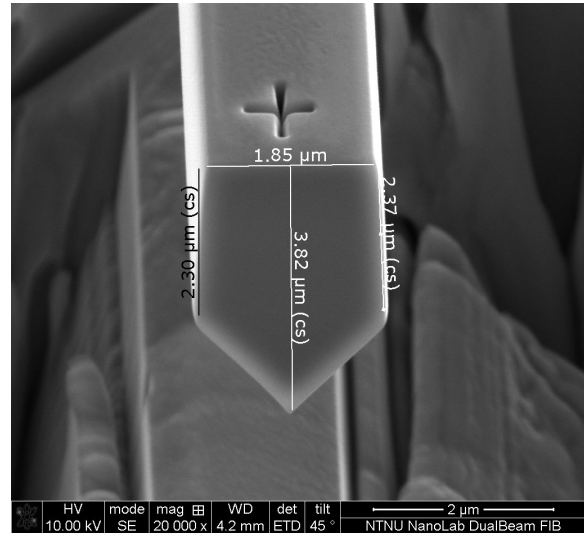
Figure 89: Cross-section
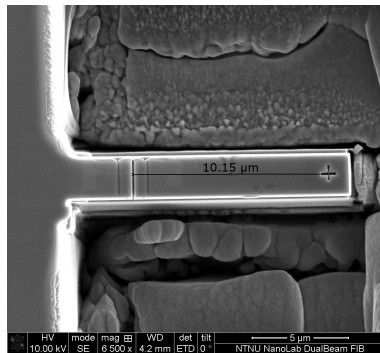
Figure 90: Top view
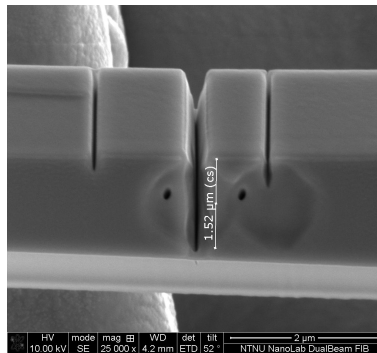

Figure 91: Crack, side 1
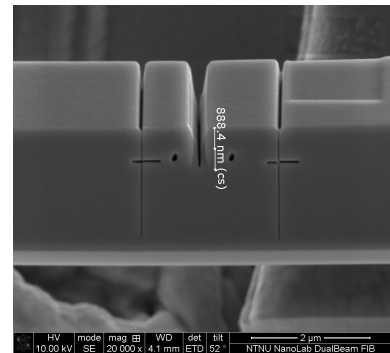

Figure 92: Crack, side 2
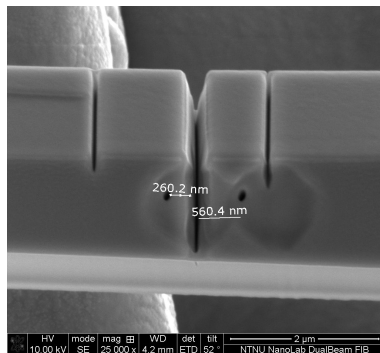
Figure 93: Side mark, side 1
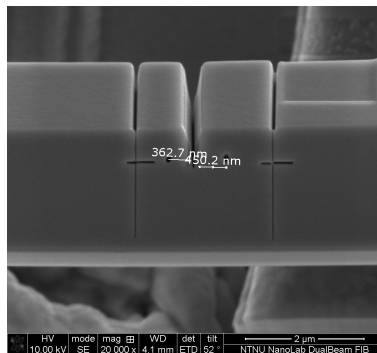
Figure 94: Side mark, side 2
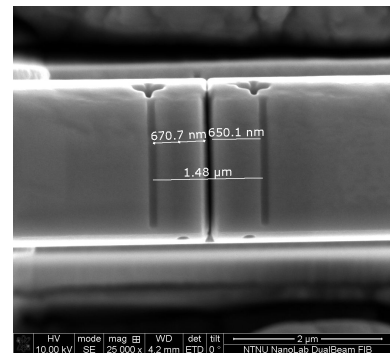
Figure 95: Top mark

Dimension	Value
Height	2,30 / 2,37 µm
Width	1,85 µm
Length	10,15 µm
Crack length, side 1	1,52 µm
Crack length, side 2	888,4 nm
Side mark, side 1	260,2 / 560,4 nm
Side mark, side 2	362,7 / 450,2 nm
Top mark	1,48 µm
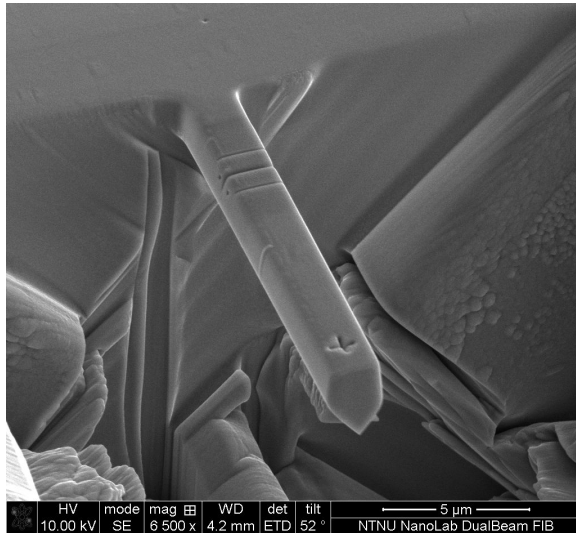
Figure 96: Beam 3
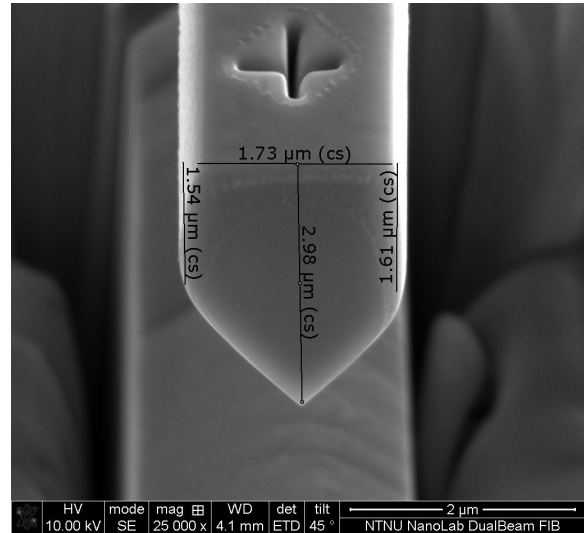
Figure 97: Cross-section
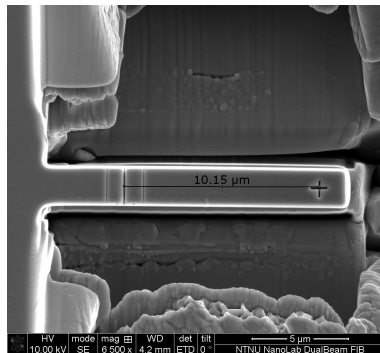
Figure 98: Top view
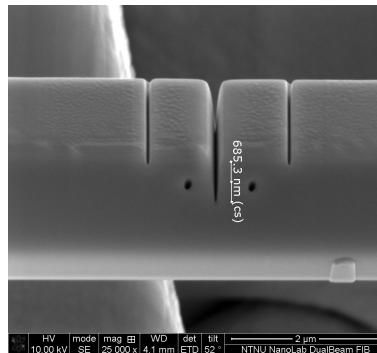
Figure 99: Crack, side 1
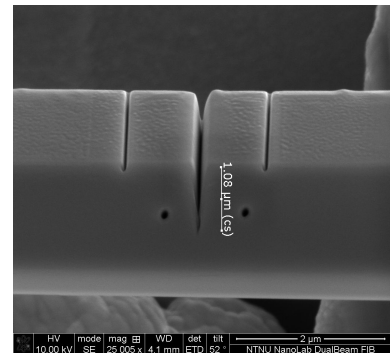
Figure 100: Crack, side 2
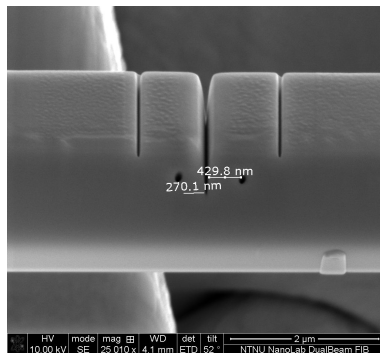
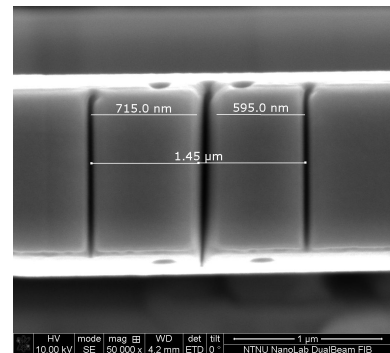Figure 101: Side mark, side 1
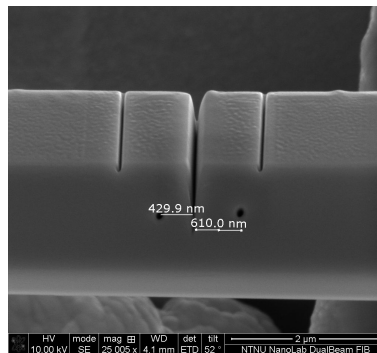
Figure 102: Side mark, side 2
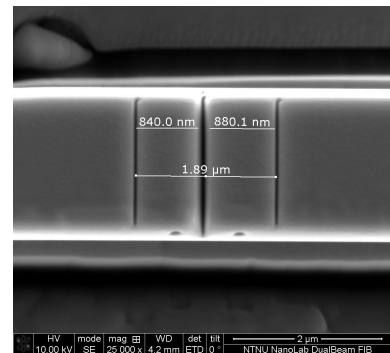
Figure 103: Top mark

Dimension	Value
Height	1,54 / 1,61 µm
Width	1,73 µm
Length	10,15 µm
Crack length, side 1	685,3 nm
Crack length, side 2	1,08 µm
Side mark, side 1	270,1 / 429,8 nm
Side mark, side 2	429,9 / 610,0 nm
Top mark	1,89 µm
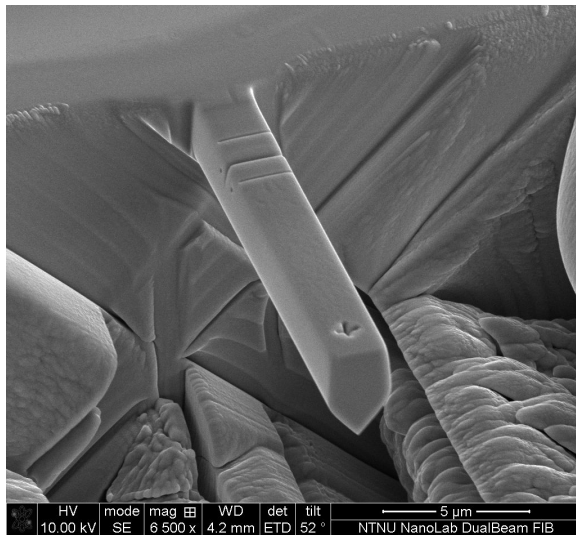
Figure 104: Beam 4
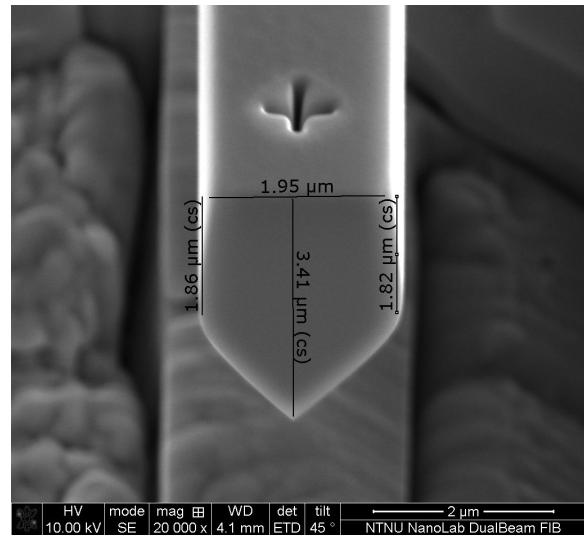
Figure 105: Cross-section
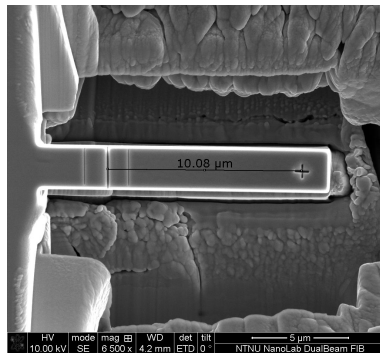
Figure 106: Top view
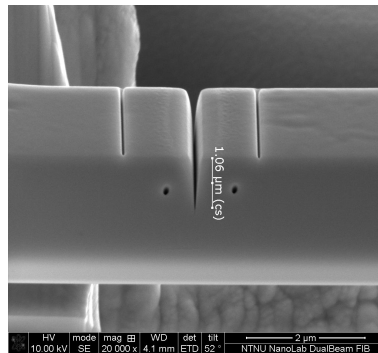
Figure 107: Crack, side 1
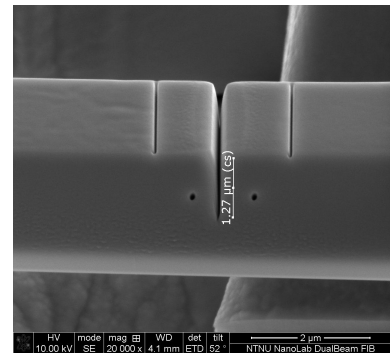
Figure 108: Crack, side 2
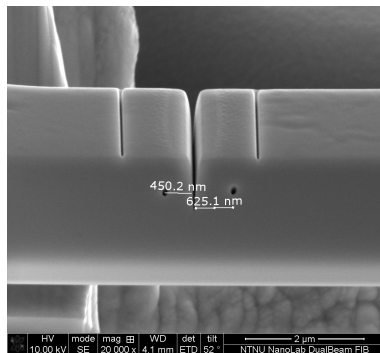
Figure 109: Side mark, side 1
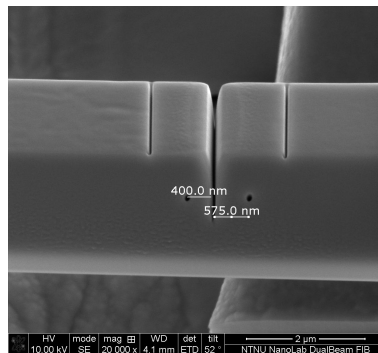
Figure 110: Side mark, side 2
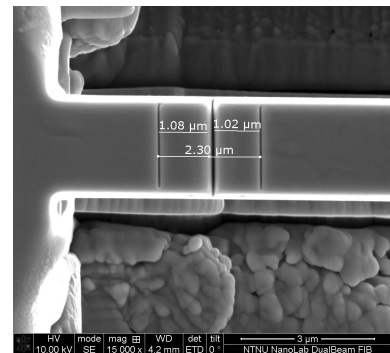
Figure 111: Top mark

Dimension	Value
Height	1,86 / 1, 82 μm
Width	1,95 μm
Length	10,08 μm
Crack length, side 1	1,06 μm
Crack length, side 2	1,27 μm
Side mark, side 1	450,2 / 625,1 nm
Side mark, side 2	400,0 / 575,0 nm
Top mark	2,30 μm
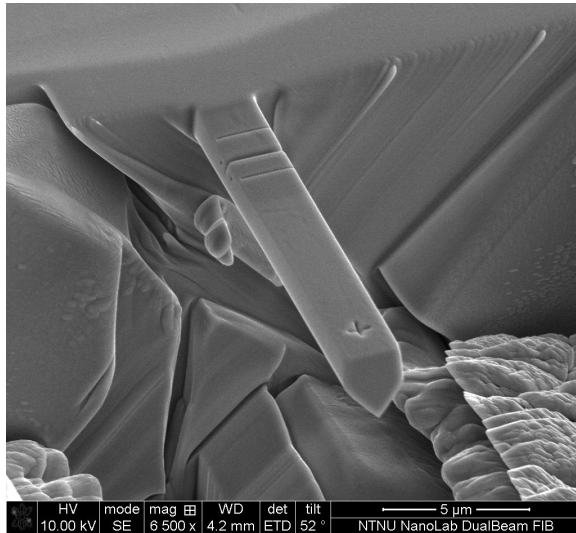
Figure 112: Beam 5
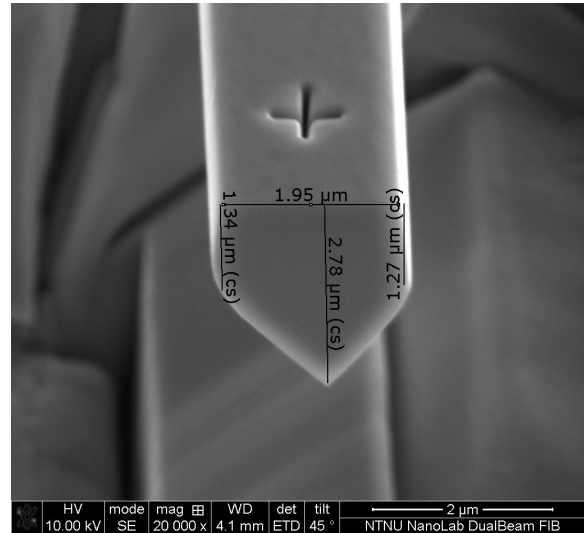
Figure 113: Cross-section
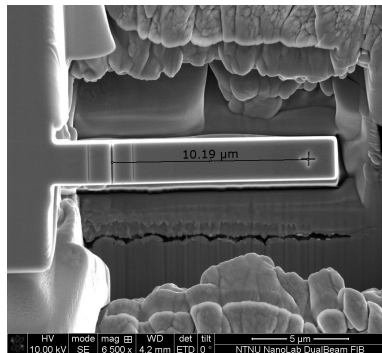
Figure 114: Top view
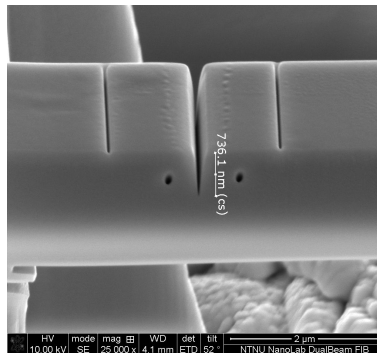
Figure 115: Crack, side 1
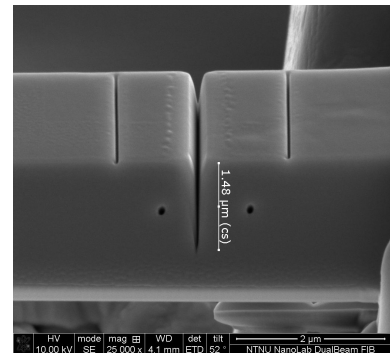
Figure 116: Crack, side 2
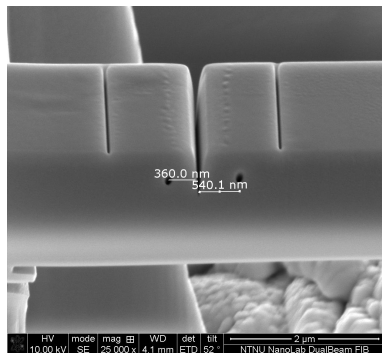
Figure 117: Side mark, side 1
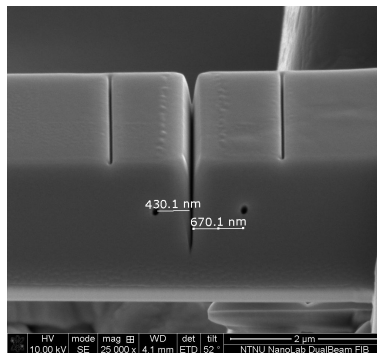
Figure 118: Side mark, side 2
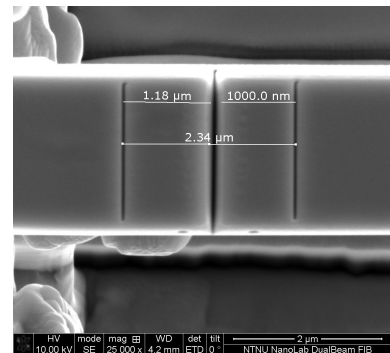
Figure 119: Top mark

Dimension	Value
Height	1,34 / 1,27 µm (at free end)
	2,09 / 1,63 µm (at crack position)
Width	1,95 µm
Length	10,19 µm
Crack length, side 1	736,1 nm
Crack length, side 2	1,48 µm
Side mark, side 1	360,0 / 540,1 nm
Side mark, side 2	430,1 / 670,1 nm
Top mark	2,34 µm
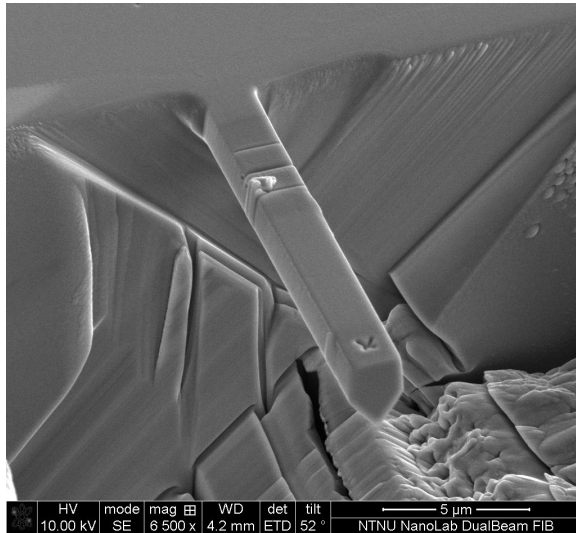
Figure 120: Beam 6
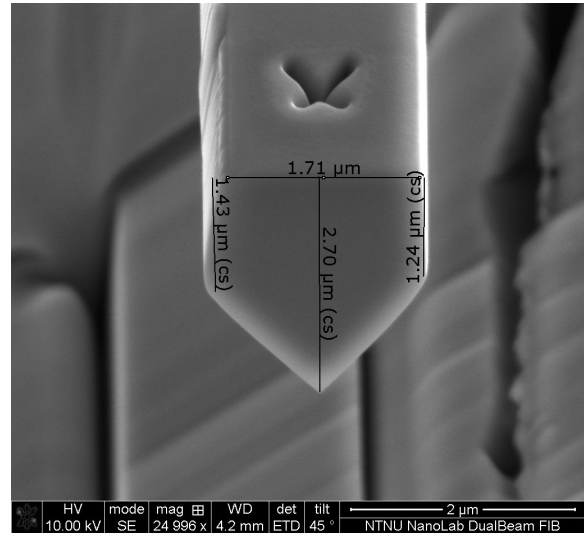
Figure 121: Cross-section
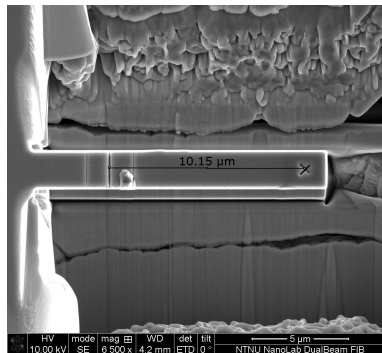
Figure 122: Top view
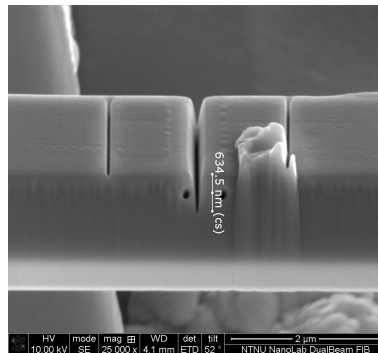
Figure 123: Crack, side 1
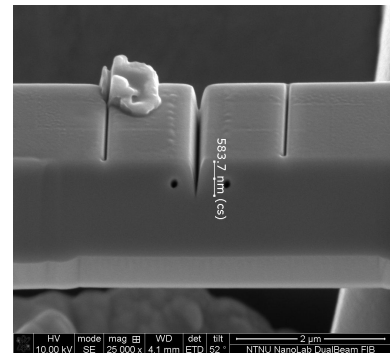
Figure 124: Crack, side 2

Figure 125: Side mark, side 1

Figure 126: Side mark, side 2

Figure 127: Top mark

Dimension	Value
Height	1,43 / 1,24 μm
Width	1,71 μm
Length	10,15 μm
Crack length, side 1	634,5 nm
Crack length, side 2	583,7 nm
Side mark, side 1	90,0 / 330,2 nm
Side mark, side 2	230,0 / 400,1 nm
Top mark	2,44 μm

Figure 128: Beam 7

Figure 129: Cross-section

Figure 130: Top view

Figure 131: Crack, side 1

Figure 132: Crack, side 2

Figure 133: Side mark, side 1

Figure 134: Side mark, side 2

Figure 135: Top mark

Dimension	Value
Height	1,23 / 1,21 μm
Width	1,26 μm
Length	10,23 μm
Crack length, side 1	716,1 nm
Crack length, side 2	951,9 nm
Side mark, side 1	247,9 / 421,4 nm
Side mark, side 2	207,1 / 442,9 nm
Top mark	1,96 μm

Figure 136: Beam 8

Figure 137: Cross-section

Figure 138: Top view

Figure 139: Crack, side 1

Figure 140: Crack, side 2
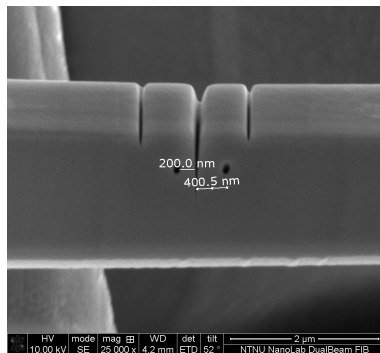
Figure 141: Side mark, side 1
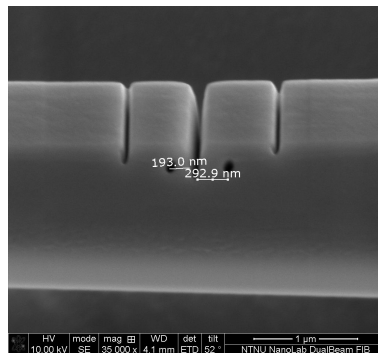
Figure 142: Side mark, side 2

Figure 143: Top mark

Dimension	Value
Height	1,73 µm / 636,5 nm
Width	1,13 µm
Length	10,04 µm
Crack length, side 1	964,5 nm
Crack length, side 2	371,7 nm
Side mark, side 1	200,0 / 400,5 nm
Side mark, side 2	193,0 / 292,9 nm
Top mark	1,45 µm

Appendix B: Additional drift correction graphs
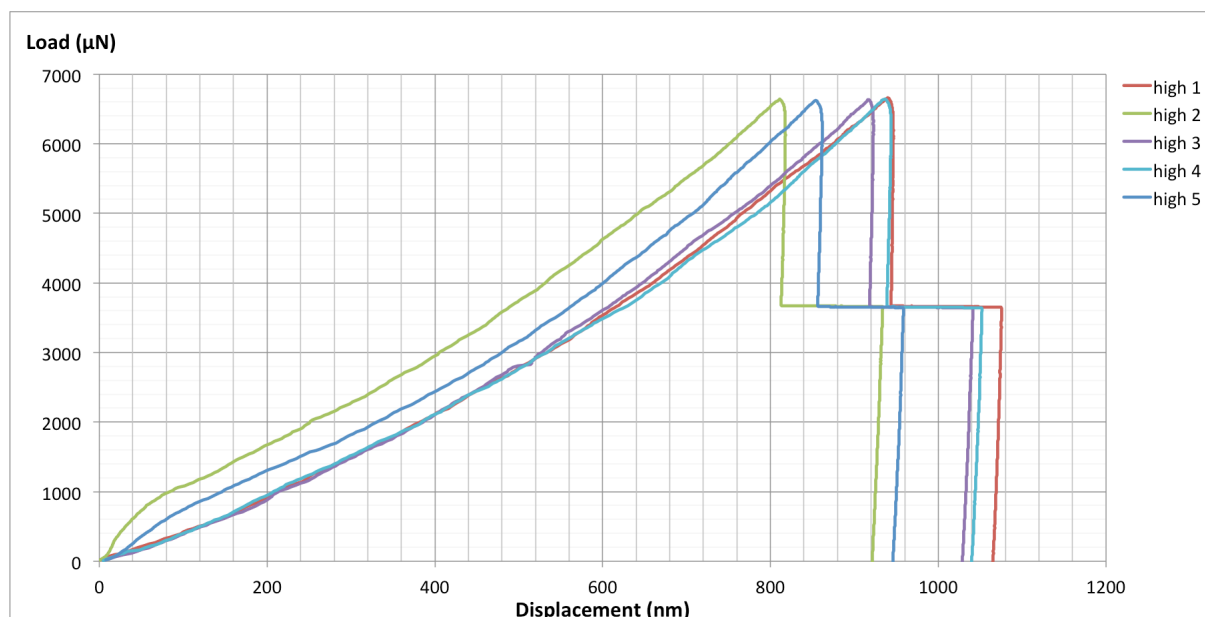
Figure 144: Load vs displacement at room temperature (29°C), with no drift correction
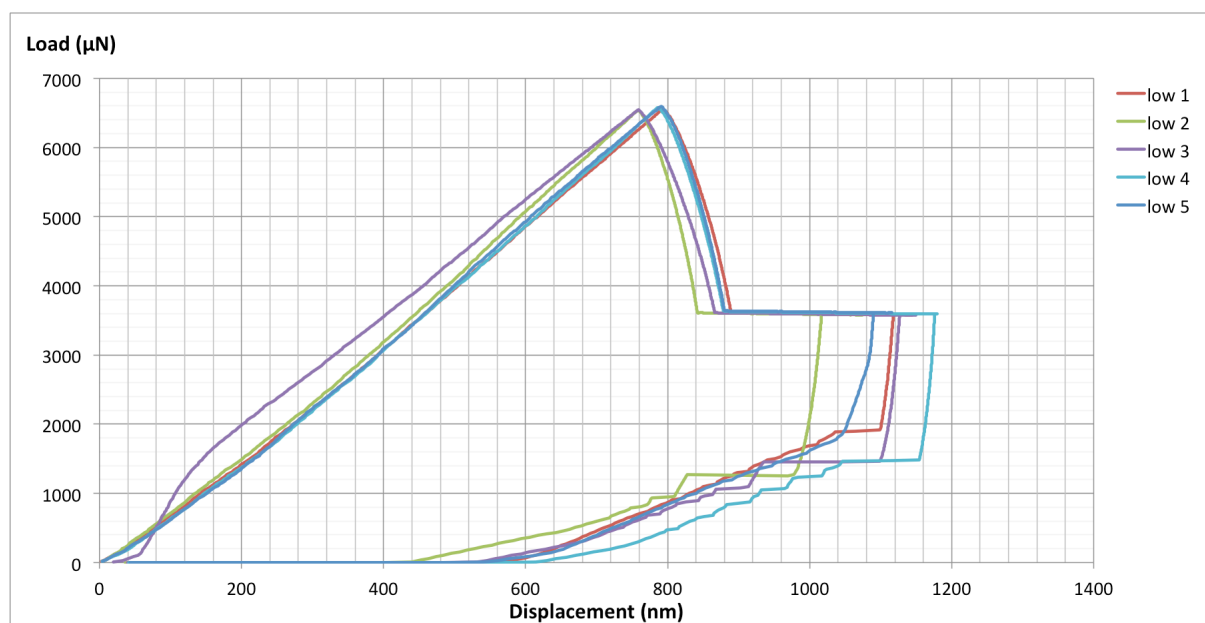
Figure 145: Load vs displacement at low temperature (-88°C), with no drift correction
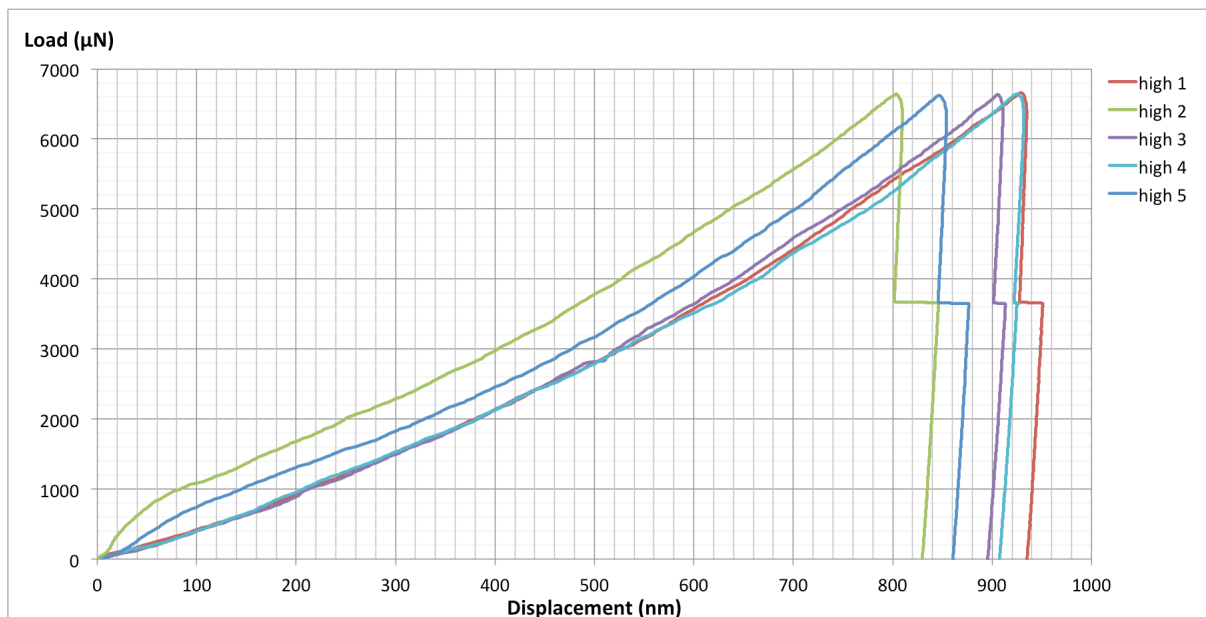
Figure 146: Load vs displacement at room temperature (29°C), with automated drift correction
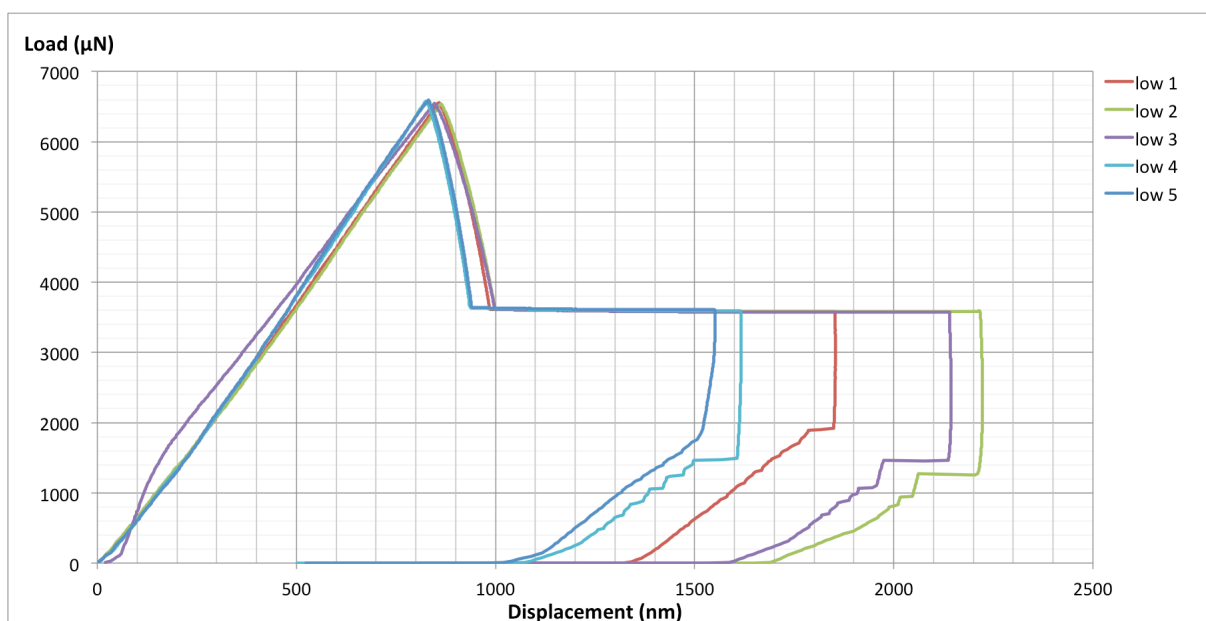
Figure 147: Load vs displacement at low temperature (-88°C), with automated drift correction
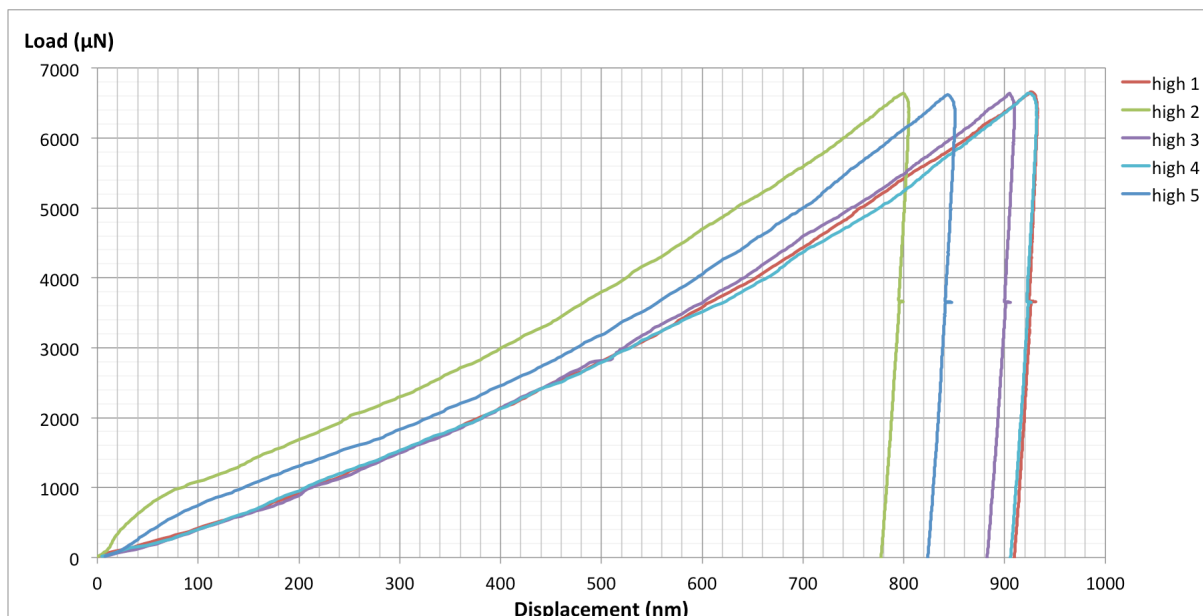
Figure 148: Load vs displacement at room temperature (29°C), with manual drift correction
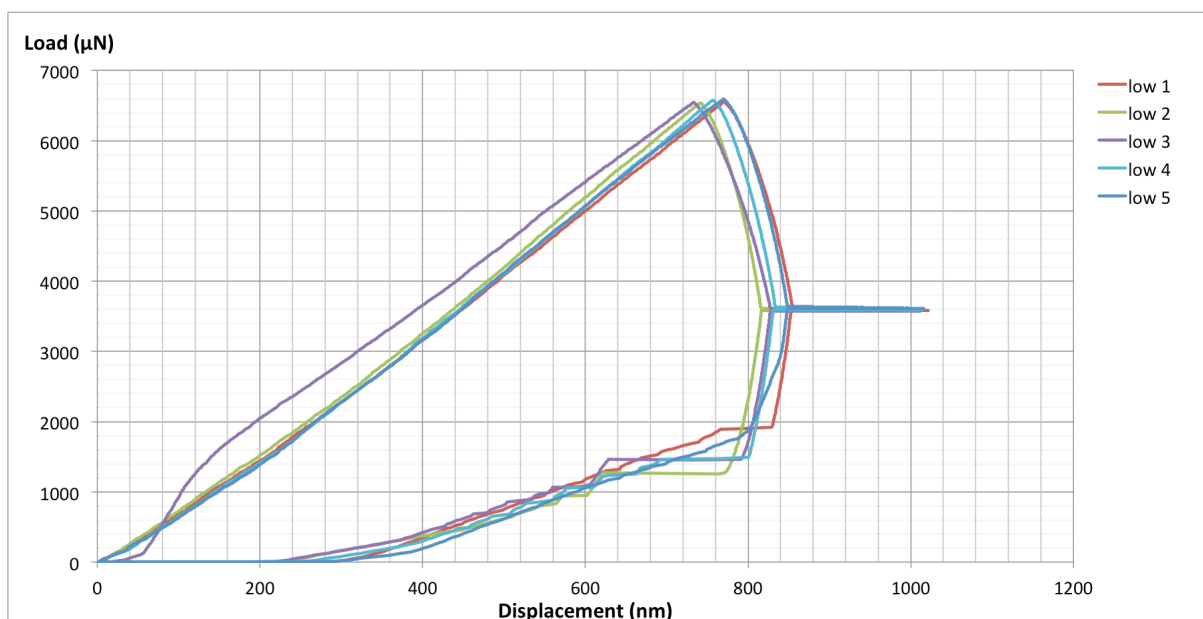
Figure 149: Load vs displacement at low temperature (-88°C), with manual drift correction

78
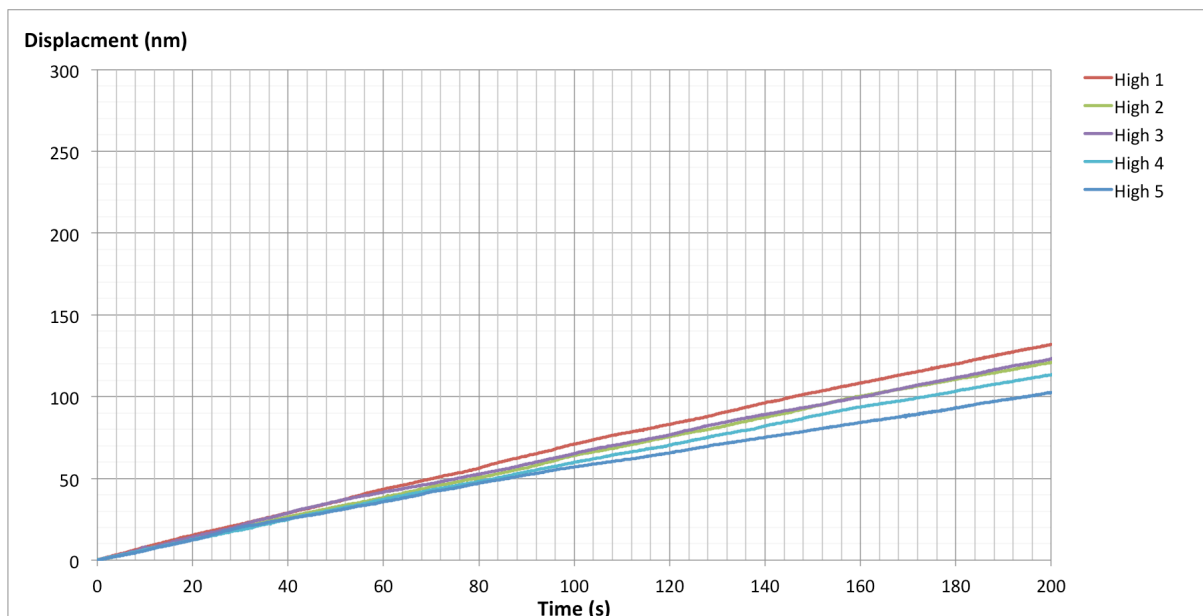
Figure 150: Displacement vs time at room temperature (29°C)
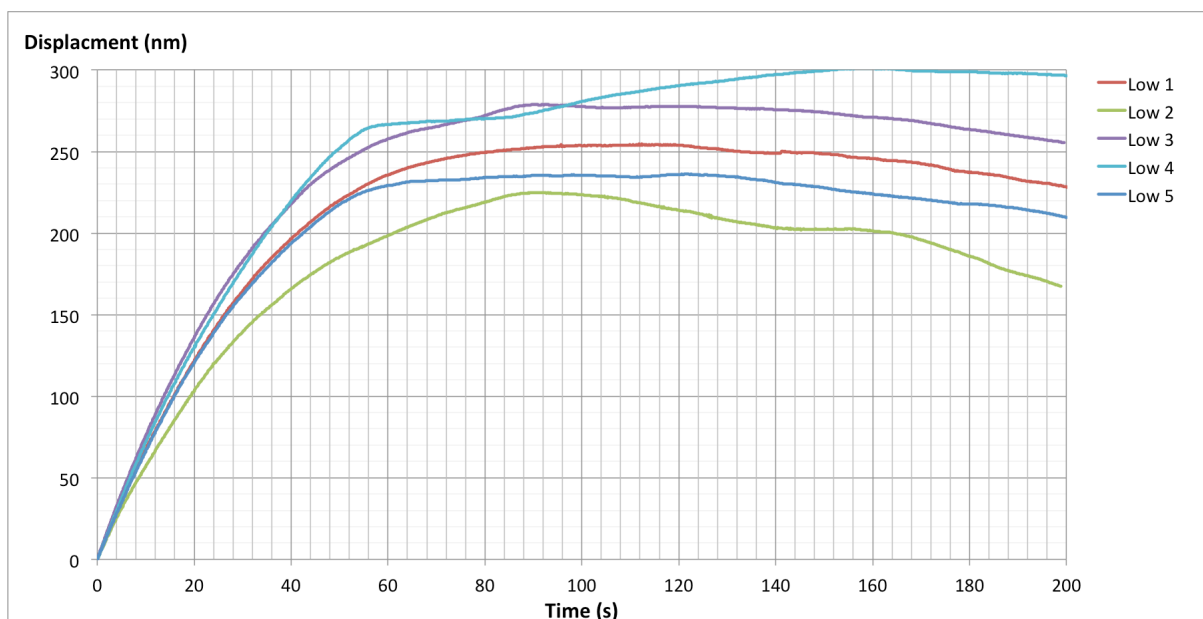
Figure 151: Displacement vs time at low temperature (-88°C)

Appendix C: Individual load displacement curves
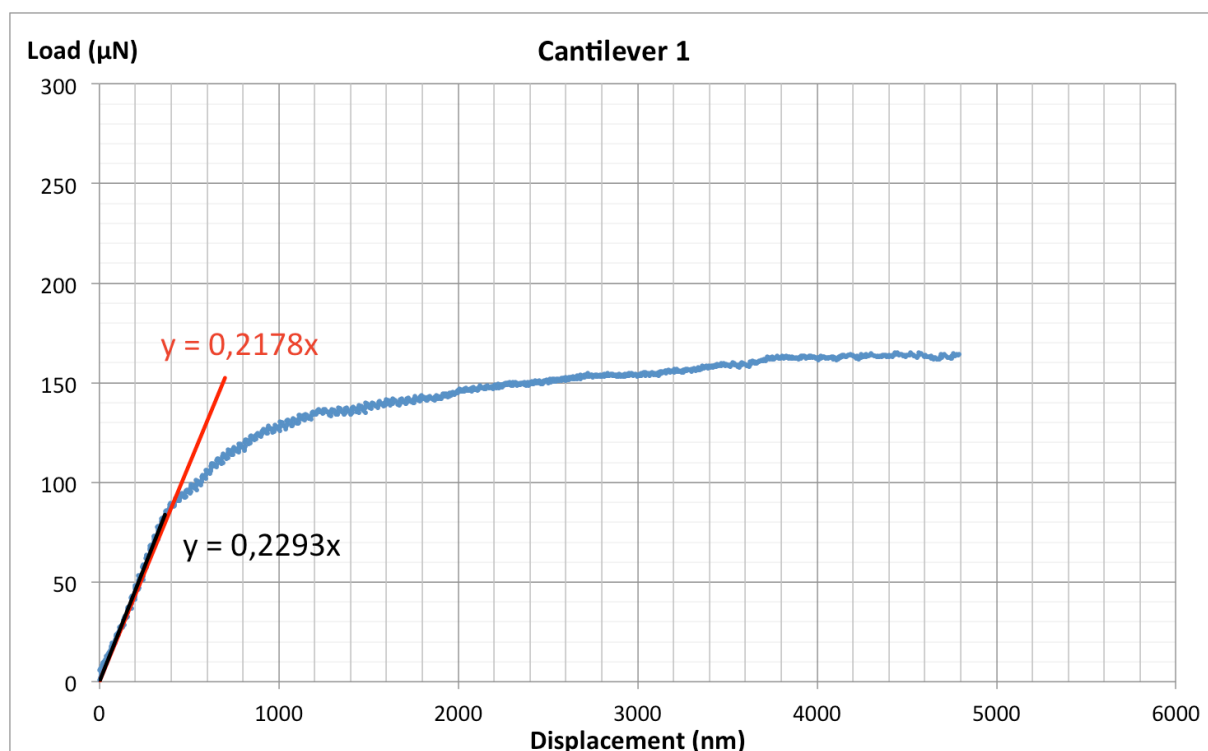
Figure 152: Load displacement for cantilever 1, temperature 29°C
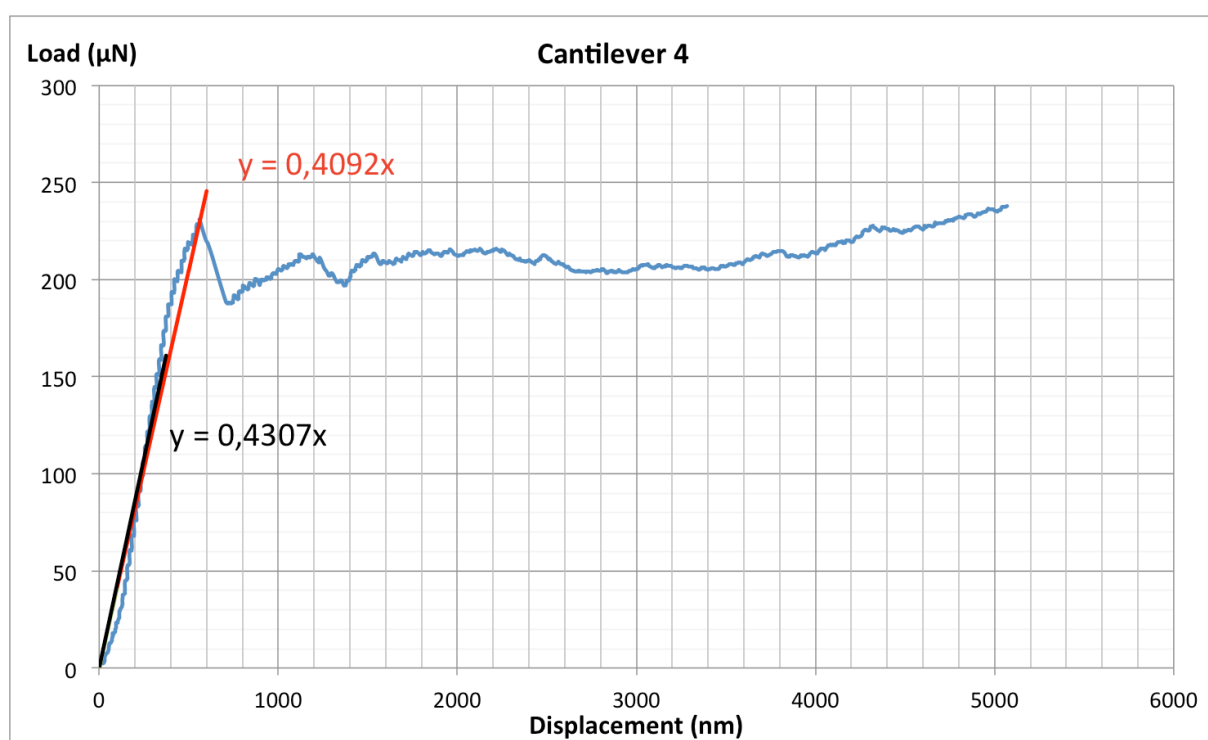
Figure 153: Load displacement for cantilever 4, temperature 29°C
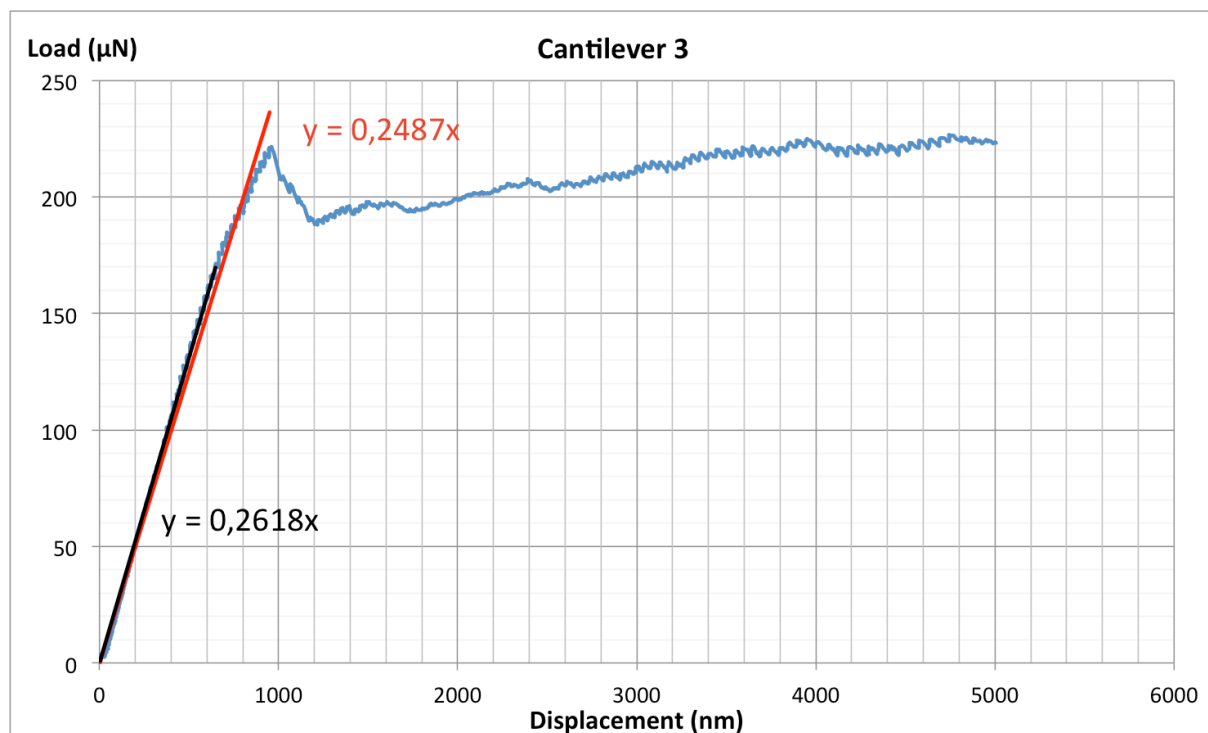
Figure 154: Load displacement for cantilever 3, temperature -70°C
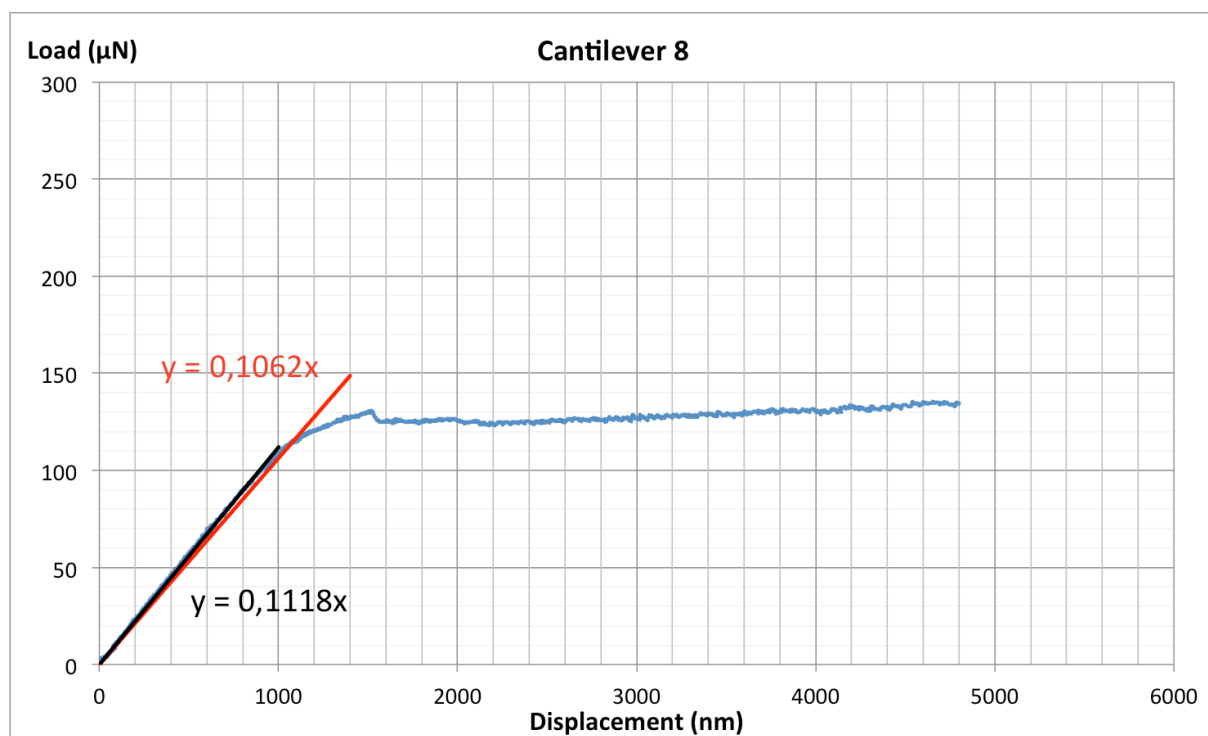
Figure 155: Load displacement for cantilever 8, temperature -78°C
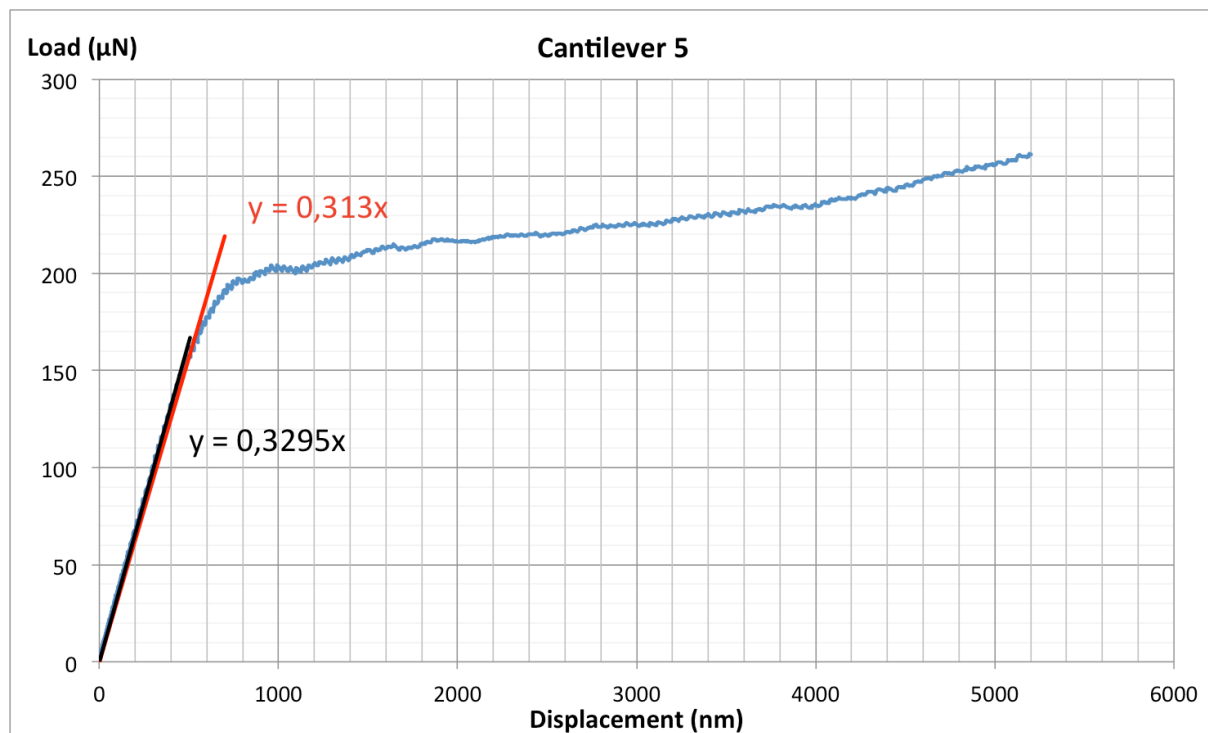
Figure 156: Load displacement for cantilever 5, temperature -88°C
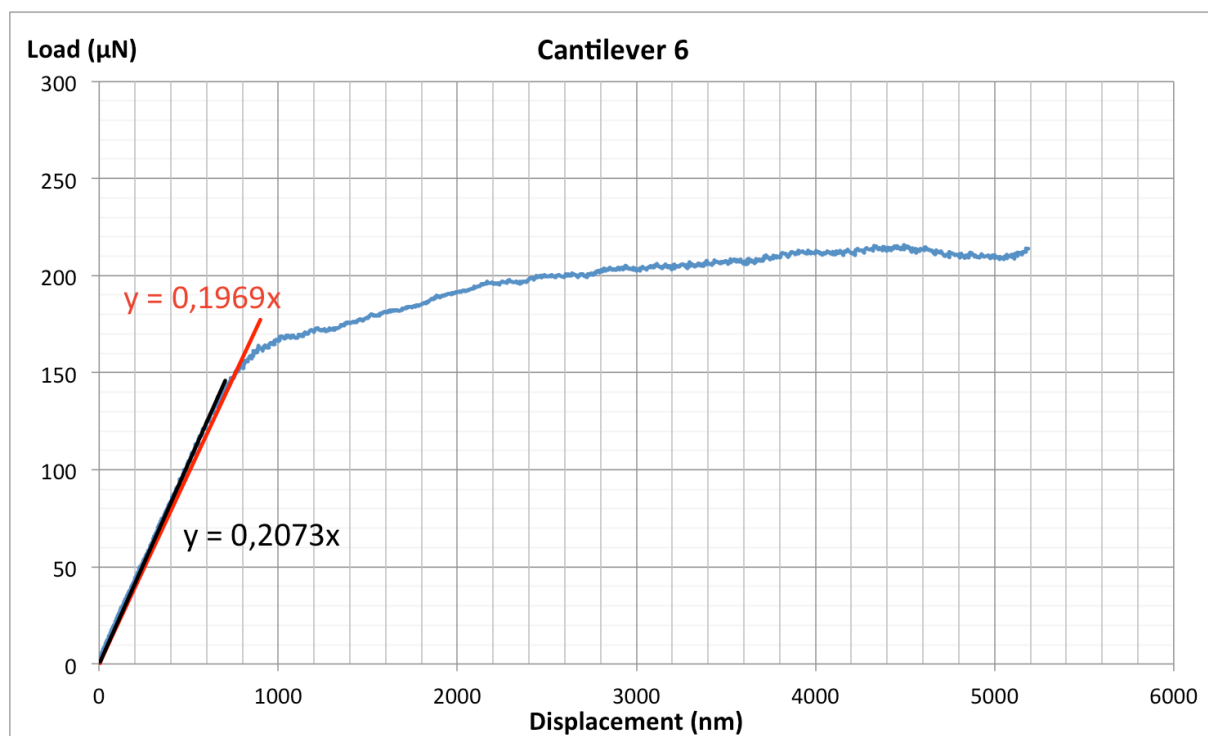
Figure 157: Load displacement for cantilever 6, temperature -88°C
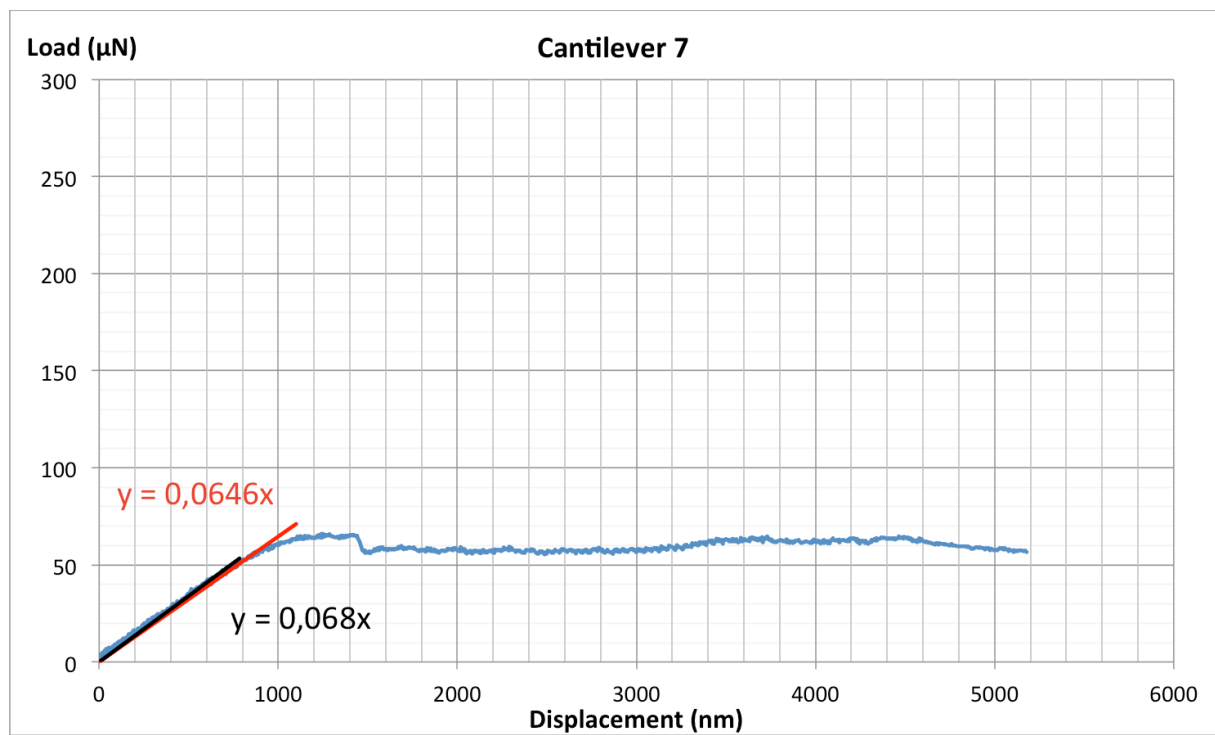
Figure 158: Load displacement for cantilever 7, temperature -88°C
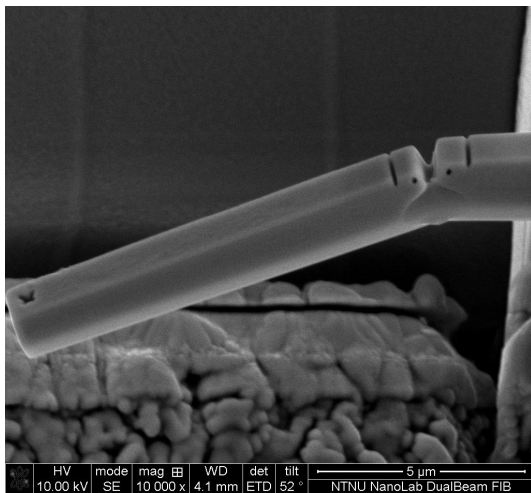
Appendix D: Cantilevers after loading
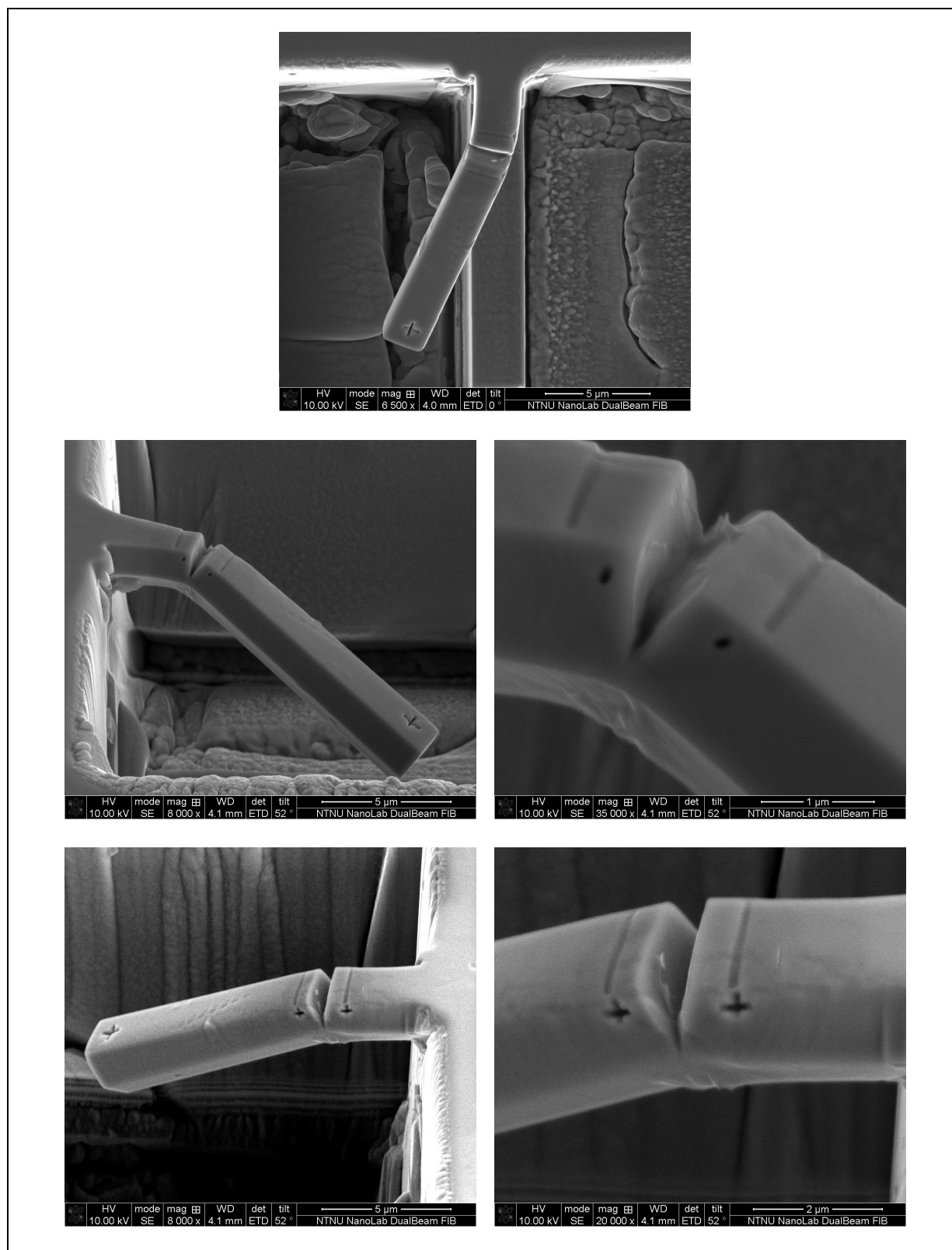
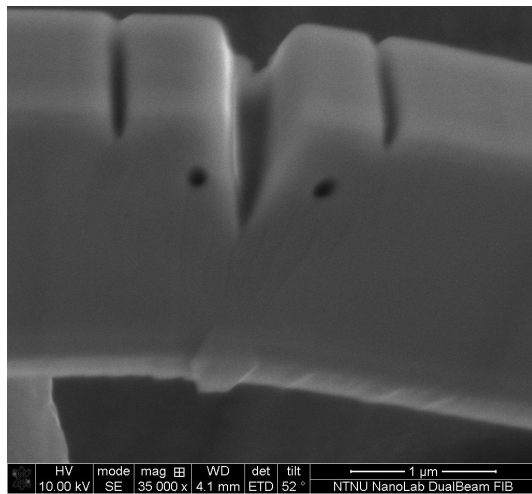Figure 159: Beam 1 after loading
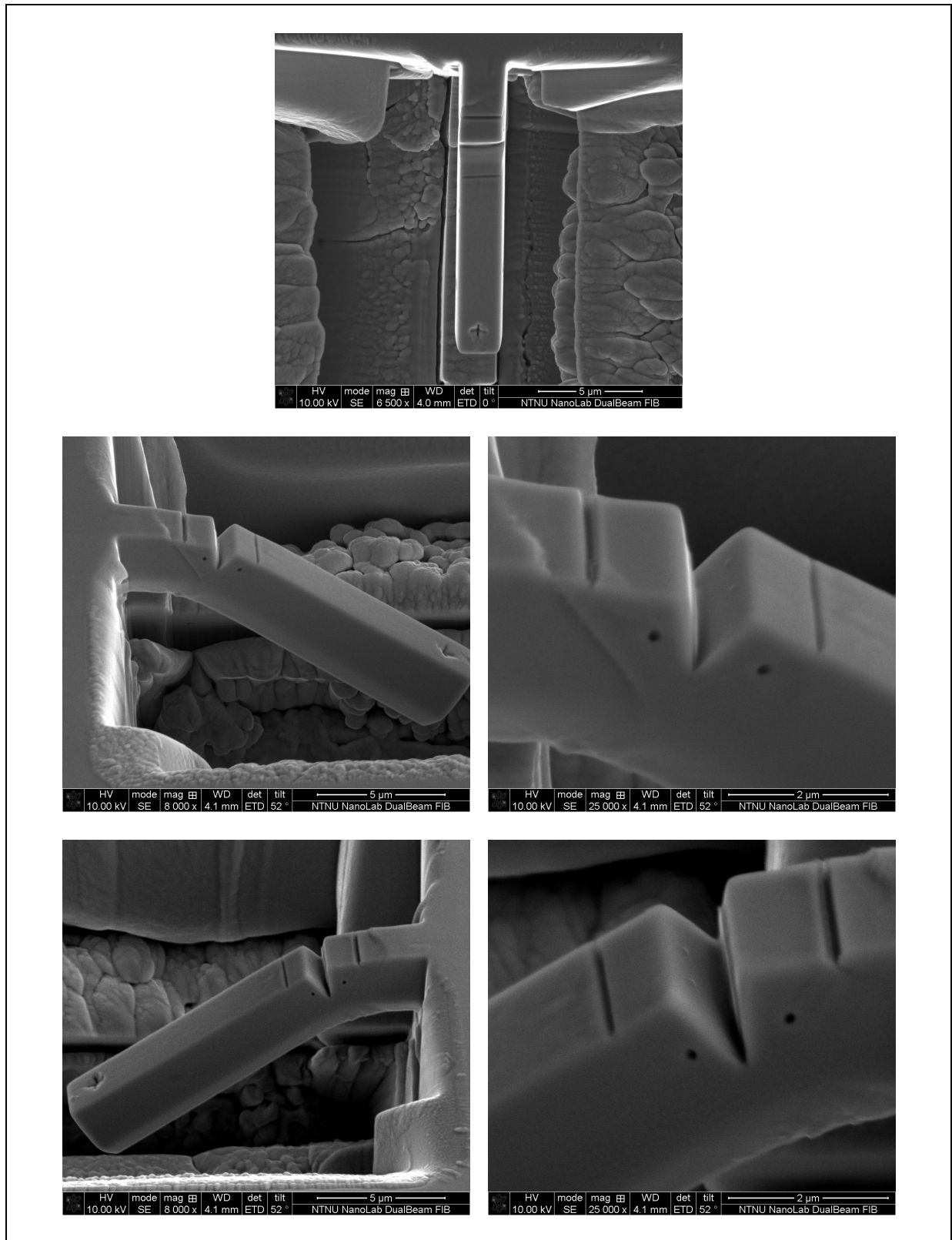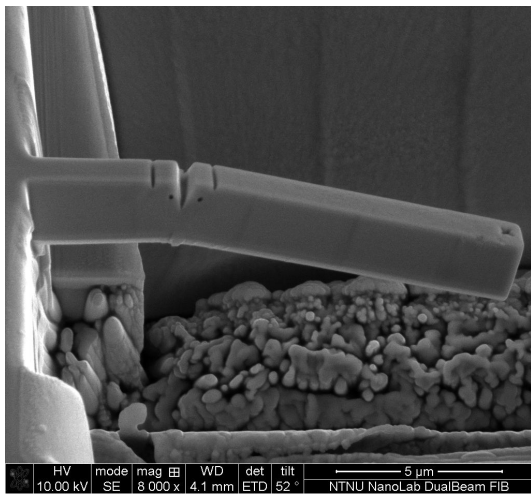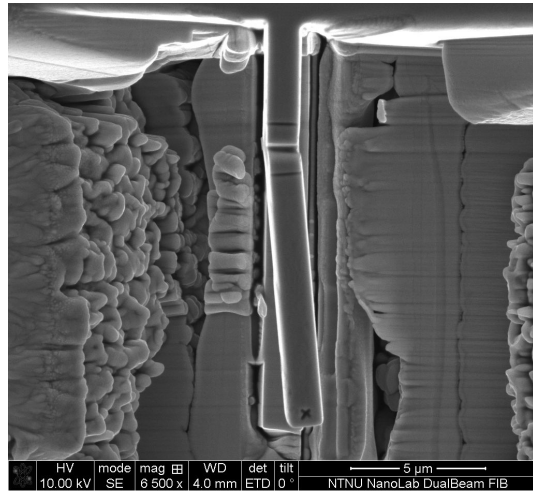
Figure 160: Beam 4 after loading
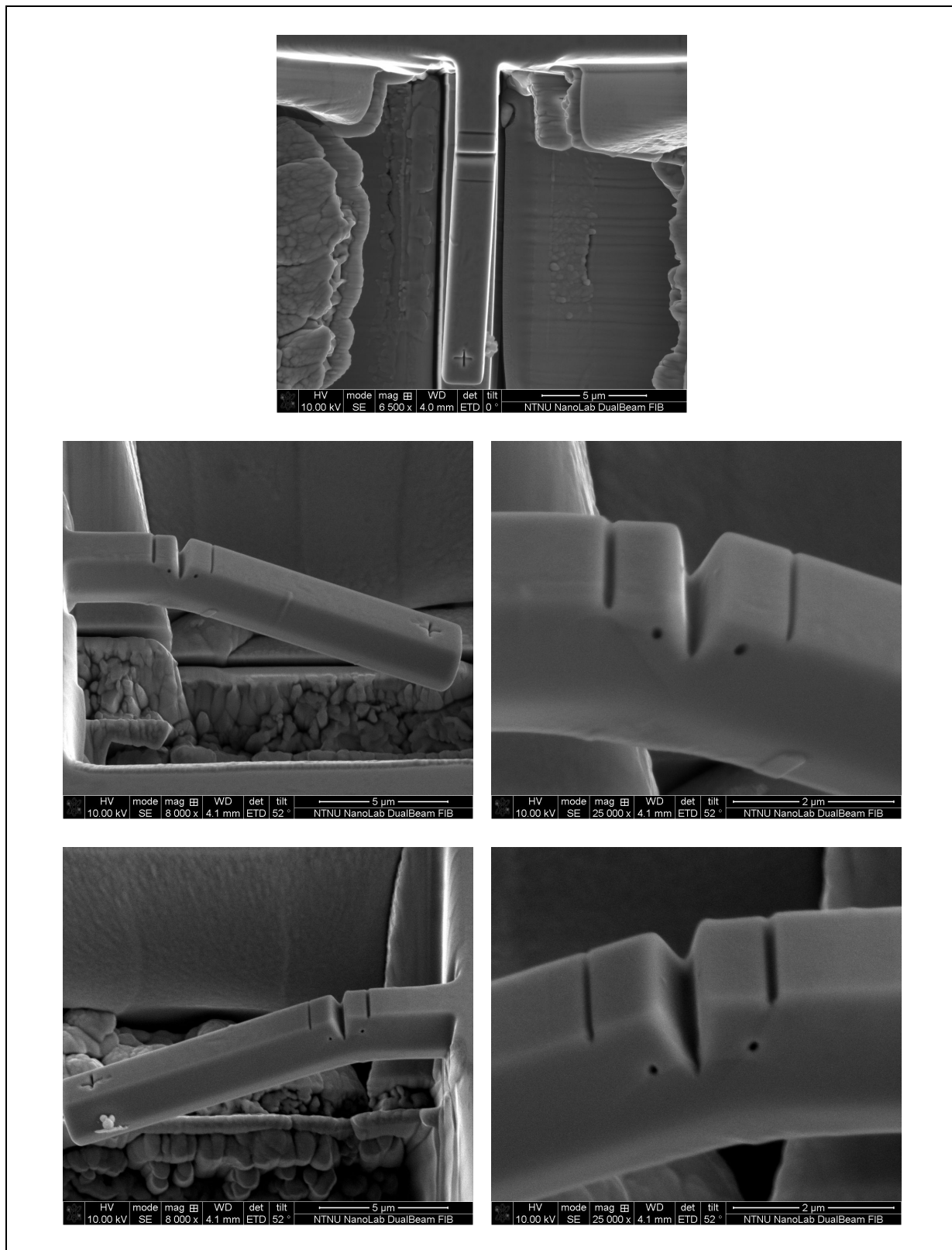
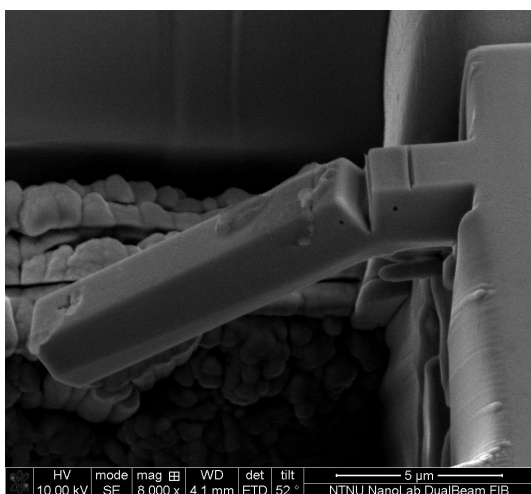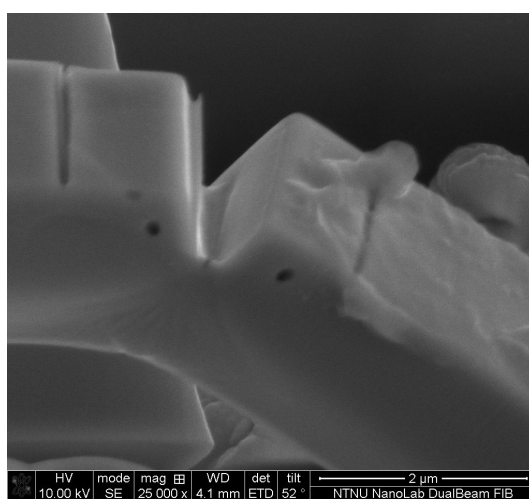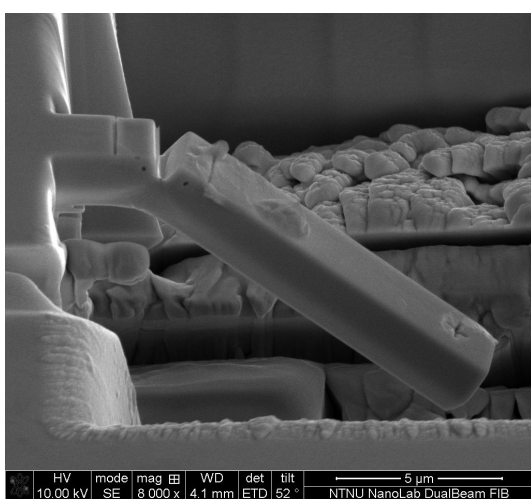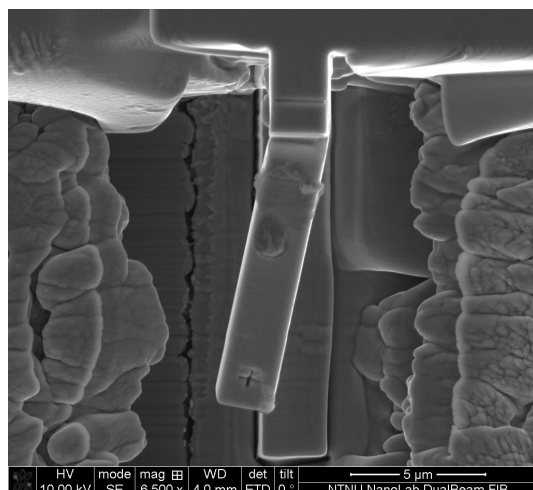Figure 161: Beam 3 after loading
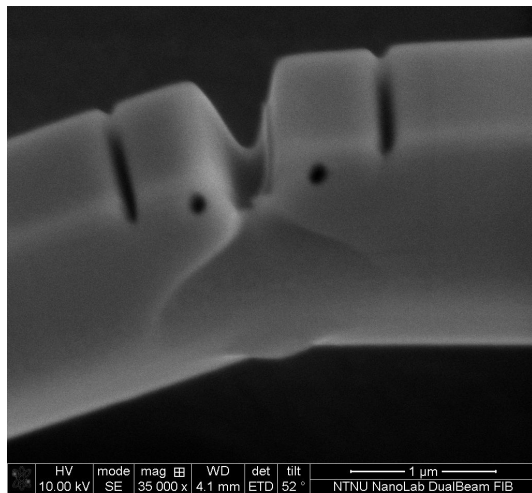
Figure 162: Beam 8 after loading
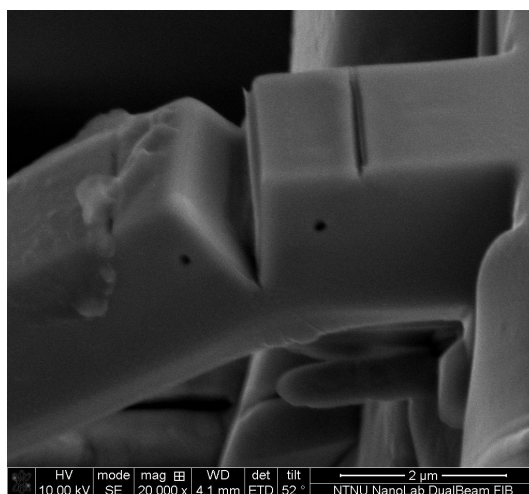
Figure 163: Beam 5 after loading
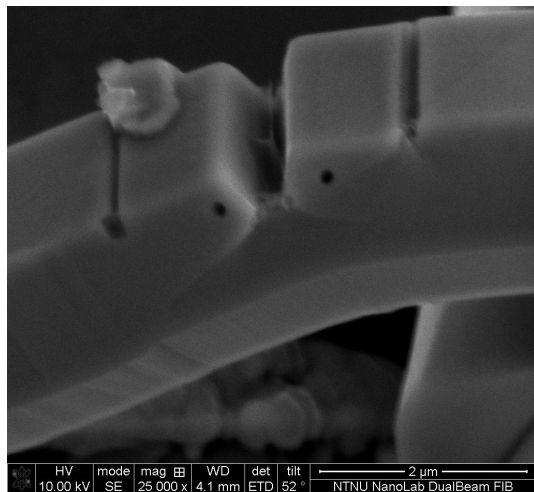
Figure 164: Beam 6 after loading
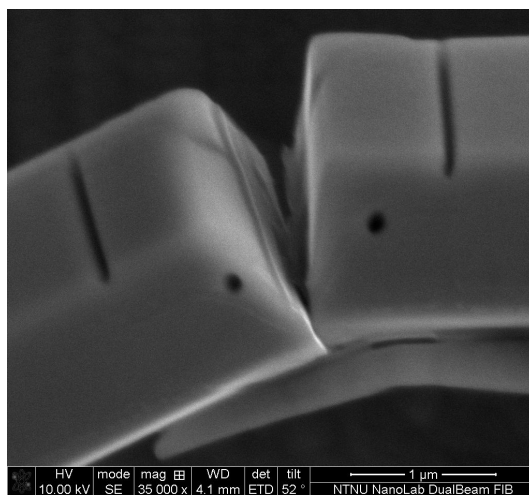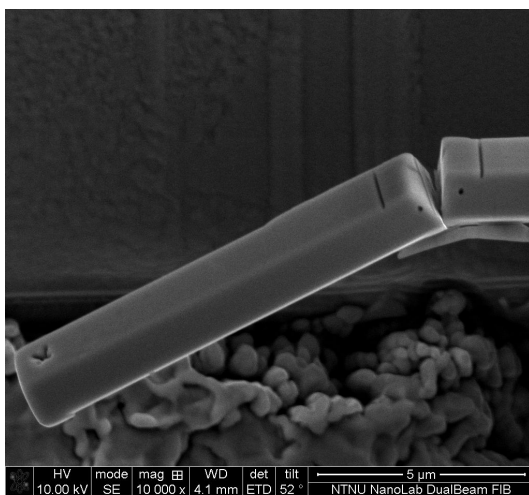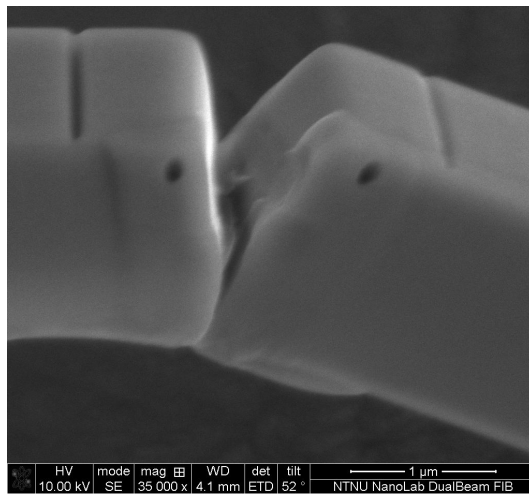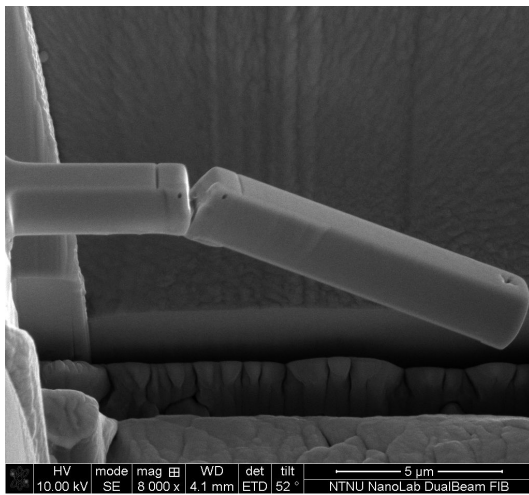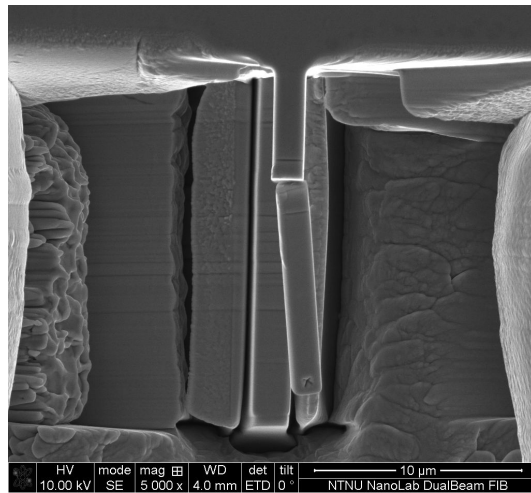
Figure 165: Beam 7 after loading

Appendix E: Calculation details

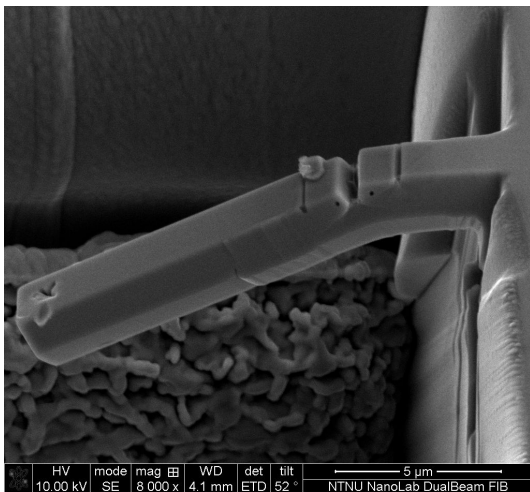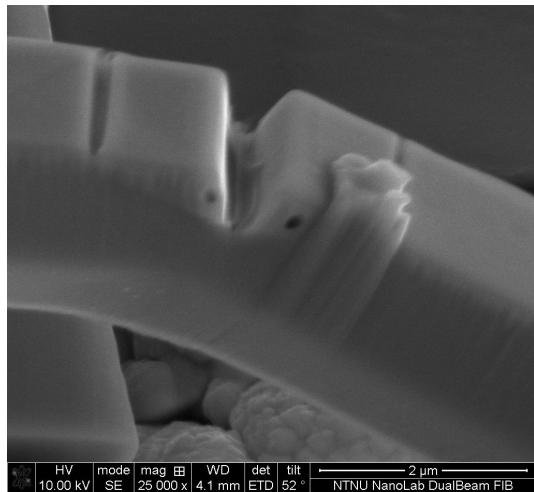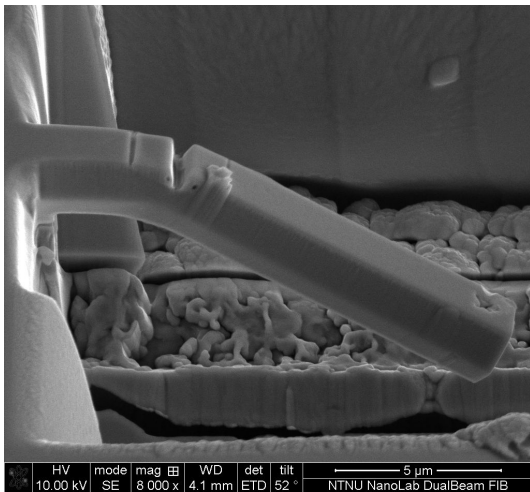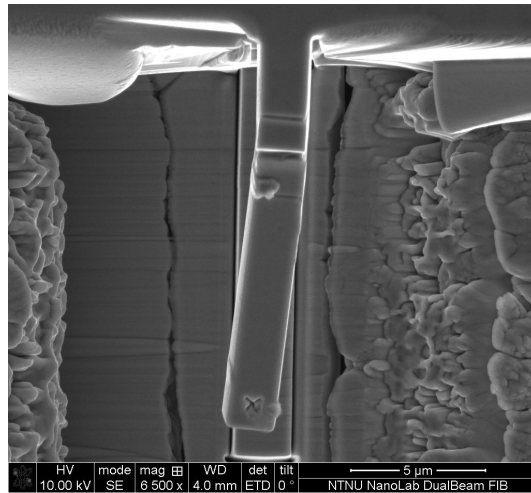|	Temp [°C]	Force[0] [µN]	Height [µm]	Width [µm]	Length [µm]	Crack length [µm]	Method 1[1] [MPa√m]	Method 2[1] [MPa√m]	Method 3[3] [MPa√m]	Method 4[4] [MPa√m]	Method 5[5] [MPa√m]
Cantilever 1	29	91,8600	1,7450	1,9100	9,4200	1,2250	3,4935	4,1789	4,7712	18,4703	4,6176
Cantilever 4	29	230,8300	1,8400	1,9500	10,0800	1,1650	6,4594	8,1282	8,9081	34,2666	8,5667
Cantilever 3	-70	221,1800	1,5750	1,7300	10,1500	0,8827	6,3176	8,8528	9,4939	37,5163	9,3791
Cantilever 8	-78	115,1500	1,1833	1,1300	10,0400	0,6681	7,2438	10,8588	11,6531	45,9517	11,4879
Cantilever 5	-88	173,3200	1,8600	1,9500	10,1900	1,1081	4,1949	5,3833	5,8186	22,6290	5,6572
Cantilever 6	-88	152,4300	1,3350	1,7100	10,1500	0,6091	3,6636	5,7834	6,2002	26,1553	6,5388
Cantilever 7	-88	54,5400	1,2200	1,2600	10,2300	0,8340	4,7903	6,5810	7,4178	28,5398	7,1349

0) Force from

1) Calculated with equations:

$$K_{IC} = \sigma_f \sqrt{\pi a}\, f\left(\frac{a}{h}\right) \qquad f\left(\frac{a}{h}\right) = 1.122 - 1.121\left(\frac{a}{h}\right) + 3.74\left(\frac{a}{h}\right)^2 + 3.873\left(\frac{a}{h}\right)^3 - 19.05\left(\frac{a}{h}\right)^4 + 22.55\left(\frac{a}{h}\right)^5$$

$$\sigma_f = \frac{FLy}{I} \qquad I = \frac{wh^3}{12} + \left(y - \frac{h}{2}\right)^2 hw + \frac{w^4}{288} + \frac{w^2}{4}\left[\frac{h}{6} + (h - y)\right]^2 \qquad y = \frac{\frac{h^2 w}{2} + \frac{w^2}{4}\left(h + \frac{w}{6}\right)}{hw + \frac{w^2}{4}}$$

2) Calculated with equations:

$$K_{IC} = \frac{F_{max}L}{wh^{3/2}}\, f\left(\frac{a}{h}\right) \qquad f\left(\frac{a}{h}\right) = 1,46 + 24,36\left(\frac{a}{h}\right) - 47,21\left(\frac{a}{h}\right)^2 + 75,18\left(\frac{a}{h}\right)^3$$

3) Calculated with equations

$$K_{IC} = \sigma_f \sqrt{\pi a}\, f\left(\frac{a}{h}\right) \qquad f\left(\frac{a}{h}\right) = 1,22 - 1,40\left(\frac{a}{h}\right) + 7,33\left(\frac{a}{h}\right)^2 - 13,08\left(\frac{a}{h}\right)^3 + 14,0\left(\frac{a}{h}\right)^4 \qquad \sigma = 6\frac{FL}{wh^2}$$

4) Calculated with equations

$$K = \frac{4FL}{wh^{3/2}}\, f\left(\frac{a}{h}\right) \qquad f\left(\frac{a}{h}\right) = 4\,\frac{3\left(\frac{a}{h}\right)^{0,5}\left(1,23 - \left(\frac{a}{h}\right)\left(1 - \left(\frac{a}{h}\right)\right)\right)\left(-6,09 + 13,96\left(\frac{a}{h}\right) - 14,05\left(\frac{a}{h}\right)^2\right)}{2\left(1 + 2\left(\frac{a}{h}\right)\right)\left(1 - \left(\frac{a}{h}\right)\right)^{1,5}}$$

5) Calculated with equations

$$K_{IC} = \frac{F_{max}L}{wh^{3/2}}\, f\left(\frac{a}{h}\right) \qquad f\left(\frac{a}{h}\right) = 4\,\frac{3\left(\frac{a}{h}\right)^{0,5}\left(1,23 - \left(\frac{a}{h}\right)\left(1 - \left(\frac{a}{h}\right)\right)\right)\left(-6,09 + 13,96\left(\frac{a}{h}\right) - 14,05\left(\frac{a}{h}\right)^2\right)}{2\left(1 + 2\left(\frac{a}{h}\right)\right)\left(1 - \left(\frac{a}{h}\right)\right)^{1,5}}$$

	Temp [°C]	Top mark (before loading) [μm]	Top mark (after loading) [μm]	CMOD₁ [μm]	Side mark (before loading) [μm]	Side mark (after loading) [μm]	CMOD₂ [μm]	Height between CMOD₁ and CMOD₂	b[1] [μm]	Rotational point[2] [μm]	Crack length (measuring side) [μm]	D[3] [μm]	CTOD[4] [μm]	Crack length (average) [μm]	D[5] [μm]	CTOD[4] [μm]
Cantilever 1	29	1,5692	1,7538	0,1846	0,7705	0,8923	0,1218	0,3727	0,0314	1,0955	1,0200	0,0755	0,0127	1,2250	-0,1295	-0,0218
Cantilever 4	29	2,3000	2,5231	0,2231	1,0753	1,2000	0,1247	0,6033	0,0492	1,3678	1,0600	0,3078	0,0502	1,1650	0,2028	0,0331
Cantilever 3	-70	1,8900	2,2500	0,3600	0,6999	0,9205	0,2206	0,5221	0,0697	1,3483	0,6853	0,6630	0,1770	0,8827	0,4657	0,1243
Cantilever 8	-78	1,4500	1,7037	0,2537	0,6005	0,7407	0,1402	0,4930	0,0568	1,1020	0,9645	0,1375	0,0316	0,6681	0,4339	0,0999
Cantilever 5	-88	2,3400	2,5761	0,2361	0,9001	1,0435	0,1434	0,4576	0,0464	1,1655	0,7361	0,4294	0,0870	1,1081	0,0574	0,0116
Cantilever 6	-88	2,4400	2,7273	0,2873	0,4202	0,6477	0,2275	0,2663	0,0299	1,2794	0,6345	0,6449	0,1448	0,6091	0,6703	0,1505
Cantilever 7	-88	1,9600	2,2222	0,2622	0,6693	0,8444	0,1751	0,3740	0,04355	1,1259	0,7161	0,4098	0,0954	0,8340	0,2919	0,0680

1) Calculated from equations: $b = \frac{CMOD_1}{2} - \frac{CMOD_2}{2}$

2) Calculated from equations: $\tan\theta = \frac{b}{h}$ and $r_p = \tan\theta \cdot \frac{1}{2} CMOD_1$

3) Distance from rotational point to crack tip (measuring side), i.e. measuring point for CTOD

4) Calculated form equation: $CTOD = CMOD_1 \frac{d}{a}$

5) Distance from rotational point to crack tip (average), i.e. measuring point for CTOD

	Temp [°C]	Top mark (before loading) [µm]	Top mark (after loading) [µm]	$CMOD_1$ [µm]	Height [µm]	Width [µm]	Crack length [µm]	r_p	CTOD[2] [µm]	Cross-section area [µm²]	New Height[1] [µm]	CTOD[2] [µm]
Cantilever 1	29	1,5692	1,7538	0,1846	1,7450	1,9100	1,2250	0,4400	0,0291	4,5983	2,4075	0,0550
Cantilever 4	29	2,3000	2,5231	0,2231	1,8400	1,9500	1,1650	0,4400	0,0453	5,1188	2,6250	0,0793
Cantilever 3	-70	1,8900	2,2500	0,3600	1,5750	1,7300	0,8827	0,4400	0,0924	3,9401	2,2775	0,1477
Cantilever 8	-78	1,4500	1,7037	0,2537	1,1833	1,1300	0,6681	0,4400	0,0643	1,9059	1,6866	0,1019
Cantilever 5	-88	2,3400	2,5761	0,2361	1,8600	1,9500	1,1081	0,4400	0,0543	4,5240	2,3200	0,0767
Cantilever 6	-88	2,4400	2,7273	0,2873	1,3350	1,7100	0,6091	0,4400	0,0988	3,4499	2,0175	0,1449
Cantilever 7	-88	1,9600	2,2222	0,2622	1,2200	1,2600	0,8340	0,4400	0,0444	2,2617	1,7950	0,0882

1) Calculated from equation: $h' = \frac{A_{crossection}}{w}$

2) Calculated form equation: $CTOD = \frac{r_p(h'-a)CMOD_1}{r_p(h'-a)+a}$

Appendix F: Posters

IN-SITU FRACTURE MECHANICAL TESTING OF MICROSIZED CANTILEVERS

Master thesis spring 2014 by Kristine Greina

Supervisor: Prof. Dr. Christian Thaulow, IPM, NTNU
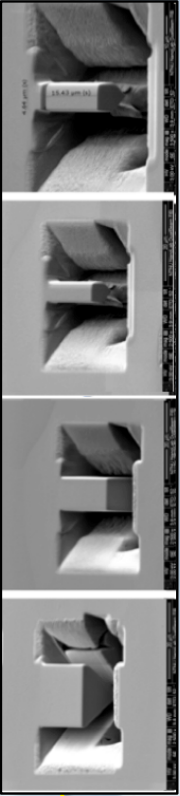
The arctic is an appealing new ventures area. However the climate is extremely demanding. An important concern in arctic environment is the ductile to brittle transition temperature (DBTT). Even tough the change of fracture properties at low temperatures has been known for more than a century; the fundamental mechanisms that control the transition have not yet been explained. By designing and constructing a cooling system, low temperature micro fracture experiments are possible. The development of innovative nanomechanical testing techniques could lead to a better understanding of fracture properties at low temperatures.

Cooling system set-up

EBSD: FIB cantilever fabrication:
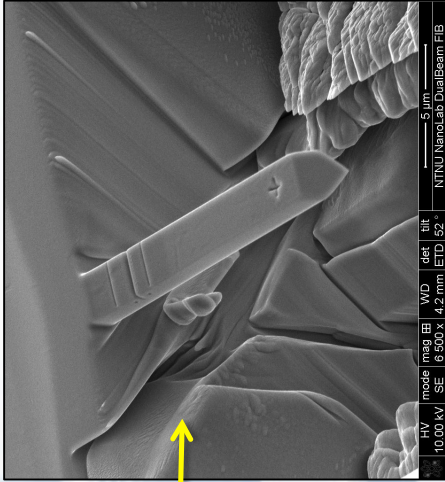
Coldfinger

In-situ loading

THE NORWEGIAN UNIVERSITY OF SCIENCE AND TECHNOLOGY DEPARTMENT OF ENGINEERING DESIGN AND MATERIALS

NTNU
Det skapende universitet

Appendix G: Posters presented at Nanobrücken

IN-SITU COMPRESSION- AND FRACTURE MECHANICAL TESTING OF NANOSTRUCTURES

The arctic is an appealing new ventures area. However the environment is extremely demanding due to harsh climate and low tempera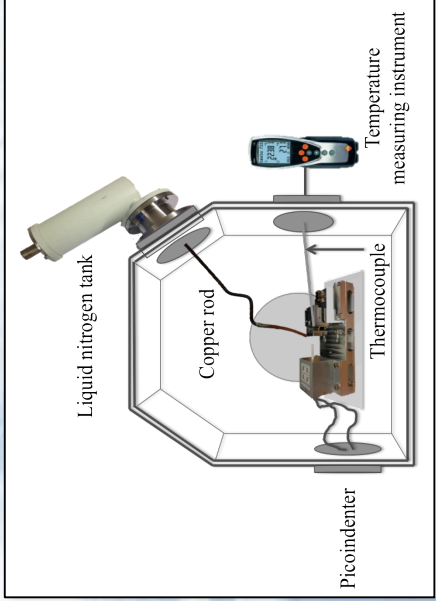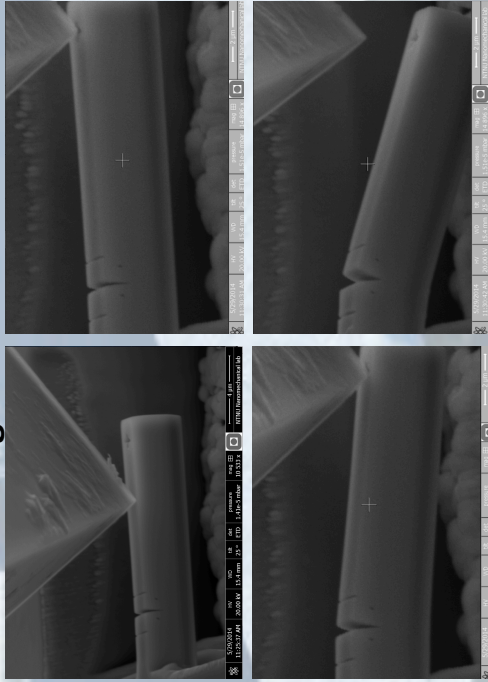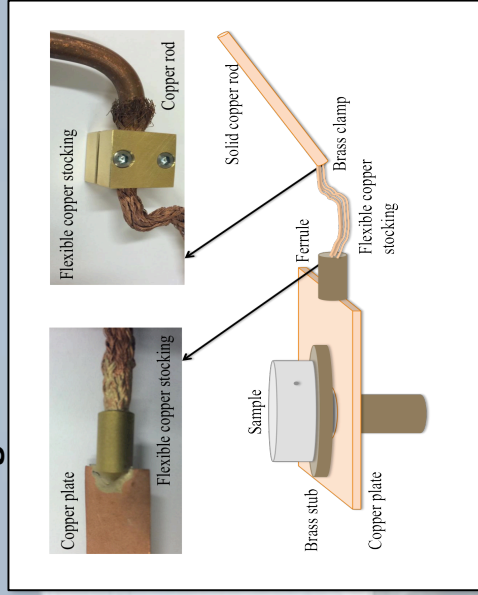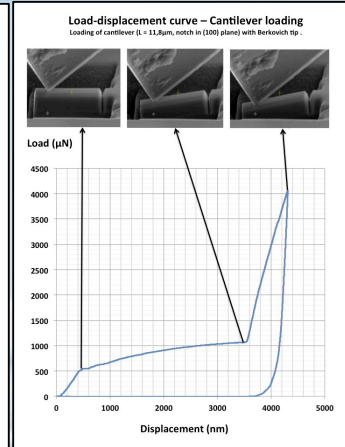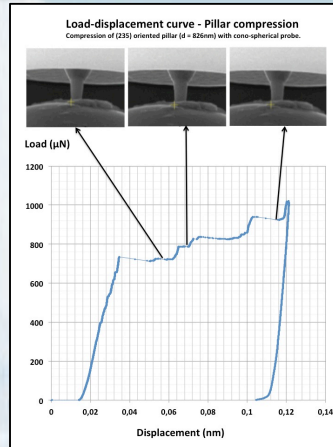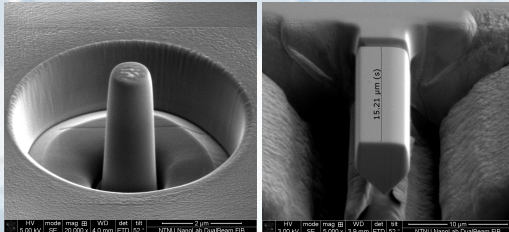tures, down to -60°C. At this temperature the brittle behavior of materials is of great concern. By cooling the samples during in-situ testing, valuable information about active slip systems, local deformation behavior, fracture toughness and CTOD at low temperatures may be obtained.

In-situ nanomechanical testing has shown to be a valuable method, suitable for analyzing local deformation behavior.
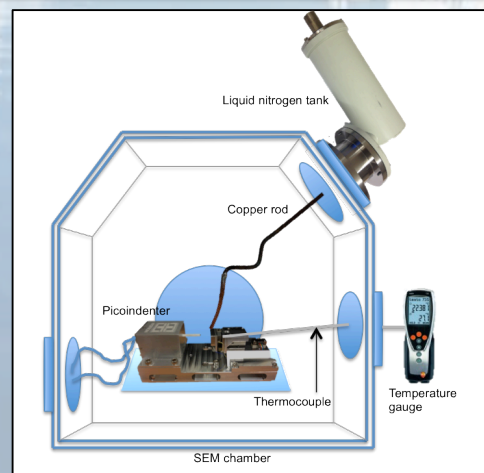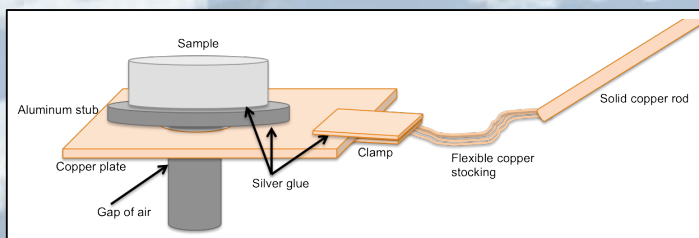
Nanomechanical testing procedure:
- Electron Backscatter Diffraction to determine crystallographic orientation
- Microsized cantilevers and nanosized pillars were fabricated using Focused Ion Beam milling
- In-situ loading and compression

Load-displacement curve - Pillar compression
Compression of (235) oriented pillar (d = 826nm) with cono-spherical probe.

Load (μN)

Load-displacement curve – Cantilever loading
Loading of cantilever (L = 11,8μm, notch in (100) plane) with Berkovich tip.

Load (μN)

Further work include cooling of the sample during in-situ nanomechanical testing, in order to obtain information about deformation behavior at low temperatures.

Cooling set-up during in-situ testing:
- The sample will be cooled down to about -60°C
- A liquid nitrogen tank will be mounted to the SEM port and connected to the sample by a thermal conductive set-up
- Silver glue will be used between the parts to ensure a stable set-up and good thermal conductivity
- The sample temperature will be measured with thermocouples

Sample

Aluminum stub

Copper plate

Gap of air

Silver glue

Clamp

Flexible copper stocking

Solid copper rod

Liquid nitrogen tank

Copper rod

Picoindenter

Thermocouple

Temperature gauge

SEM chamber

Crystallographic slip:
- CRSS produced on slip system

Applied force:
$F = \sigma A_0$

Normal to slip plane

Cross sectional area,

Slip direction

Shear stress:
$\tau_R = F_R / A^*$
$\cos\Phi\cos\lambda$

Slip plane
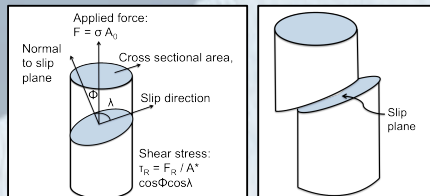
Crack tip opening displacement (CTOD):
- Direct measurement
- Hinge model
- Double gauge method/ δ_5

Crack tip

CTOA   CTOD

$CTOD_p$

$r_p(W-a)$

L_1
$CMOD_1$
L_2
$CMOD_2$
CTOD

Kristine Greina[1], Anette Brocks Hagen[1], Professor Christian Thaulow[1], Bjørn R. S. Rogne[1], Afrooz Barnoush[1], Nousha Kheradmand[1] and Odd Magne Akselsen[2]
[1]The Norwegian University of Science and Technology (NTNU), Department of Engineering Design and Materials (IPM), Trondheim, Norway.
[2]SINTEF Materials and chemistry, Trondheim, Norway.
krisgrei@stud.ntnu.no

NTNU Norwegian University of Science and Technology

SINTEF

Appendix H: Risk evaluation

NTNU — HMS

Risikovurdering

	Utarbeidet av	Nummer	Dato
	HMS-avd.	HMSRV2601	22.03.2011
	Godkjent av		Erstatter
	Rektor		01.12.2006

Dato: 20.01.2014

Enhet:

Linjeleder:

Deltakere ved kartleggingen (m/ funksjon): Kristine Gretna, Christian Thaulow, Bjørn Rune Sørås Rogne
(Ansv. Veileder, student, evt. medveiledere, evt. andre m. kompetanse)

Risikovurderingen gjelder hovedaktivitet: Masteroppgave student xx. Tittel på oppgaven. In-situ fracture mechanical testing of microsized cantilevers.

Signaturer: Ansvarlig veileder: *[signature]* Student: Kristine Gretna

ID nr	Aktivitet fra kartleggings-skjemaet	Mulig uønsket hendelse/belastning	Vurdering av sannsyn-lighet (1-5)	Vurdering av konsekvens: Menneske (A-E)	Ytre miljø (A-E)	Øk/ materiell (A-E)	Om-dømme (A-E)	Risiko-Verdi (menn-eske)	Kommentarer/status Forslag til tiltak
	FIB	Damage on equipment electrons/voltage radiation	3	A	A	C	A	3A	
		electrons/voltage radiation	1	E	D	D	A	1E	
	SEM	Damage on equipment	3	A	A	C	A	3A	
		electron/voltage radiation	1	E	D	D	A	1E	
	Picoindenter	Damage on equipment	3	A	A	C	A	3A	
	Cold finge (liquid nitrogen tank)	cold burns asphyxiation	1	E	A	A	A	1E	
	cleaning solutes (aceton/ethanol)	flamable toxic in large amounts	2	D	D	D	A	2D	

	Utarbeidet av	Nummer		Dato
	HMS-avd.	HMSRV2601		22.03.2011
HMS	Godkjent av		Erstatter	
	Rektor			01.12.2006

Kartlegging av risikofylt aktivitet

Dato: 20.01.2014

Enhet:

Linjeleder:

Deltakere ved kartleggingen (m/ funksjon): Kristine Gretna, Christian Thaulow, Bjørn Rune Serão Rogne
(Ansv. veileder, student, evt. medveiledere, evt. andre m. kompetanse)

Kort beskrivelse av hovedaktivitet/hovedprosess: Masteroppgave student xx. Tittel på oppgaven. In-situ fracture mechanical testing of microalloyed cantilevers

Er oppgaven rent teoretisk? (JA/NEI): NEI   «JA» betyr at veileder innestår for at oppgaven ikke inneholder noen aktiviteter som krever
risikovurdering. Dersom «JA»: Beskriv kort aktiviteten i kartleggingsskjemaet under. Risikovurdering trenger ikke å fylles ut.

Signaturer: Ansvarlig veileder: *[signature]*   **Student:** Kristine Gretna

ID nr.	Aktivitet/prosess	Ansvarlig	Eksisterende dokumentasjon	Eksisterende sikringstiltak	Lov, forskrift o.l.	Kommentar
	FIB (focused ion beam) milling of cantilevers	Kristine Gretna	User manual	FIB course Cleanroom course		
	SEM (scanning electron microscopy) - imaging - EBSD analysis	Kristine Gretna	User manual	Training course		
	Picoindenter: cantilever loading	Kristine Gretna	User manual	Training course		
	Coldfinger (liquid nitrogen tank) - cooling of samples in SEM chamber	Kristine Gretna	Data sheet liquid nitrogen			
	Cleaning solutes (aceton/ethanol)	Kristine Gretna	Data sheets aceton Data sheet ethanol	Ventilation	Ventilation	

98

Utarbeidet av	Nummer	Dato
HMS-avd.	HMSRV2601	22.03.2011
Godkjent av		Erstatter
Rektor		01.12.2006

Risikovurdering

Sannsynlighet vurderes etter følgende kriterier:

Svært liten 1	Liten 2	Middels 3	Stor 4	Svært stor 5
1 gang pr 50 år eller sjeldnere	1 gang pr 10 år eller sjeldnere	1 gang pr år eller sjeldnere	1 gang pr måned eller sjeldnere	Skjer ukentlig

Konsekvens vurderes etter følgende kriterier:

Gradering	Menneske	Ytre miljø Vann, jord og luft	Øk/materiell	Omdømme
E Svært Alvorlig	Død	Svært langvarig og ikke reversibel skade	Drifts- eller aktivitetsstans >1 år.	Troverdighet og respekt betydelig og varig svekket
D Alvorlig	Alvorlig personskade. Mulig uførhet.	Langvarig skade. Lang restitusjonstid	Driftsstans > ½ år Aktivitetsstans i opp til 1 år	Troverdighet og respekt betydelig svekket
C Moderat	Alvorlig personskade.	Mindre skade og lang restitusjonstid	Drifts- eller aktivitetsstans < 1 mnd	Troverdighet og respekt svekket
B Liten	Skade som krever medisinsk behandling	Mindre skade og kort restitusjonstid	Drifts- eller aktivitetsstans < 1uke	Negativ påvirkning på troverdighet og respekt
A Svært liten	Skade som krever førstehjelp	Ubetydelig skade og kort restitusjonstid	Drifts- eller aktivitetsstans < 1dag	Liten påvirkning på troverdighet og respekt

Risikoverdi = Sannsynlighet x Konsekvens
Beregn risikoverdi for Menneske. Enheten vurderer selv om de i tillegg vil beregne risikoverdi for Ytre miljø, Økonomi/materiell og Omdømme. I så fall beregnes disse hver for seg.

Til kolonnen "Kommentarer/status, forslag til forebyggende og korrigerende tiltak":
Tiltak kan påvirke både sannsynlighet og konsekvens. Prioriter tiltak som kan forhindre at hendelsen inntreffer, dvs. sannsynlighetsreduserende tiltak foran skjerpet beredskap, dvs. konsekvensreduserende tiltak.

NTNU	Risikomatrise	utarbeidet av HMS-avd.	Nummer HMSRV2604	Dato 08.03.2010
HMS/KS		godkjent av Rektor	Erstatter	09.02.2010

MATRISE FOR RISIKOVURDERINGER ved NTNU

KONSEKVENS		Svært liten	Liten	Middels	Stor	Svært stor
	Svært alvorlig	E1	E2	E3	E4	E5
	Alvorlig	D1	D2	D3	D4	D5
	Moderat	C1	C2	C3	C4	C5
	Liten	B1	B2	B3	B4	B5
	Svært liten	A1	A2	A3	A4	A5
				SANNSYNLIGHET		

Prinsipp over akseptkriterium. Forklaring av fargene som er brukt i risikomatrisen.

Farge	Beskrivelse
Rød	Uakseptabel risiko. Tiltak skal gjennomføres for å redusere risikoen.
Gul	Vurderingsområde. Tiltak skal vurderes.
Grønn	Akseptabel risiko. Tiltak kan vurderes ut fra andre hensyn.